Chair of Petroleum and Geothermal Energy Recovery

Master's Thesis

Hydrogen uptake and permeation in steels for oil and gas production and comparison with ARMCO™-Fe

Sabrina Raab, BSc

November 2022

MONTANUNIVERSITÄT LEOBEN
www.unileoben.ac.at

EIDESSTATTLICHE ERKLÄRUNG

Ich erkläre an Eides statt, dass ich diese Arbeit selbständig verfasst, andere als die angegebenen Quellen und Hilfsmittel nicht benutzt, und mich auch sonst keiner unerlaubten Hilfsmittel bedient habe.

Ich erkläre, dass ich die Richtlinien des Senats der Montanuniversität Leoben zu "Gute wissenschaftliche Praxis" gelesen, verstanden und befolgt habe.

Weiters erkläre ich, dass die elektronische und gedruckte Version der eingereichten wissenschaftlichen Abschlussarbeit formal und inhaltlich identisch sind.

Datum 27.10.2022

Unterschrift Verfasser/in
Sabrina Raab

AFFIDAVIT

I hereby declare that the content of this work is my own composition and has not been submitted previously for any higher degree. All extracts have been distinguished using quoted references and all information sources have been acknowledged.

Leoben,27.10.2022

Signature author
Sabrina Raab

Sabrina Raab, BSc

Master Thesis 2022

Petroleum Engineering / Geoenergy Engineering

Hydrogen uptake and permeation in steels for oil and gas production and comparison with ARMCO^{TM}-Fe

Supervisor:
Ao.Univ.-Prof. Dipl.-Ing. Dr.mont. Mori Gregor
Univ.-Prof. Dipl.-Ing. Dr.mont. Hofstätter Herbert

Co-supervisor/Advisor:
Dipl.-Ing. Eichinger Matthias

Chair of Petroleum and Geothermal Energy Recovery

dpe

MONTAN UNIVERSITÄT LEOBEN

Acknowledgement

The presented work was conducted at the Chair of General and Analytical Chemistry at the University of Leoben.

First, I would like to express my endless gratitude to Ao.Univ.-Prof. Dipl.-Ing. Dr.mont Gregor Mori for the unique opportunity to write this master thesis and for inspiring my interest in the field of corrosion through his passion. He supported me excellently throughout the entire progress of this master's thesis with his expertise and broadened my knowledge. I also appreciate the various life-experienced conversations as they contributed to my personal development and provided me with insights that will definitely help me in many situations in my future life path. I gladly take these experiences with me and will always remember this time.

Furthermore, I would like to sincerely thank Univ.-Prof. Dipl.-Ing. Dr.mont. Herbert Hofstätter for his support, enabling me to write this work, and his valuable contributions.

I especially want to express my appreciation to my supervisor, Dipl.-Ing. Matthias Eichinger. He continuously shared his knowledge with me, always supported me during my work in the lab, and motivated me throughout the completion of this thesis.

Furthermore, I would like to thank the corrosion working group. I greatly appreciate the warm welcome in their team and the pleasant working atmosphere. Special thanks go to Bernd Loder, Mathias Truschner, and Dino Zwittnig, without whose support I could not have completed this thesis. They always encouraged me and assisted me in all fields of my work. I will never forget our discussions and great conversations.

In particular, I am grateful to my boyfriend, Boris Jammernegg, who stood by my side in all life situations and always pushed and supported me during my studies.

Abstract

The demand for renewable energy sources like hydrogen is rising and gaining importance as the global energy market is currently facing a period of transition to combat ongoing global warming. However, even the most optimistic energy mix includes oil and gas as a key energy carrier towards the end of the century. Hydrogen is a possible future energy carrier but can be a harmful element for metals and their alloys due to its small size and the related potential to propagate within the material. To ensure the safe and smooth transport and storage of hydrogen, it is crucial to avoid hydrogen damage. Therefore, it is of utmost importance to comprehend how much hydrogen can be absorbed by the material under operating conditions and how absorbed hydrogen affects the properties of the materials used. The aim of this thesis is to study the question of how much hydrogen can be absorbed by certain steel grades used in the oil and gas industry under different conditions, which mechanisms are responsible for this, and whether the diffusion coefficient of hydrogen varies depending on the type of charging. The hydrogen uptake and permeation of three different types of carbon steels (J55, L80, P110) and ARMCO^{TM}-Fe were investigated to evaluate the diffusion coefficient. The techniques used for the permeation measurements include pressure permeation with gaseous hydrogen at 100 bar, permeation at open circuit potential (OCP), and electrochemical hydrogen permeation at a current density of 1 mA/cm^2. For the analysis of hydrogen uptake, cathodic charging and immersion tests were carried out, both at ambient temperature in NaCl solution with thiourea added. The loading time for both methods was between 1 hour and 72 hours. In addition, the hydrogen uptake was also investigated utilizing autoclave tests with gaseous hydrogen at elevated pressure for a test duration between 1 and 168 hours. Following that, the absorbed hydrogen content was analyzed, and diffusion curves were fitted for the evaluation process. To assess the hydrogen diffusivity, the diffusion coefficients of all applied techniques were calculated, and the results of J55, L80, and P110 were compared to those of ARMCO^{TM} iron. The results indicate an increased hydrogen uptake for the steel grades used in the oil and gas industry compared to ARMCO^{TM} iron. Moreover, the effective diffusion coefficient of hydrogen for oilfield steel grades is between one or two orders of magnitude lower than that of ARMCO^{TM} iron.

Zusammenfassung

Die Nachfrage nach erneuerbaren Energiequellen wie Wasserstoff steigt und gewinnt immer mehr an Bedeutung, da sich der globale Energiemarkt aktuell im Wandel befindet, um die fortschreitende Erderwärmung zu bekämpfen. Jedoch sieht selbst der optimistischste Energiemix Öl und Gas als Hauptenergieträger bis zum Ende des Jahrhunderts vor. Wasserstoff ist ein möglicher zukünftiger Energieträger aber kann aufgrund seiner geringen Größe und des damit verbundenen Potenzials, sich im Material auszubreiten, ein schädliches Element für Metalle und ihre Legierungen sein. Um einen sicheren und reibungslosen Transport und die Speicherung von Wasserstoff zu schaffen, ist die Vermeidung von Wasserstoffschäden essentiell. Dabei ist es von entscheidender Bedeutung zu verstehen, wieviel Wasserstoff unter Betriebsbedingungen vom Werkstoff absorbiert werden kann und wie der absorbierte Wasserstoff die Eigenschaften der verwendeten Materialien beeinflusst. Ziel dieser Arbeit ist es, den Fragen nachzugehen, wie viel Wasserstoff von bestimmten Stählen in der Öl- und Gasindustrie unter verschiedenen Bedingungen aufgenommen werden kann, welche Mechanismen dafür verantwortlich sind und ob der Diffusionskoeffizient von Wasserstoff je nach Art der Beladung variiert. Zur Ermittlung des Diffusionskoeffizienten wurden die Wasserstoffaufnahme und -Permeation von drei verschiedenen Kohlenstoffstählen (J55, L80, P110) und ARMCO^{TM}-Fe untersucht. Die Permeationsmessungen beinhalten dabei die Verfahren der Wasserstoff-Druckpermeation, der Permeation bei Ruhepotential und der elektrochemischen Wasserstoffpermeation bei einer Stromdichte von 1 mA/cm^2. Für die Evaluierung der aufgenommenen Wasserstoffmenge wurden kathodische Beladungsversuche und Auslagerungstests in einer NaCl Lösung mit Zugabe von Thioharnstoff bei Raumtemperatur durchgeführt. Die Beladungszeit lag dabei zwischen einer Stunde und 72 Stunden. Zusätzlich sollte auch die Wasserstoffaufnahme mittels Autoklaventests mit gasförmigem Wasserstoff bei erhöhtem Druck untersucht werden für eine Testdauer zwischen einer Stunde und 168 Stunden. Nach der Wasserstoffbeladung wurde der Wasserstoffgehalt im Metall analysiert und Diffusionskurven für die Auswertung erstellt. Zur Bewertung des Diffusionsverhaltens wurden die Wasserstoff-Diffusionskoeffizienten aller durchgeführten Methoden bestimmt, und die Ergebnisse von J55, L80 und P110 mit denen von ARMCO^{TM}-Eisen verglichen. Die Resultate zeigen für die in der Öl- und Gasindustrie verwendeten Stahlsorten eine erhöhte Wasserstoffaufnahme im Vergleich zu ARMCO^{TM}-Eisen. Des Weiteren ist der effektive Diffusionskoeffizient von Wasserstoff für Ölfeldstahlsorten um eine oder zwei Größenordnungen niedriger als der von ARMCO^{TM}-Eisen.

Table of Contents

Acknowledgement vi

Abstract vii

Zusammenfassung viii

Chapter 1 1

Introduction 1

Chapter 2 3

Hydrogen uptake of steels in oil and gas production 3

2.1 Corrosion 4

2.1.1 Hydrogen evolution reaction 6

2.1.2 Recombination inhibitors 8

2.2 Cathodic charging 9

2.2.1 Charging parameters 9

2.3 Pressure hydrogen 12

2.3.1 Pressurized hydrogen charging 14

Chapter 3 16

Diffusion and permeation of hydrogen in steels 16

3.1 Trapping of hydrogen 16

3.2 Hydrogen diffusion 17

3.2.1 Numerical analysis of the diffusion coefficient 19

3.2.2 Temperature dependence of hydrogen diffusion 21

3.3 Permeation measurements and diffusion coefficient 24

3.3.1 Principle of electrochemical permeation 24

3.3.2 Diffusion coefficient 26

3.3.3 Diffusion coefficients from literature 28

3.3.4 Pressure permeation 29

Chapter 4 32

HSE aspects related to hydrogen gas storage and transport 32

4.1 Hydrogen properties 32

4.1.1 Gaseous hydrogen properties 32

4.2 Gaseous hydrogen hazards 33

4.3 Utilization of existing natural gas infrastructure for hydrogen storage and transport 34

4.4 Integrity and reliability of material 34

4.5 Further risks 35

Chapter 5 ..... **36**
Experimental section 36
5.1 Materials 36
5.1.1 Chemical analysis 36
5.1.2 Mechanical properties 38
5.1.3 Microstructure 38
5.2 Hydrogen charging 43
5.2.1 Immersion testing 43
5.2.2 Cathodic charging 44
5.2.3 Autoclave tests 45
5.2.4 Hydrogen analysis 46
5.3 Hydrogen permeation 47
5.3.1 Electrochemical permeation 48
5.3.2 Permeation at open circuit potential 49
5.3.3 High pressure permeation 50
Chapter 6 ..... **52**
Results 52
6.1 Hydrogen uptake 52
6.1.1 Immersion testing 53
6.1.2 Cathodic charging 57
6.1.3 Autoclave tests 61
6.2 Hydrogen permeation 62
6.2.1 Electrochemical permeation 62
6.2.2 Permeation at open circuit potential 71
6.2.3 Pressure permeation 72
Chapter 7 ..... **73**
Discussion 73
Chapter 8 ..... **78**
Conclusion 78
References **80**

Chapter 1

Introduction

The oil and gas industry is facing ongoing problems of corrosion and material damage caused by hydrogen absorbed in the metal from various sources. This leads to a deterioration of the material properties and consequently to significant functional degradation and destruction of the metal up to the ultimate failure of the equipment. The material deterioration associated with corrosion might also cause economic damage and even pose a potential hazard to humans.

In order to meet international climate protection agreements and drive forward decarbonization by the end of the century, hydrogen will also serve an essential role in the upcoming years with regard to the energy transition, as energy production from renewable sources instead of fossil fuels becomes increasingly attractive worldwide.

A recent new alternative adopted for hydrogen transportation as a mixture of natural gas is blending hydrogen into natural gas pipelines. Besides that, hydrogen as an energy carrier has many similarities to the current petroleum business in terms of storage, generation, processing, and transportation. Therefore, existing transport pipeline networks and underground gas storage facilities offer the possibility for the future use of hydrogen due to their vast capacities, and implementation of infrastructures and business plans becomes easier and more desirable.

However, the use of hydrogen may lead to material damage. Therefore, to ensure safe operations in both, petroleum production and hydrogen storage and transport, it is essential to develop an understanding of the hydrogen content a material can absorb and the mechanism responsible for it.

The most widely used material for the pipeline transport and production of oil and gas is carbon steel and its alloys with elements such as Cu, Ni, Mo, V, Nb, or Cr that can greatly reduce the absorption and diffusion of hydrogen in steel. Carbon steel is chosen for its ease of availability and relative cost-effectiveness, in addition to the amount of information and experience available on its use. Furthermore, carbon steel has good mechanical properties, is excellent for welding, and its corrosion resistance can be improved in various ways.

In this work, electrolytic hydrogen uptake in steels during corrosion and cathodic charging are first discussed, as well as hydrogen uptake under the influence of pressure and hydrogen diffusion by permeation experiments. Moreover, various factors influencing hydrogen uptake are explained, but especially the impact on the diffusion coefficient is described in more detail.

The practical part of this thesis deals with experimental procedures and the comparison of obtained results regarding absorbed hydrogen in the metal by different charging methods. J55, L80, and P110 carbon steels were investigated throughout the experiments and compared with ARMCO^{TM} pure iron to establish a possible relationship between the microstructure and the amount of absorbed hydrogen and further the diffusion coefficients. One of the main objectives of this work is to determine the diffusion coefficients for all materials based on the data measured during the conducted experiments and to compare them in order to evaluate whether the diffusivity varies depending on the type of hydrogen charging. The experimental results obtained in this work make it possible to evaluate the behavior of diffusible hydrogen for common steel grades used in the oil and gas industry and provide information on the absorbed hydrogen content in the steels to gain a deeper understanding of future operations in the field.

Chapter 2

Hydrogen uptake of steels in oil and gas production

There are several pathways for hydrogen uptake in metals. The metal can absorb hydrogen due to interactions with a gaseous environment as well as through interactions with an aqueous electrolyte. However, the fundamental mechanism of hydrogen uptake is related to the absorption of adsorbed hydrogen atoms at the solution-metal interface [1]. The challenges of hydrogen presence in the petroleum industry arise from the natural hydrogen evolution as a by-product of electrochemical corrosion reactions of produced and processed fluids, the surrounding environment, or hydrogen already trapped in the metal due to the manufacturing process. Corrosion is usually associated with the presence of water, gaseous pollutants (H_2S and CO_2), and oxygen intrusion. Furthermore, higher conductivity caused by the presence of ionic species from the surrounding may accelerate the corrosion process. During the depletion of oil and gas fields, the severity of corrosion increases as a result of a higher water production rate, the content of harmful gases, and the contamination of fluids by the introduction of steam or CO_2 used for enhanced oil production [2]. Moreover, it is also common in practice to reinject the produced water in the wellbore to maintain the reservoir pressure, thus stabilizing the reservoir, as well as to perform water flooding with seawater or freshwater to achieve enhanced oil recovery. Additionally, rising operating temperature and pressure conditions also induce increased corrosion severity [3]. Regardless of the source of hydrogen uptake, its presence can cause severe degradation of the mechanical characteristics of steel in the form of hydrogen-induced damage, leading to premature failure of the material.

2.1 Corrosion

In general, it is well known that in the oil and gas industry exists a high risk of corrosion of downhole facilities when they are in contact with an electrolyte such as water, carbon dioxide (CO_2), or hydrogen sulfide (H_2S). The reaction can also be aggravated by microbiological activities, and the susceptibility depends on the type of material used [4]. However, the most harmful gases in the petroleum industry involve CO_2 and H_2S, for which the undergoing corrosion processes are also known as sweet corrosion (CO_2) and sour corrosion (H_2S) [5].

In principle, the electrochemical corrosion process is divided into two sub-processes at the interface between the metal and solution that co-occur in the anodic and cathodic regions of the metal. On the one hand, a cathodic reaction takes place, whereby an oxidant changes into a reduced form by absorbing electrons. In the case of acidic corrosion, the cathodic reduction of electrons results in the formation of atomic hydrogen, followed by the adsorption of the atoms on the metal surface. On the other hand, the anodic reaction leads to metal dissolution due to the release of electrons, resulting in the transformation from metal to metal ions. [6]. These reactions can be explained by the fact that electrons released from the metal exposed to the solution at the anodic site move through to the cathodic site, where they are picked up by species in the electrolyte that will be reduced [7].

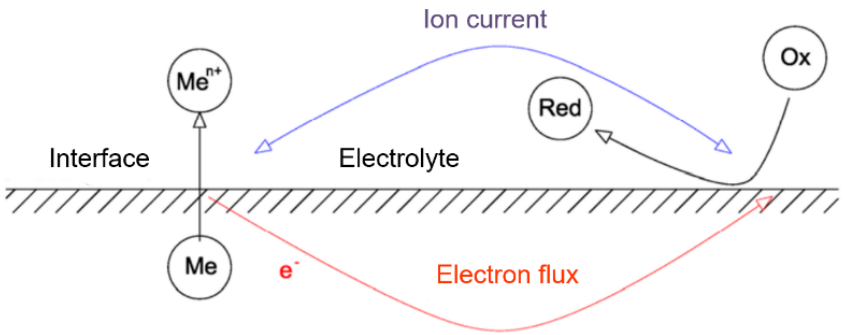

Figure 1. The electrochemical corrosion mechanism [6]

Common oxidation/ reduction reactions in the oilfield [8]:

Anode reaction (Oxidation): $Fe \rightarrow Fe^{2+} + 2e^-$ and $Fe \rightarrow Fe^{3+} + 3e^-$ (1)

Cathodic reaction (Reduction):

$2H^+ \rightarrow H_2 + 2e^-$ (acidic solutions) (2)

$O_2 + 4H^+ + 4e^- \rightarrow 2H_2O$ (acidic solution) (3)

$O_2 + 2H_2O + 4e^- \rightarrow 4OH^-$ (neutral or basic solutions) (4)

Both, H_2S and CO_2 can dissolve in an aqueous environment and form corrosive solutions with water, acting as a reaction catalyst. When CO_2 dissolves in water, carbonic acid is generated, which lowers the pH of the solution, making it acidic. The reaction proceeds as follows [9,10]:

$H_2O + CO_2 \rightarrow H_2CO_3$ (5)

$H_2CO_3 \rightarrow HCO_3^- + H^+$ (6)

$HCO_3^- \rightarrow CO_3^- + H^+$ (7)

$Fe + 2H^+ \rightarrow H_2 + Fe^{2+}$ (8)

Water dissociates during the process to form H^+ protons, while the two carbonic acid dissociation steps promote the process of hydrogen generation.

Formation of corrosion products:

$CO_3^{2-} + Fe^{2+} \rightarrow FeCO_3$ (iron carbonate film) (9)

The dissolution of iron characterizes the anodic reaction, and the overall reaction can be described as follows:

$H_2O + CO_2 + Fe \rightarrow FeCO_3 + H_2$ (10)

In the sour corrosion process, H_2S partially dissociates in aqueous solutions and forms hydronium ions (H^+) and bisulphide ions (HS^-) depending on the pH value and other factors [11]:

H_2S dissociation: $H_2S\ (aq) \rightarrow HS^-\ (aq) + H^+\ (aq)$ (11)

HS^- dissociation: $HS^-\ (aq) \rightarrow S^{2-}\ (aq) + H^+\ (aq)$ (12)

H_2S reduction: $2H_2S\ (aq) + 2e^- \rightarrow H_2\ (aq) + 2HS^-\ (aq)$ (13)

Anodic reaction: $Fe \rightarrow Fe^{2+} + 2e^-$ (14)

Overall reaction: $Fe + H_2S + H_2O \rightarrow FeS + H_2$ (15)

The predominant net reaction is the oxidation of iron and the reduction of protons to elemental hydrogen. Iron releases electrons in the anodic reaction and forms with the dissolved sulfide ions solid porous films of iron sulfides (such as FeS) as corrosion by-products on the steel surface [2].

2.1.1 Hydrogen evolution reaction

The generated H^+ ions in the solution migrate close to the metal surface, where the atomic particles are discharged and adsorbed at the metal/solution interface. This is the first step of the hydrogen evolution process, and it is also known as the Volmer reaction [7,12]:

Acidic solution: $H^+ + e^- \rightarrow H_{ad}$ (16)

Neutral or basic solution: $H_2O + e^- \rightarrow H_{ad} + OH^-$ (17)

The adsorbed hydrogen atoms (H_{ad}) on the cathodic surface can get absorbed by the metal and diffuse into the material, or the reaction proceeds to form molecular hydrogen. There are two possible pathways for the recombination: the Tafel reaction and the recombination according to Herovsky.

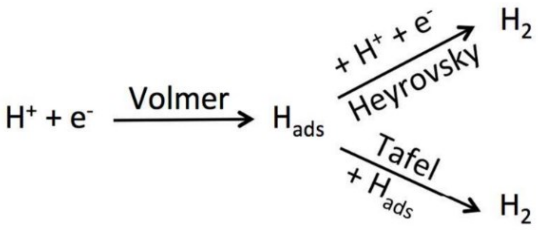

Figure 2. Mechanisms of hydrogen evolution [13]

The Tafel mechanism is based on chemical desorption and refers to the reaction of two adsorbed hydrogen atoms forming an adsorbed hydrogen molecule [12]:

$$H_{ad} + H_{ad} \rightarrow H_{2ad} \quad (18)$$

Moreover, the hydrogen recombination may also be subjected to an electrochemical reaction, according to Herovsky, involving an adsorbed hydrogen atom, a hydrogen proton, and an electron from the material [12]:

$$H_{ad} + H^+ + e^- \rightarrow (H_2)_{ad} \quad (19)$$

However, in both reactions, the hydrogen molecules escape harmlessly as gas from the metal surface after desorption. The overall procedure can therefore be described according to the combined reactions of Volmer ─ Tafel, or according to Volmer ─ Herovsky (Fig. 3) [12].

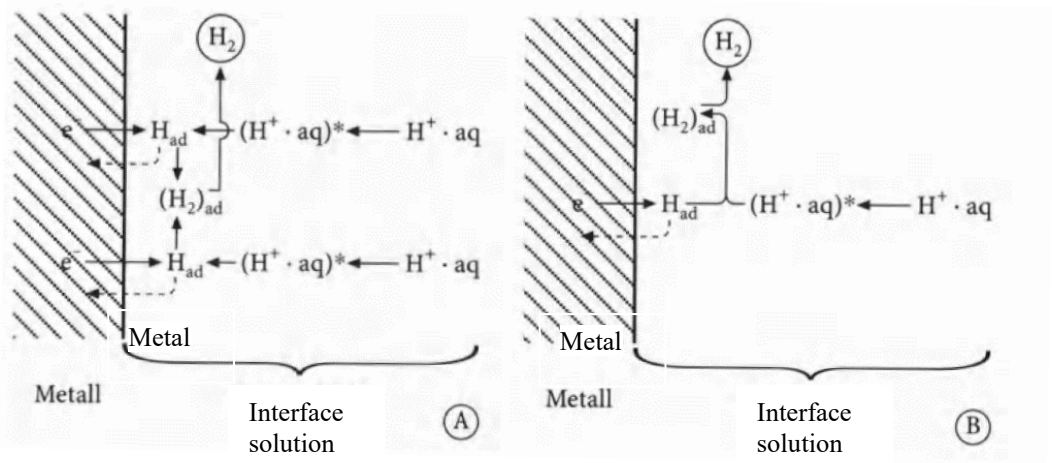

Figure 3. Illustration of cathodic hydrogen evolution: A) According to the Volmer-Tafel mechanism, B) according to the Volmer-Heyrovsky mechanism [12]

If recombination proceeds unimpeded, hydrogen evolution occurs faster than the absorption of hydrogen atoms.

However, inhibition of recombination leads to increased adsorption of hydrogen atoms on the metal surface, hence an increased absorption in the material, which can cause hydrogen-induced damage and can lead to unpredictable failures of the equipment [6].

2.1.2 Recombination inhibitors

The term refers to so-called poisons in the electrolyte solution that promote hydrogen uptake in the steel and inhibit the recombination to molecular hydrogen [14]. Consequently, atomic hydrogen may diffuse interstitially into the steel and distribute within the material according to Fick's law. The hydrogen preferentially accumulates in the mixed crystal at the interstitial sites of foreign atoms with corresponding energy. Among the known inhibitors such as hydrocyanic acid (HCN) and arsenic oxide (As_2O_3), the oil industry is particularly confronted with the presence of poisons like H_2S as well as CO and CO_2 [3,15]. The corrosion rates of carbon steels and low alloy steels in H_2S-containing environments tend to rise with decreasing pH values of the aqueous solution. In general, as the reservoir pressure drops during the production period, the volumetric percentage concentration of hydrogen sulfide increases [11].

The most common theories for the mechanism of enhanced hydrogen absorption by recombination poisons propose that the Tafel equation and/or the Herovsky equation are impeded, and the promoters catalyze the Volmer reaction. Furthermore, Bockris reported that hydrogen promoters weaken the bonding energy of metal and hydrogen atoms ($M\text{-}H_{ad}$), thus facilitating hydrogen entering into steel [16].

For electrochemical hydrogenation in the laboratory, the electrolytes can be diluted by adding various concentrations of poisons, such as sulfur, arsenic, and thiourea, as well as ammonium thiocyanate [17,18]. Thiourea (CH_4N_2S) and its derivatives are frequently used and are suitable inhibitors. The molecule of thiourea possesses a single electron pair, which promotes the electron transfer to the metal and the formation of a covalent bond. The corrosion inhibitor serves as a protective film whereby its adsorption bond strength is controlled by the electron density, the donor atom of the functional group, and the polarizability of the group. The organic substances assigned to this group include mainly oxygen, sulfur, and nitrogen atoms, as well as multiple bonds in the molecules that enable adsorption on the metal surface [19].

Han et al. investigated the effect of thiourea on hydrogen uptake in alkaline and acidic solutions. They noted a significantly lower hydrogen uptake in the alkaline medium than in the acidic solution. In addition, they confirmed the inhibiting effect of thiourea, resulting in increased hydrogen uptake [14].

2.2 Cathodic charging

Various techniques have been developed for the hydrogenation of materials in the lab up to now. Cathodic hydrogen charging is one of these methods, which involves an electrochemical cell filled with an electrolyte. The immersed specimen serves as the cathode in the cell, while a platinum electrode acts as the anode [17]. The schematic setup is shown in Fig. 4.

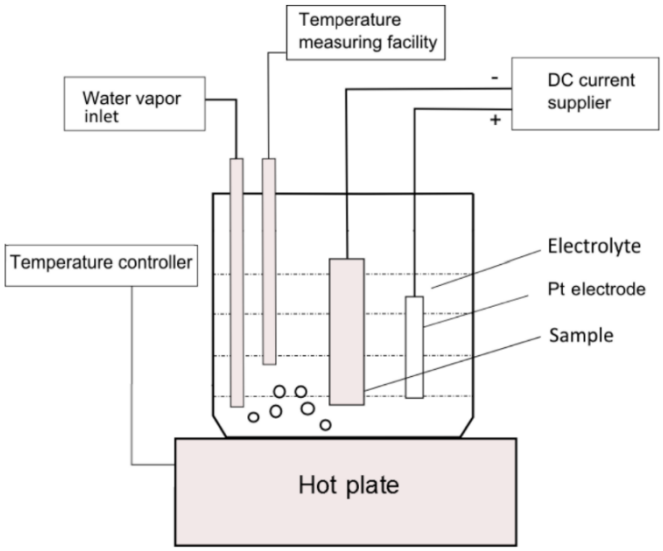

Figure 4. Illustration of a cathodic hydrogen charging setup [17]

When the electrodes are subjected to an applied potential, the electrolyte solution decomposes, and adsorbed hydrogen atoms are generated on the metal surface as described in equations (16) and (17) by the reduction of protons (H^+) in acidic solutions and the dissociation of water in neutral or basic solutions, respectively. The applied potential enhances the production of adsorbed hydrogen atoms on the metal surface while simultaneously acting as a driving force for their diffusion into the material [17].

2.2.1 Charging parameters

The main parameters influencing cathodic charging found in the literature are temperature, applied current density, charging time, and the electrolytic medium [17]. The effects of them on hydrogen charging are described in more detail in the following section.

2.2.1.1 Effect of charging time

In both, the corrosion process by immersion tests and the cathodic charging process, a saturation state of the hydrogen concentration can be noticed after sufficient charging time. Fig. 5 illustrates the hydrogen content as a function of the charging time and also shows a comparison of the experimental data with the theoretical diffusion model. At charging times of less than 12 hours, the absorption rate is higher, implying a more rapid diffusion of hydrogen in the specimen. The saturation state is mainly observable in this case between 24 and 48 hours, and the hydrogen content remains constant even after 72 hours. Moreover, the saturated hydrogen content value also represents the hydrogen concentration on the charging surface [20].

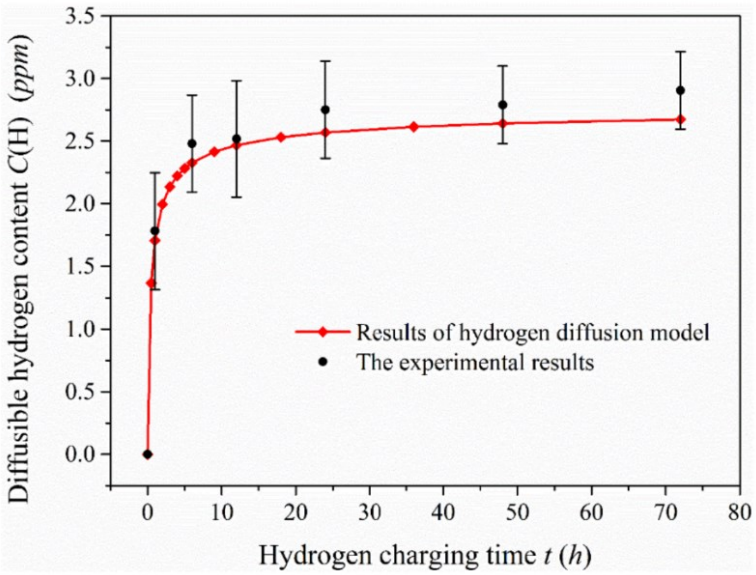

Figure 5. Comparison of diffusible hydrogen content measured in the 1-mm-thick specimen after charging and analytical results using a hydrogen diffusion model [20]

2.2.1.2 Effect of the current density

Previous research showed that the absorbed hydrogen concentration rises as the charging time and current density increase. This effect can be explained by an increase in current density that leads to initially better absorption kinetics and consequently results in a higher absorbed hydrogen content [21,22]. If the hydrogen progressively reaches the saturation state in the near-surface region, further diffusion into the material becomes slower and takes more time, as demonstrated in the diagram in Fig. 6 [22].

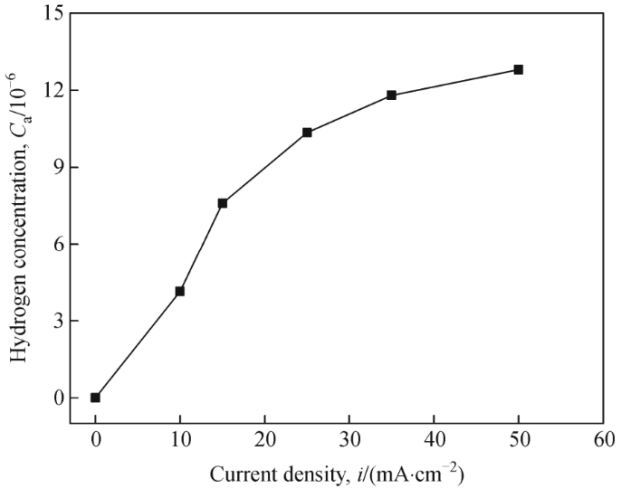

Figure 6. Hydrogen concentration vs. different charging densities [22]

Moreover, the effect of varying current densities of cathodic charging is also illustrated in the diagram for ultra-low carbon steel (ULC) in Fig. 7 [21].

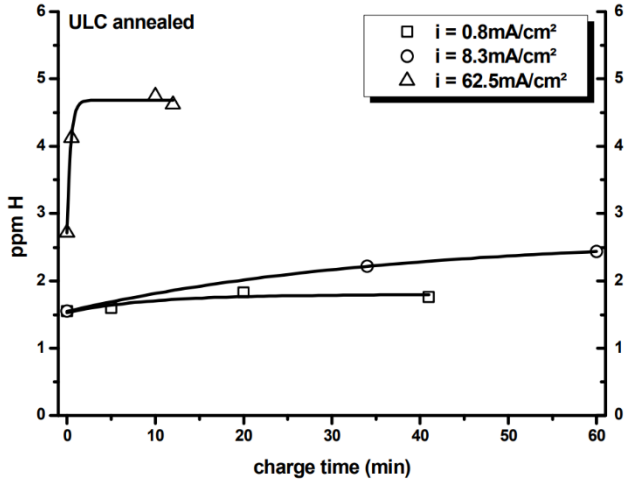

Figure 7. Hydrogen content as a function of different charging current densities [21]

Fig. 7 shows a higher achieved hydrogen content at increased current density after a shorter test duration. Hydrogen promotes metal dissolving and the formation of corrosion cover layers of varying thicknesses on the metal surface. However, Qiao, Y. et al. studied the behavior of hydrogen uptake at different current densities and discovered that once the current density exceeds a particular value, cracks are formed in the layer, allowing the electrolyte to penetrate the film and interact with the steel matrix again, thus accelerating steel corrosion [23].

2.2.1.3 Effect of the medium

Cathodic charging is feasible with acidic as well as neutral and basic electrolytes, whereby the amount of absorbed hydrogen is strongly influenced by the prevailing pH value of the surrounding solution. The previously discussed promoters, such as thiourea (CH_4N_2S), ammonium thiocyanate (NH_4SCN), or arsenic species, are frequently added to the electrolyte to hinder the recombination process and improve hydrogen uptake [14,18]. Besides that, an enhanced cathodic reduction is generally associated with lower pH values. D.Pérez Escobar et al. revealed that effect by investigating the absorbed hydrogen content of FB450 steel in various electrolytes. They examined the samples in an alkaline NaOH solution and an acidic H_2SO_4 environment with the addition of recombination inhibitors and observed a significantly higher hydrogen concentration for the acidic conditions than for the alkaline ones (Fig. 8) [14].

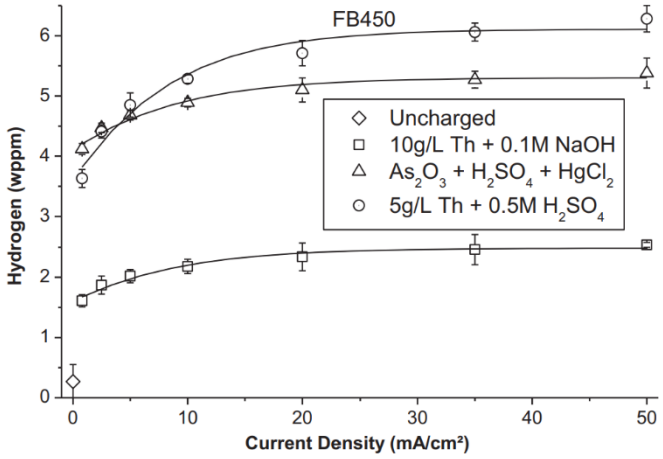

Figure 8. Hydrogen concentration for various electrolytes and different current densities of FB450 steel [14]

2.3 Pressure hydrogen

Besides potential hydrogen uptake due to corrosion in an aqueous electrolyte, there is also the possibility of hydrogen absorption in the gaseous environment. This is particularly relevant during the transport of natural gas in pipelines, as well as for further processing in high-pressure boilers in the petrochemical industry. Since hydrogen damage can be induced by the hydrogen contained in natural gas, the equipment may be subject to deterioration and premature failure [24]. At standard temperature and pressure conditions, hydrogen gas consists solely of H_2 molecules and dissociates to form hydrogen atoms as the temperature rises [12].

When metal gets in contact with hydrogen molecules from the gas atmosphere, these molecules undergo physisorption at the surface due to Van der Waals interactions. Depending on active sites at the surface, the hydrogen molecules may be subjected directly to dissociation to form hydrogen atoms on the surface and subsequently get absorbed [25]. Subsequently, the diffusion of hydrogen within the steel is enabled by establishing an equilibrium concentration between the partial pressure of gaseous hydrogen in the environment and the hydrogen concentration in the subsurface layers of the steel [26].

The reaction mechanism is depicted below and can be described as [25]:

$$H_2(g) \rightarrow H_{ad} + H_{ad} \rightarrow 2H_{ab} \quad (20)$$

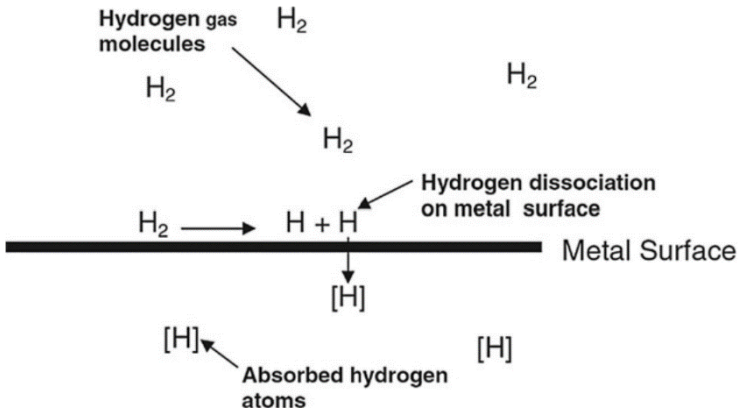

Figure 9. Hydrogen absorption in gaseous environment [25]

Since the partial pressure of hydrogen highly impacts the reaction, the hydrogen activity at low temperatures ($T \leq 200$ °C) and low partial pressures ($p_{H2} \leq 100$ bar) is usually insufficient to adsorb hydrogen atoms on the surface and further absorb them. As a result, an increase in pressure also accompanies an increase in hydrogen absorption. However, if the material is mechanically loaded, low pressures are often enough to cause hydrogen adsorption at the interface [12,27].

Sieverts and Krumbhaar first introduced hydrogen solubility in metal as a function of the hydrogen partial pressure and the temperature. The relationship is characterized by Sievert's law [28]:

$$S = S_0 * \sqrt{p} * e^{\frac{-\Delta H}{R*T}} \quad (Eq.1)$$

Whereby S_0 expresses the solubility constant, p defines the partial pressure of the H_2 gas, R is the universal gas constant, ΔH corresponds to the heat of dissolution, and T is the absolute temperature [28].

2.3.1 Pressurized hydrogen charging

The methods used for experimental tests of hydrogen uptake of gaseous hydrogen typically involve in-situ setups of pressurized vessels or autoclaves. In principle, an autoclave is a test cell that offers the possibility to investigate the amount of absorbed hydrogen in different materials for high pressure and often high-temperature conditions. They are typically made of stainless steel and can be applied statically or dynamically during the experiment [24].

In order to eliminate the impact of oxygen and other ambient gases, the vessels must be evacuated and flushed multiple times with argon before the experiments can be conducted. The autoclaves are then filled with the specified test solutions or dry hydrogen (or other test gases of interest) at specific pressure and temperature conditions for a particular period of charging [29].

However, as previously mentioned, elevated pressure exceeding 100 bar is necessary to detect significant hydrogen uptake without mechanical stress. This phenomenon was also confirmed in autoclave tests with dry hydrogen at pressure conditions of up to 100 bar and ambient temperature. The materials examined were ARMCO-iron and a carbon steel L80 frequently used in the oilfield industry. The results are shown in Fig. 10 and indicate just a slight hydrogen uptake by the specimens [30].

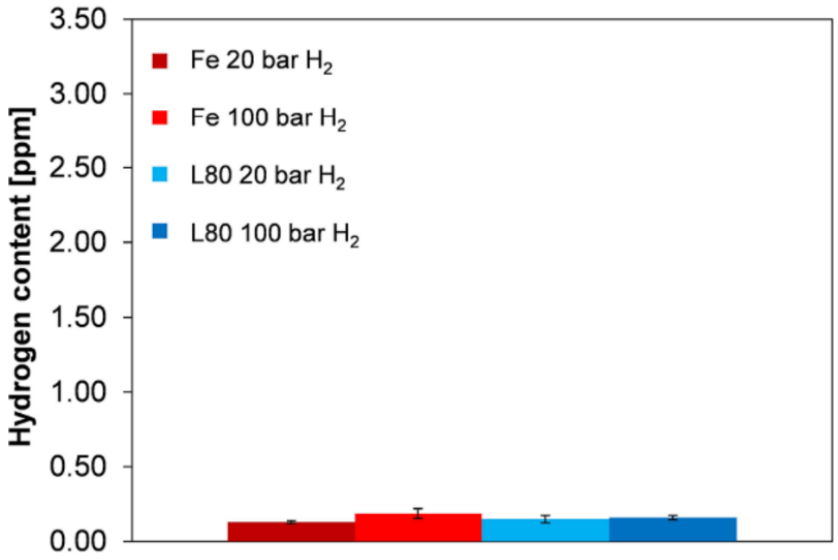

Figure 10. Hydrogen content after charging at different pressures [30]

Another analysis using autoclave tests was conducted by Trautmann et al.. The examined materials were L80 carbon steel and furthermore P110 carbon steel, which is also commonly used in the petroleum industry [28]. The specimens were tested under conditions with dry H_2 gas at pressures of 20 bar and 100 bar as well as with wet CO_2 at 5 bar. Additionally, an aqueous NaCl electrolyte was added to some autoclaves to create wet conditions with H_2. All experiments were performed for 30 days at both ambient and elevated temperature of 80 °C. The results in Fig. 11 and Fig. 12 revealed a low hydrogen uptake in all experimental setups for both materials. Nevertheless, the hydrogen content increases with increasing partial pressure. However, in tests conducted by adding an electrolyte, hydrogen uptake was observed to be enhanced at 20 bar and 100 bar, as well as at room temperature and elevated temperature. Furthermore, the presence of CO_2 provides an increased hydrogen uptake for all conditions, which is further enhanced by the mixture of the gases H_2 and CO_2 [28].

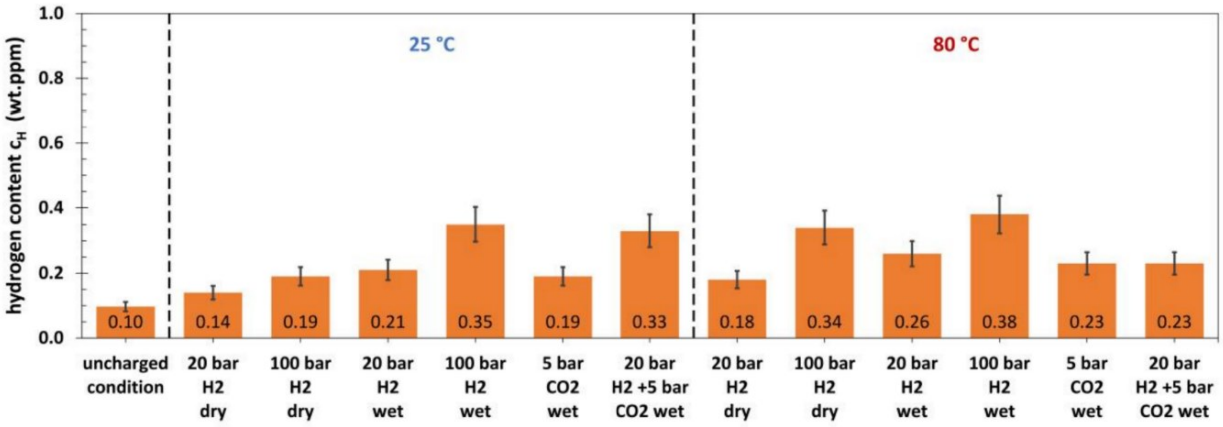

Figure 11. Hydrogen concentration of P110 after pressurized charging under various conditions [28]

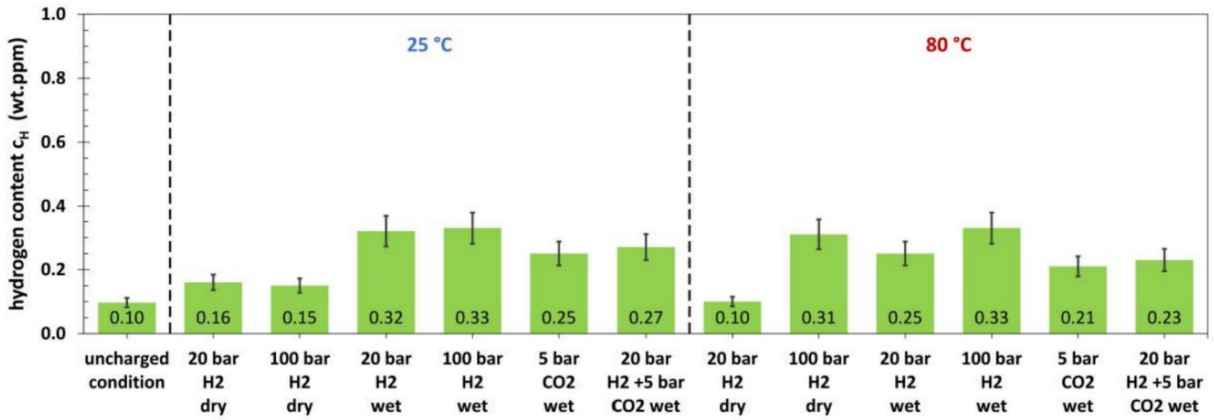

Figure 12. Hydrogen concentration of L80 after pressurized charging under various conditions [28]

Chapter 3

Diffusion and permeation of hydrogen in steels

3.1 Trapping of hydrogen

Once absorbed by steel, hydrogen may dissolve at interstitial sites or occupy lattice imperfections. Following Sievert's law described in the previous chapter, hydrogen achieves low solubility in iron. However, experimental results revealed a higher hydrogen content than predicted by theory [24]. This effect was also studied by Darken and Smith, who concluded that the increased hydrogen content must be induced by the trapping of hydrogen in lattice defects in addition to interstitial accumulation [31,32]. The term lattice defects refers to microstructural imperfections, including internal phase boundaries, precipitations, voids, dislocations, interstitial atoms, and vacancies (Fig. 13) [33].

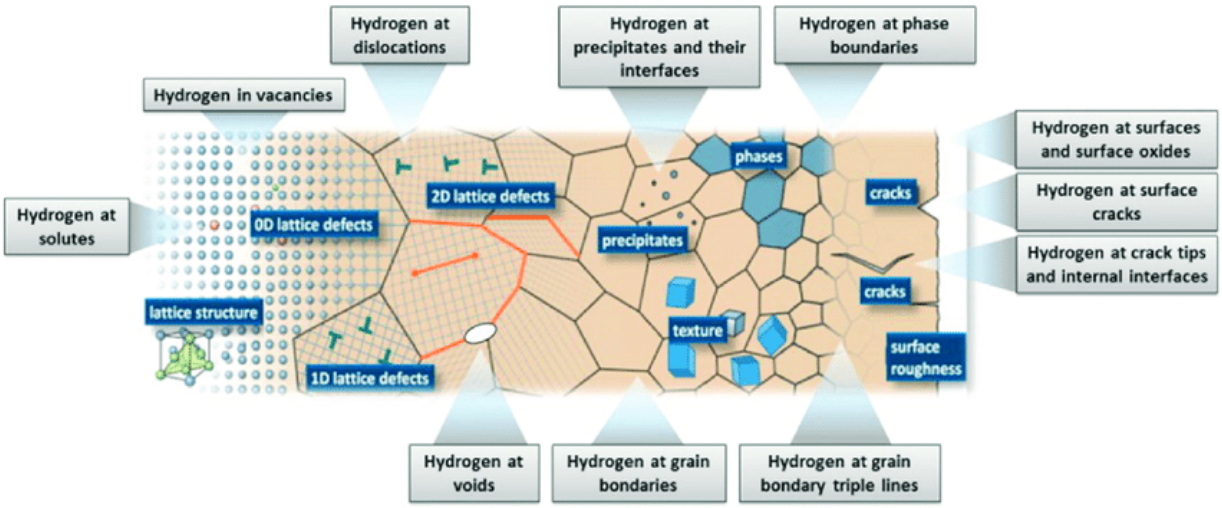

Figure 13. Various sites for hydrogen trapping in steels [33]

These features in the material exhibit higher binding energies than the lattice and are potential accumulation spots for hydrogen defined as so-called traps [12]. Moreover, such traps enable hydrogen atoms to recombine, forming molecular hydrogen. In regard to different binding energies proportional to the trapping depth, they are characterized as deep irreversible traps and flat reversible traps [3]. According to this classification, hydrogen in reversible traps may overcome the activation energy (≤60 kJ/mol) and migrate through the lattice as diffusible hydrogen after desorption. Reversible traps often include dislocations, coherent precipitates, and small-angle grain boundaries.

In contrast, the hydrogen in irreversible traps (such as incoherent precipitates and grain boundaries) remains inactive and is not able to escape at moderate temperatures due to the high activation energy (≥ 60 kJ/mol) [34]. Since energy must be applied from the trapped hydrogen greater than the migration energy, diffusing hydrogen atoms remain within a trap much longer than in a lattice site. The presence of traps thus explains the apparent lower diffusivity than the lattice diffusivity [31]. Furthermore, the total quantifiable hydrogen content is composed of diffusible hydrogen dissolved at interstitial lattice sites and hydrogen atoms bound in traps.

The effects of traps on diffusion depend on the density and distribution of trapping sites and the depth of the associated potential. In practice, there may be a spectrum of trapping sites in a metal, each with a characteristic binding energy. However, often one or two types of traps will dominate and determine the effective diffusivity at a given temperature [35].

3.2 Hydrogen diffusion

Diffusion in metals proceeds by hydrogen atoms hopping between interstitial sites and is mainly driven by the hydrogen concentration as well as the velocity of the hopping atoms [25]. The interstitial sites occupied during diffusion in body-centered cubic (bcc) metals are preferentially tetrahedral at low temperatures (room temperature) and octahedral at higher temperatures (above 100 °C). Compared to this, the sites tend to be octahedral in face-centered cubic (fcc) metals or austenitic stainless steels, while in hexagonal close-packed (hcp) metals and alloys, the sites are favorably tetrahedral at ambient temperatures [25].

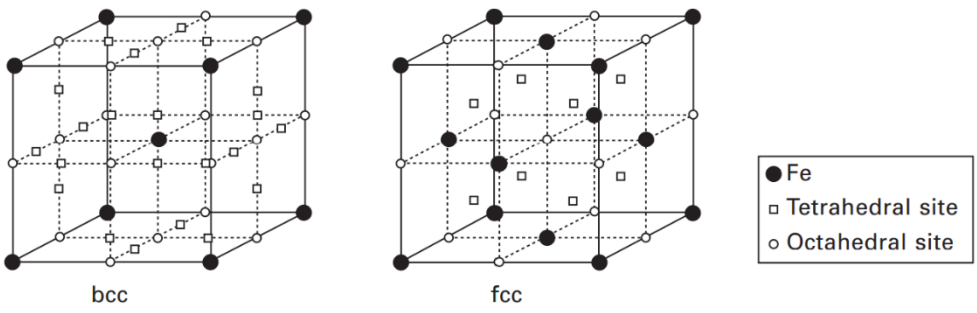

Figure 14. Illustration of tetrahedral and octahedral interstitial sites in bcc and fcc crystal structures [25]

Alloying has a significant impact on diffusible hydrogen in steels. Austenitic stainless steel, for example, shows a significantly lower heat of hydrogen solution (16 kJ/mol-H) than pure iron, related to a higher solubility. This increased solubility of hydrogen in austenitic stainless steels is associated with the crystal structure but also with alloying metals such as Ni and Cr, which change the precipitation of cementite and increase the solubility, thus decreasing the diffusivity. Furthermore, the literature indicates that numerous elements, including Co, Si, Cr, Al, Ni, Mo, V, and Ti, in solid solution reduce the hydrogen diffusivity in pure iron. Due to its binding energy with hydrogen, cementite exhibits a limited ability to trap hydrogen in low to medium-carbon steels [35]. Fig. 15 depicts a comparison of the solubility behavior of austenitic stainless steels and stainless ferritic steels [36]. Due to the fact that the diffusion rate in body-centered cubic lattices (bcc) is considerably higher than that in face-centered cubic lattices (fcc), ferritic and martensitic steels are often more prone to hydrogen-induced damage than austenitic steels. Furthermore, austenitic steels frequently exhibit an uneven distribution of hydrogen, which also denotes a low hydrogen diffusivity [12,36].

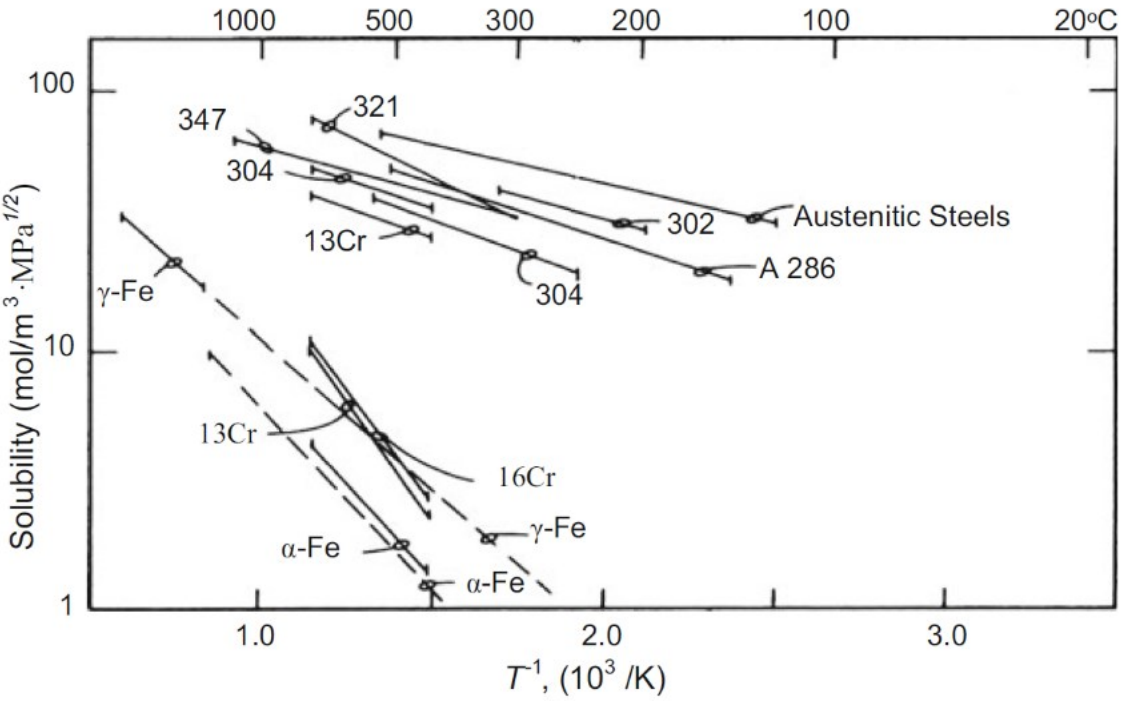

Figure 15. Solid solubility data of hydrogen in steels [36]

An ideal homogeneous material without traps is characterized by uniform depths of potential walls and their corresponding energy barriers between adjoining tetrahedral sites. In this case, the distribution of hydrogen atoms and their diffusion can be described using Fick's second law (assuming one-dimensional diffusion along the thickness of the specimen) [37]:

Fick's 1st law:

$$j = -DgradC \quad \text{(Eq.2)}$$

Fick's 2nd law:

$$\frac{\delta c}{\delta t} = D_H \nabla^2 \mathrm{C} \quad \text{(Eq.3)}$$

Where j expresses the flux, D_H describes the diffusion coefficient, and C refers to the concentration of diffusible hydrogen [37].

3.2.1 Numerical analysis of the diffusion coefficient

In practice, it is of great interest to use measured data from charging experiments to model numerical approximations for fitting theoretical charging curves and calculating the effective diffusion coefficient of hydrogen. Assuming that diffusivity remains constant during the charging process and diffusion is one-dimensional along the specimen thickness, Fick's law can be noted as a partial differential expression with associated boundary conditions as follows [20,38].

$$\frac{\partial c}{\partial t} = \frac{\partial^2 C}{\partial x^2}\mathrm{D} \quad \text{(Eq.4)}$$

$$\frac{\partial C}{\partial x}(\mathrm{x} = 0, \mathrm{t} \geq 0) = 0;\ \mathrm{c}(\mathrm{x} = \mathrm{r}, \mathrm{t} > 0) = \mathrm{C}_0;$$

$$\mathrm{c} = \mathrm{f}(\mathrm{x}),\ 0 < \mathrm{x} < \mathrm{r},\ \mathrm{t} = 0$$

Where x describes the position, t refers to the hydrogen loading time, D expresses the diffusion coefficient of hydrogen in steel, c(x, t) corresponds to the hydrogen concentration at time t at a distance x from the hydrogen-charging surface, and c_0 is the constant hydrogen concentration on the specimen surface [20] The boundary conditions are adapted to appropriate simplifications. For this purpose, a sample with a circular cross-section of radius r is assumed with a symmetrical concentration profile and constant potential during electrochemical hydrogenation [38,39].

The diffusion equation can be solved by inserting the boundary conditions and applying Laplace transformation, resulting in a time-dependent expression for the hydrogen concentration profile [20,38–40].

$$c_{ges} = C_0 - \frac{4C_0}{\pi}\sum_{n=0}^{\infty}\frac{(-1)^n}{2n+1}\exp\left\{\frac{-D(2n+1)^2\pi^2 * t}{4r^2}\right\}\cos\frac{(2n+1)\pi x}{2r} \qquad \text{(Eq.5)}$$

By integrating the concentration profile over the sample thickness, the final time-dependent equation of total hydrogen concentration is given as follows [40]:

$$c_{ges} = \frac{c_o}{r}\left(r\ erfc\left(\frac{x}{\bar{x}}\right)\right) - \frac{\bar{x}}{\sqrt{\pi}}e^{\left(\frac{-r}{\bar{x}}\right)^2} + \frac{\bar{x}}{\sqrt{\pi}} where\ \bar{x} = 2\sqrt{Dt} \qquad \text{(Eq.6)}$$

$$with\ c(x,t) = c_0 * erfc\frac{x}{2\sqrt{Dt}} \qquad \text{(Eq.7)}$$

In order to construct a theoretical saturation curve, the experimental data are used to determine the two unknown constants in the equation, i.e., the diffusion coefficient D and the surface concentration C_0. Subsequently, the calculated constants are used to fit a curve with all experimental data points.

L.Claeys et al. investigated a similar numerical approach based on Fick's second diffusion law for duplex stainless steels. They studied the evolution of total hydrogen content as a function of charging time until the concentration reached a saturation state. The data points that fit the curve best were found to have a diffusion coefficient of $2.1*10^{-14}$ m^2/s and a saturated hydrogen content of 650 ppm. By specifying the effective diffusion coefficient, the model gave a reliable indication of the saturation time, but it was insufficient to model the curve prior to actual saturation. In the figures below, the measured values and the constructed saturation curve are both depicted [39].

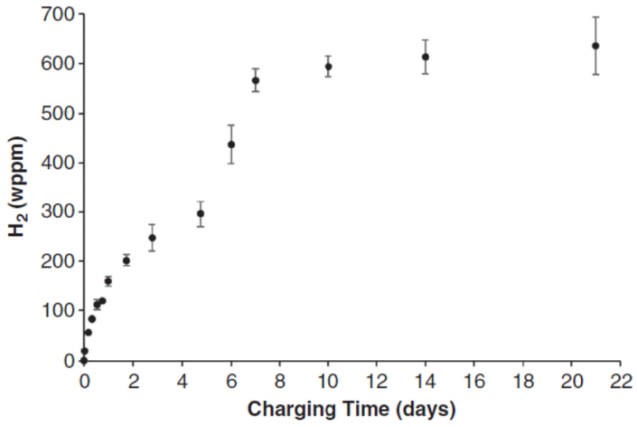

Figure 16. Hydrogen content as a function of charging time [39]

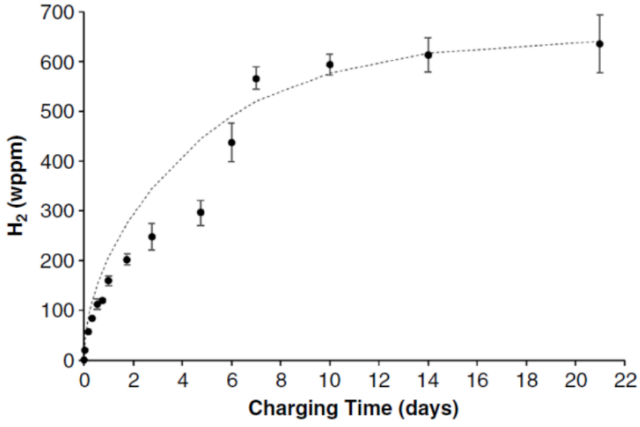

Figure 17. Theoretical fitted saturation curve according to Fick's law [39]

3.2.2 Temperature dependence of hydrogen diffusion

The increase in temperature and pressure promotes the kinetic energy of the atoms as well as the mobilization into the metal matrix, leading to enhanced solubility [33]. Another important aspect is the crystal structure of the steel, whose hydrogen solubility is represented in Fig. 18 as a function of temperature and pressure [41]. The diagram shows an increase in solubility accompanied by a rise in temperature during the transition from ferrite (α) to austenite (γ) and also results in a reduction of diffusivity. Conversely, the solubility decreases when austenite transforms into delta ferrite (δ). An increase in solubility is also observed for the liquid phase of iron when a temperature of 1600 °C is reached. The amount of hydrogen may then become up to 34 ppm at 1 atm. Due to relatively low hydrogen solubility at room temperature, rapid cooling of liquid iron to ambient temperature will cause the residual hydrogen content in the steel to exceed its solubility limit. The hydrogen content in the martensite phase corresponds to 0.4 ppm and therefore lies between the ranges of the ferritic and austenitic phase [41].

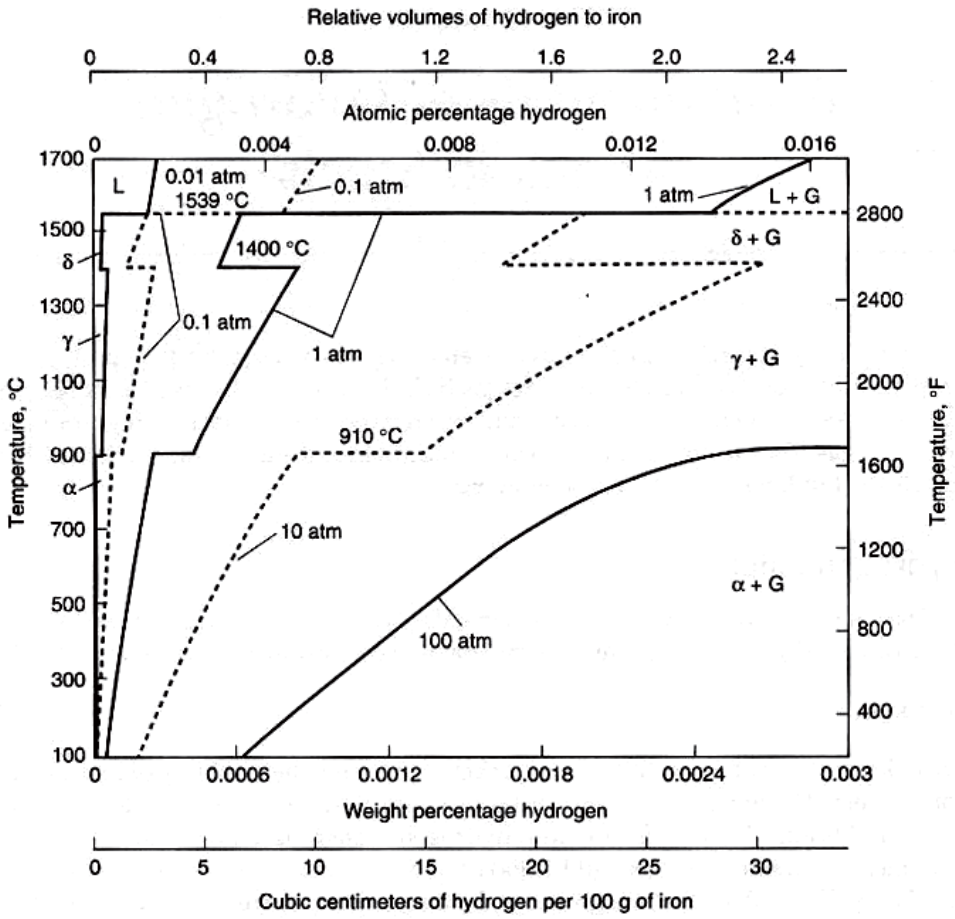

Figure 18. Solubility of hydrogen in steel as a function of temperature and pressure [41]

Since the solubility of hydrogen protons depends on the phase of the steel, different diffusion coefficients are obtained for specific steel grades as a function of temperature, illustrated in Fig. 19. The graph shows a significantly lower diffusivity for austenitic steel compared to carbon steel and duplex, especially for temperatures below 100 °C. Furthermore, ferrite exhibits the fastest diffusion of hydrogen at any temperature range [42].

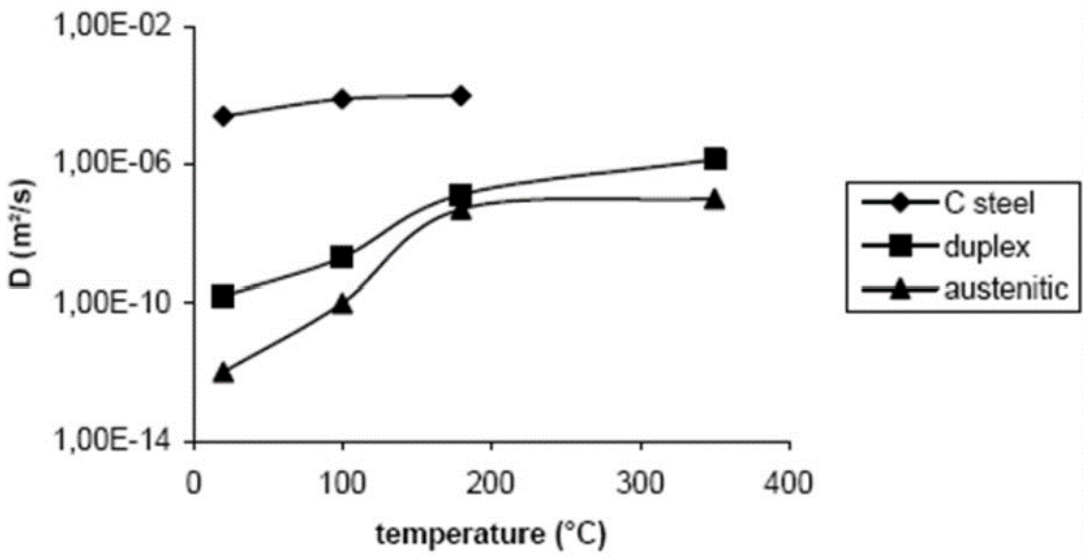

Figure 19. Hydrogen diffusion coefficient as a temperature function in different types of metals. [42]

Surface impedance and traps at lattice defects have a major impact on the measurement of the diffusion coefficient in a typical bcc iron lattice with already high hydrogen diffusivity. Kiuchi and McLellan [43] proposed equations that provide a valid approximation for the diffusion coefficient of hydrogen in a bcc iron in the absence of traps over a wide temperature range. The formulas were derived using a set of evaluated diffusion data from several measuring techniques [44]. The results showed that only data obtained electrochemically by H-Gas equilibration methods in ultrahigh vacuum, using Pd-covered membranes, are reliable [43]. The diffusion coefficient is best described for different temperature ranges by the following equations [43]:

The diffusion coefficient for a temperature range from -40°C to 80°C:

$$D = 7.23 * 10^{-8} exp\left(-\frac{5.69\left(\frac{kJ}{mol}\right)}{RT}\right) \quad [\frac{m^2}{s}] \qquad \text{(Eq.8)}$$

The diffusion coefficient for a temperature range from 50°C to 550°C:

$$D = (1\sim2.52) * 10^{-7} exp\left(-\frac{(6{,}7-7.12)\left(\frac{kJ}{mol}\right)}{RT}\right) \quad [\frac{m^2}{s}] \qquad \text{(Eq.9)}$$

The formulas provide the highest diffusion coefficient determined by the experimental methods. The differences in diffusivities correspond to the increasing fraction of H atoms that jump to octahedral sites instead of tetrahedral sites at elevated temperatures [43,44]. Fig. 20 shows a comparison of the determined diffusivities considering surface impedances and traps versus the data of the theoretical calculated coefficients without traps. The diagram indicates lower diffusivities in the regions C and D than the diffusivities in areas A and B expected from the calculations [44].

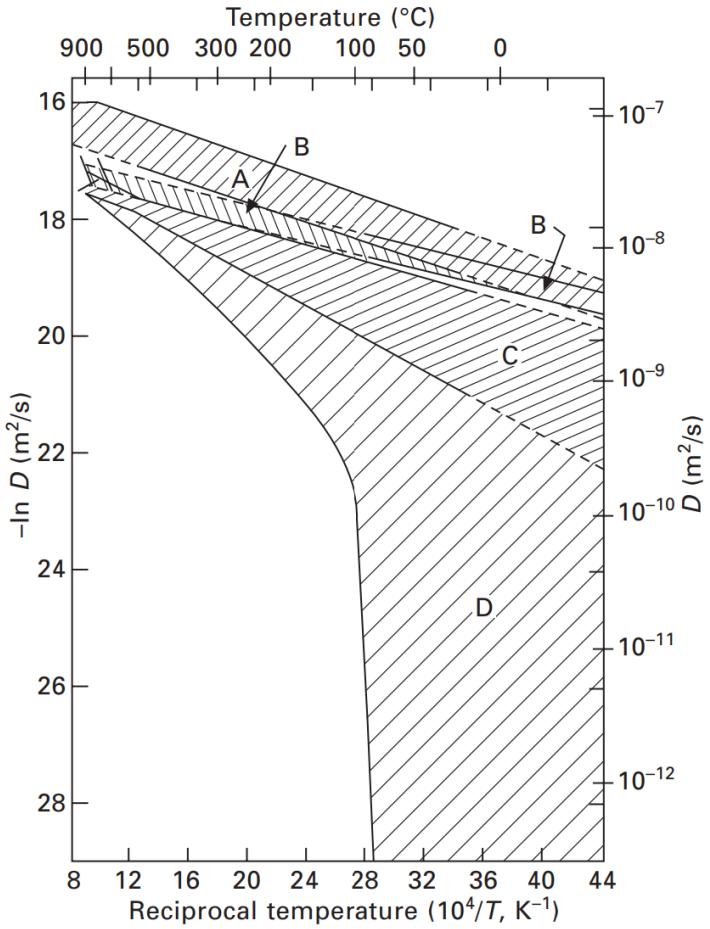

Figure 20. Diffusion coefficients in bcc iron as a function of the temperature [44]

Due to the additional hydrogen trapped in the lattice defects, the residence time of the diffusing hydrogen is prolonged, which leads to a lower diffusivity that is particularly evident at low temperatures. Therefore, the hydrogen concentration at the trap sites in local equilibrium with the hydrogen at the lattice sites must also be taken into account for an appropriate calculation of the diffusion coefficient [44]. Widely used models for this are based on the work of McNabb, Oriani, and Foster, who studied the phenomenon of diffusion associated with trapping sites influence [45]. However, this will not be discussed in detail in this work.

3.3 Permeation measurements and diffusion coefficient

3.3.1 Principle of electrochemical permeation

Electrochemical permeation measurements are conventionally performed according to the method developed by Devanathan and Stachurski. The experimental setup for this technique involves an electrochemical double cell divided into two compartments [46]. One of them acts as a charging cell and the other as a detection cell to measure the generated current of hydrogen oxidation. The cells are connected by a metal membrane (the specimen), as shown in the schematic setup in Fig. 21 [47,48]. Typically, a NaOH solution serves as an electrolyte for the detection side, and acidic (H_2SO_4), as well as neutral solutions (NaCl), can be used for the charging side [48]. Furthermore, the reduction compartment of the cells is operated galvanostatically, and the oxidation compartment potentiostatically. By applying a constant cathodic potential, hydrogen is introduced on the entry side of the specimen. The atoms diffuse through the membrane and are immediately oxidized by an applied potential as they leave the specimen on the detection side [46]. The recorded anodic oxidation current density is proportional to the diffusing amount of hydrogen and can be plotted as permeation transient as a function of time [49].

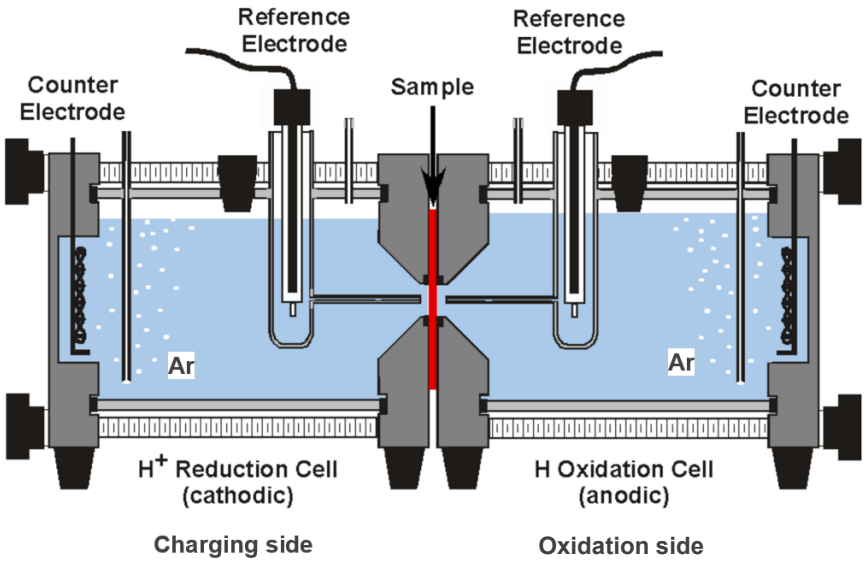

Figure 21. Illustration of a setup for electrochemical permeation [49]

Usually, the specimen is coated with a thin palladium film on the exit side to prevent the formation of an oxidation layer on the surface and ensure complete hydrogen oxidation [46]. Palladium coatings are essential for permeation measurement since the stability of the passive layer significantly controls diffusion and affects the results [48].

The obtained permeation curves permit a direct calculation of the hydrogen diffusion coefficient and further provide information about present traps and their energies in the material.

A typical permeation curve is demonstrated in Fig. 22 [35]. Throughout the measurement, there are three main phases consisting of trap filling, constant permeation rate, and saturation phase at a constant potential. Initially, the traps in the material are filled with hydrogen until an equilibrium concentration is established in the lattice. Following this, a constant concentration gradient in the sample leads to a constant permeation rate in the Pd layer until a critical hydrogen concentration is reached. Finally, a saturated state with constant potential evolves [50].

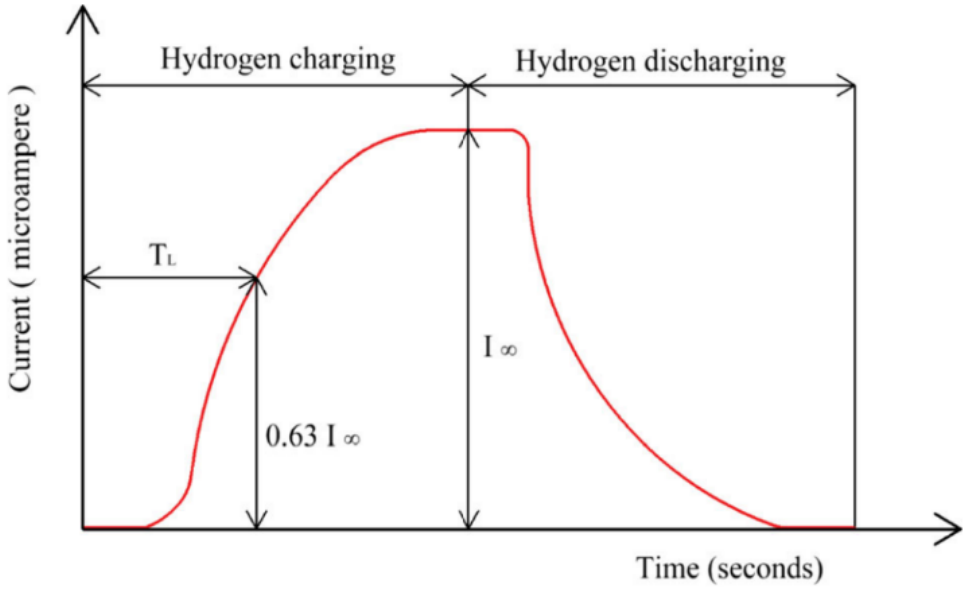

Figure 22. Permeation curve after one polarization [35]

Once a saturated state is reached, the cathodic current flow may be stopped, causing the oxidation current to decay in the hydrogen-discharging process. To prevent corrosion of the sample for additional measurements, the electrolyte in the cathodic compartment should be removed in the meantime and then refilled for the start of the next charging cycle [51]. The measurement of a second permeation curve allows the interpretation of reversible and irreversible traps in the material. During the first polarization, reversible and irreversible traps are filled. Since most of the irreversible traps are saturated after the first polarization, they do not effectively contribute to the second charge cycle [35]. The second permeation curve should therefore be lower than the one of the first polarization. In addition, the difference in the density of traps between the two charging cycles can be measured as the density of irreversible trapping sites. Fig. 23 presents such a permeation curve after two charging cycles [51].

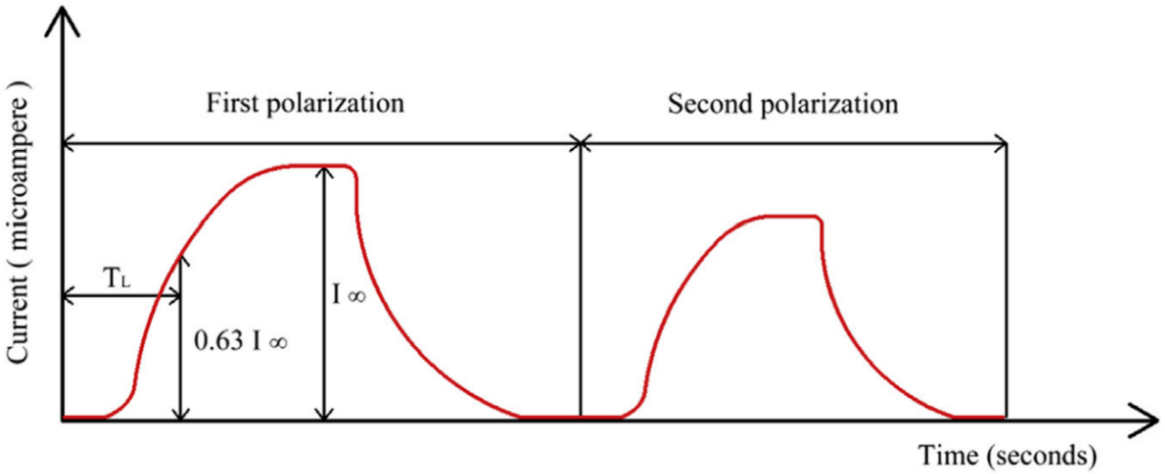

Figure 23. Typical permeation curve after two charging cycles [51]

3.3.2 Diffusion coefficient

The methods mentioned in the literature for the evaluation of the permeation curves propose the use of Fick's diffusion law. If one-dimensional diffusion is considered, the relationship between the transient permeation flux J(t) and the steady-state flux J_{ss} is influenced only by the diffusion coefficient D and the membrane thickness L (Eq.10). The diffusion coefficient can then be derived directly from the permeation curve using various methods [52]. There are three standard methods for this including the time lag method, the breakthrough method and the option of fitting the permeation curve according to Fick's law [53] (Fig. 24).

$$\frac{J(t)}{J_{ss}} = 1 + 2\sum_{n=1}^{\infty}(-1)^n \exp\left(-n^2\pi^2\frac{D*t}{L^2}\right) \qquad \text{(Eq.10)}$$

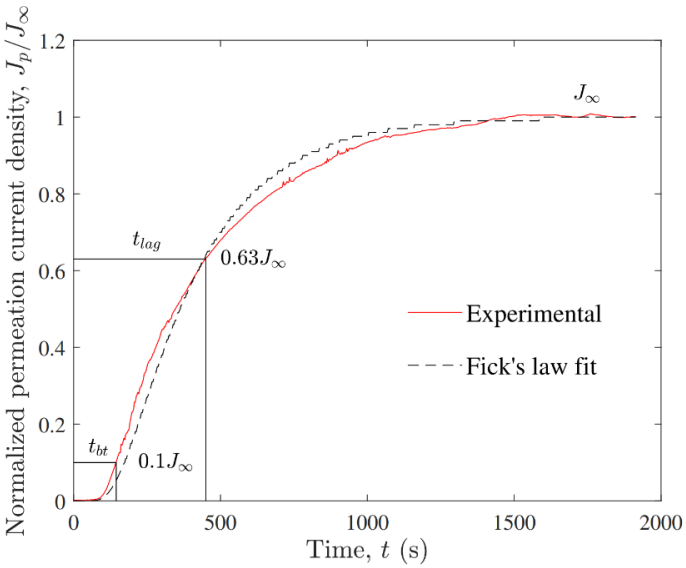

Figure 24. Permeation transient with different evaluation methods [53]

The general equation for the diffusion coefficient:

$$D = \frac{L^2}{M * t_{lag}} \quad \text{(Eq.11)}$$

3.3.2.1 Time lag method

This method is most widely used for the evaluation of permeation curves. The time lag corresponds to the time required for the oxidation current to reach 0.63 times the steady state current (Fig.24). Assuming L as specimen thickness and t_{lag} as characteristic time lag, the diffusion coefficient can be calculated by the following formula [53]:

$$\frac{J(t)}{J_\infty} = 0{,}63$$

$$D = \frac{L^2}{6 * t_{lag}} \quad \text{(Eq.12)}$$

3.3.2.2 Breakthrough method

In this method, the breakthrough time t_b is defined as the time required to reach 0.1 times the steady state current. It is also characterized as the time needed for the first hydrogen atoms to migrate completely through the membrane. The only difference in the formula is a another M-value [53].

$$\frac{J(t)}{J_\infty} = 0{,}1$$

$$D = \frac{L^2}{15{,}3 * t_b} \quad \text{(Eq.13)}$$

In both methods, a representation of the theoretical curves according to Fick's law is possible. Since hydrogen diffusion takes longer in the rising permeation curve, an M-value of 6 is usually selected, corresponding to 63% of the steady-state current density. However, if the focus of the measurement is on the hydrogen effusion during discharge, it is recommended to select a M-value of 15.3 suitable for 10% of the steady-state current density due to the fast effusion of the diffusible hydrogen at the beginning of the reaction during the decay curve [54].

3.3.3 Diffusion coefficients from literature

The Arrhenius plot can be used to illustrate and compare the diffusion coefficients derived from the permeation curves. This plot provides a large variety of measured hydrogen diffusion coefficients in the range of 10^{-9} to 10^{-4}cm^2/s in ferrite [55] (Fig. 25)

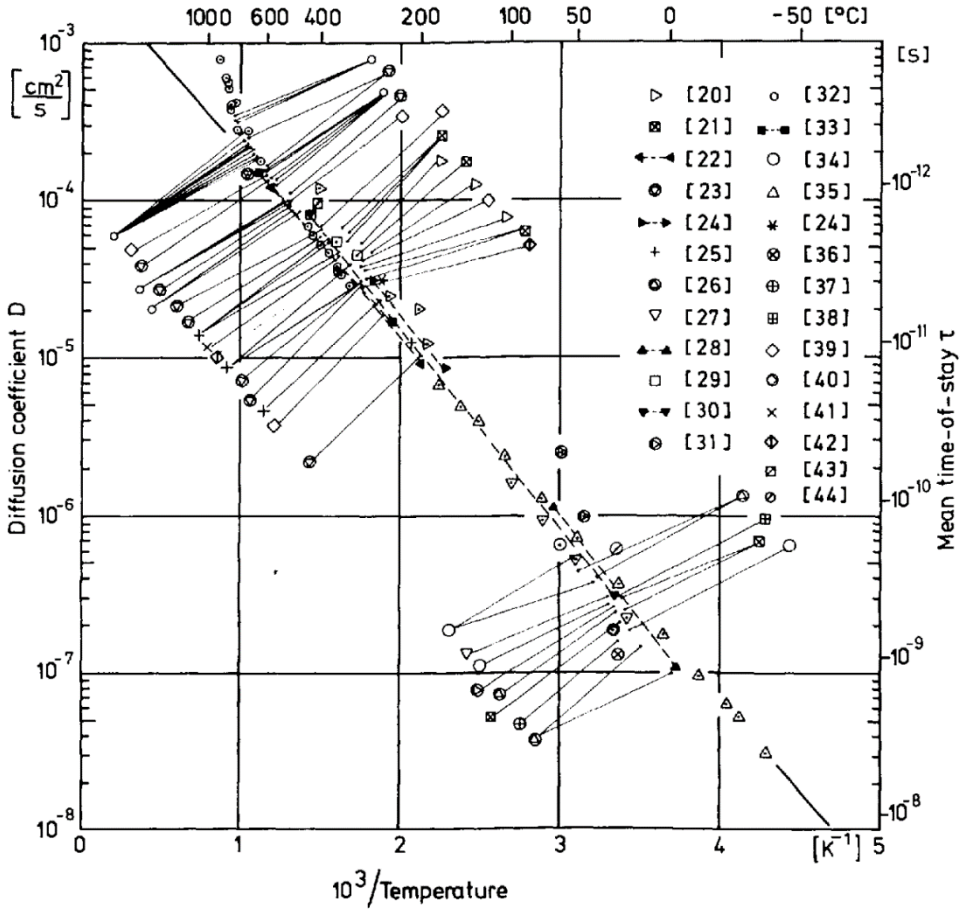

Figure 25. Arrhenius plot with diffusion coefficients of H in Pd coated ferrite [55]

Some values found in the literature for various diffusion coefficients obtained by permeation of commercial pipeline steels are given in Tab. 1 [56]. The metals were exposed to different electrolytes for the permeation measurements, and both the breakthrough method and the time lag method were used to calculate their diffusivity. The diffusion coefficients obtained for the palladium coated steel specimens are basically in the range of $1.5*10^{-11}$ - $9.4*10^{-10}$ m^2/s [56].

Table 1. Diffusion coefficients of pipeline steels found in the literature determined by permeation experiments [56]

Material	Solution	Coating	Method	D (10^{-10} m^2s^{-1})
X70	0.5 M H_2SO_4 + 250 mg/L $NaAsO_2$	Ni	Time lag	0.263
X100		Ni	Time lag	0.01
X65	NACE	Pd	Breakthrough	4.05 – 9.4
X70	NACE	Pd	Breakthrough	0.5 – 4.3
X52	NACE	Pd	Breakthrough	0.15 – 0.24
X65	0.1 M NaOH	-	Time lag	0.9-0.96
X65	NACE	-	Breakthrough	2.4
API	NACE	Pd	Breakthrough	3.5 – 9.5
X80	0.5 M H_2SO_4	Pd	Time lag	0.2
X70	0.1 M NaOH	Pd	Time lag	0.73 – 0.79

3.3.4 Pressure permeation

Since there is a possibility of extending the existing natural gas pipeline technology to the transport of hydrogen, the Oak Ridge National Laboratory wanted to gain a fundamental understanding of the effects of high-pressure hydrogen on steel properties. They developed a high-pressure test rig to evaluate the effects of temperature and pressure on permeation and subsequently formulate engineering guidelines for ensuring the integrity and safety of H_2 pipelines [57]. An internally heated pressure vessel was used for the implementation of in-situ testing under high-pressure hydrogen (Fig. 26) [57].

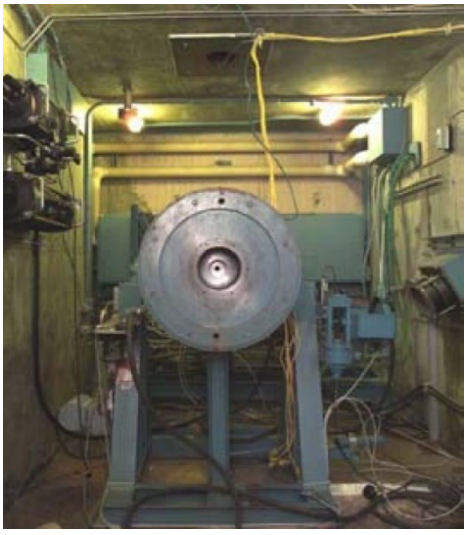

Figure 26. High-pressure testing rig up to 120,000 PSI and 1000°C [57]

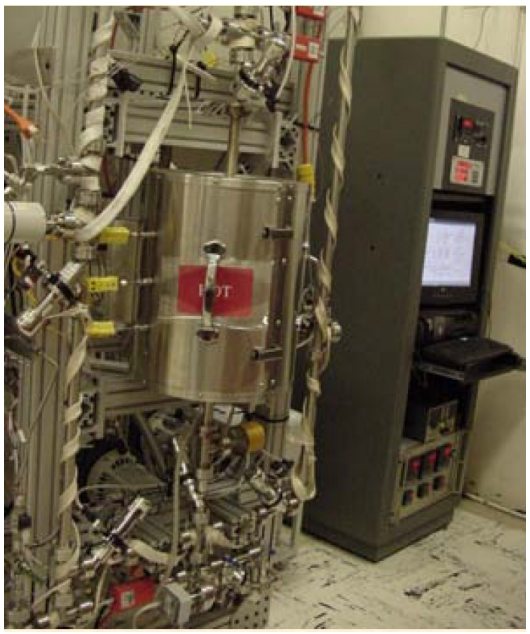

Figure 27. Low-pressure testing rig up to 1.3 bar and 500°C [57]

At the same time, low-pressure permeation tests were also conducted using a facility already developed by the Savannah River National Laboratory (Fig. 27). The tests were performed with X-52 and X-65 specimens at 1 bar differential pressure and 100°C. The material X-52 steel was used for high-pressure hydrogen permeation experiments at pressures up to 69 bar and a temperature of 170 °C. Basically, pressure permeation involves the hydrogen charging of the sample on the upstream side under maintained pressure (Fig. 28). Once diffused through the specimen, the hydrogen accumulates on the downstream side in a constant volume chamber where the pressure change over time is recorded (Fig. 29) [57].

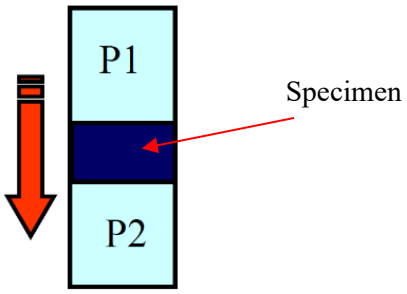

Figure 28. Principle of pressure permeation [57]

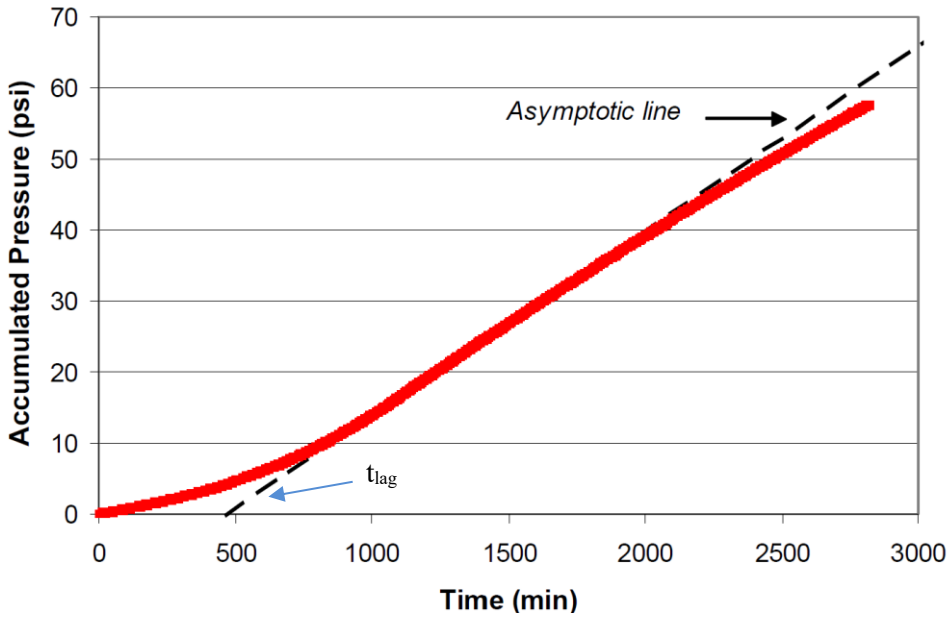

Figure 29. Pressure-time curve for X52 steel at H_2 charging condition of 38 bar and 170°C [57]

The time lag approach can be applied to calculate the effective diffusion coefficient by using the asymptotic slope line of the pressure-time curve:

$$D = \frac{l^2}{6 * t_{lag}} \quad \text{(Eq.14)}$$

Furthermore, the maximum hydrogen concentration on the upstream side is determined from the permeation rate and the effective diffusion of the steady state:

$$C_{max} = J_{ss} \frac{l}{D_{eff}} \quad \text{(Eq.15)}$$

Based on these measurements, diffusion coefficients for the low-pressure test were found to be $2.68*10^{-7}$ cm^2/s for X52 and $2.57*10^{-7}$ cm^2/s for X65. Moreover, at high-pressure permeation, diffusion coefficients of $1.95*10^{-6}$ cm^2/s at 69 bar and $2.66*10^{-7}$ cm^2/s at 38 bar were reported for X-52 steel. In general, the researchers concluded that an increasing pressure level leads to faster diffusion. However, they compared the pressure permeation method with electrochemical permeation and discovered lower diffusion coefficients for all experiments under gaseous H_2 charge compared to those measured by electrochemical permeation. The electrochemical permeations yielded an average coefficient of $5.2*10^{-6}$ cm^2/s at ambient temperature and $3.2*10^{-5}$ cm^2/s at 200°C. The diffusivity is thus one to two orders of magnitude higher than for the pressure permeations [57].

Chapter 4

HSE aspects related to hydrogen gas storage and transport

4.1 Hydrogen properties

If one considers working with hydrogen, it is of paramount importance to develop an understanding of the hazards that may arise and, even more important, how to manage them. The first section of this chapter provides an overview of the main properties of hydrogen, consequences in regard to gaseous hydrogen handling, and potential accidental kindling chain.

4.1.1 Gaseous hydrogen properties

At standard conditions, hydrogen is an odorless, colorless, non-toxic, tasteless, and highly combustible diatomic gas [58].

Following associated behaviors for gaseous hydrogen can be derived from Tab. 2 [58]:

- Due to its low density (by a factor of 14 lighter compared to air), it rises and disperses fast. As a result, high pressures are required to store vast amounts of hydrogen in the gaseous phase.
- Without external disturbance, the concentration of hydrogen will become entirely homogeneous due to its high diffusivity. But its dispersion is more affected by its high buoyancy than by its high diffusivity.
- There is a certain tendency to leak as a result of the low viscosity.
- There is a high potential for explosion or flame since hydrogen is combustible within a wide flammable range and requires a rather low ignition energy.
- Compared to Methane, the flame is less radiative, and the flame is colorless.
- Negative Joule Thomson effect, which means that during explosion, it is generating heat and has to be cooled before expansion.

Table 2. Hydrogen properties [58]

Properties	Numerical values
Molecular weight	2 g*mol^{-1}
Gaseous density at 273 K	0.0899 kg*Nm^{-3}
Diffusion coefficient in air	0.61 cm^2*s^{-1}
Compressibility factor	1.0006
Lower heating value	119.9 kJ*g^{-1}
Higher heating value	141.1 kJ*g^{-1}
Specific heat (C_p at 273 K)	14199 J*kg^{-1}*K^{-1}
Specific heat ratio (at 273 K)	1.4
Minimum ignition energy	20 μJ
Flammability range in air (upward propagation)	4-75% vol
Detonation range in air	13 – 65% vol
Flame velocity in air	260 cm*s^{-1}

4.2 Gaseous hydrogen hazards

Among potential hazardous events in hydrogen handling are hydrogen release and either immediate or delayed ignition of a flammable mixture of hydrogen and air or the rupture of vessels that are pressurized. If the case arises that hydrogen was accidentally released, several points must be taken into account to estimate the appropriate consequences. First of all, the pressure and the size of the release. Secondly, the environment in terms of confined space or free field. Thirdly, check potential ignition sources, and finally, in case of ignition, determine the type: immediate or delayed [58].

Hydrogen release in the free field with immediate ignition poses the risk of a so-called jet fire, as long as the source of hydrogen is not shut-off, these events are accompanied by thermal effects.

If the release takes place with a delayed ignition, the formation of a flammable cloud will take place prior to ignition. Once the flammable cloud is ignited, a deflagration is induced with overpressure effects which impact the surrounding workers and infrastructure [58,59].

If hydrogen is released in a confined space, it can result in an accumulation that is accompanied by certain hazards like pressure and thermal effects once the flammable mixture is ignited. Further hazards include the asphyxiation that may result from the displacement of breathable air via hydrogen, so-called oxygen depletion [59].

4.3 Utilization of existing natural gas infrastructure for hydrogen storage and transport

To accelerate the transition from natural gas to hydrogen storage, attempts have been made to utilize the already existing infrastructure, such as underground gas storage sites as well as natural gas transportation pipelines. The infrastructure is needed since hydrogen is ideally produced from renewable energy sources like wind and solar. To minimize the losses, an economically feasible way is to store the surplus energy in the form of hydrogen. If one wants to store considerably large amounts of hydrogen, among the most prominent candidates are subsurface containers, such as depleted gas reservoirs or salt caverns, which are already proven to be gas-tight [59]. This is their big advantage compared to saline aquifers, where the caprock integrity in terms of gas leakage is most likely not evaluated yet.

One of the most fundamental points in hydrogen storage is the geological integrity of the reservoir and the caprock. Usually, the porous caprock is water saturated and, therefore, hydraulically gas-tight until the capillary threshold pressure is reached. If one is not exceeding the fracture pressure of a depleted gas reservoir, the chance of leakage is minor since it has proven to be gas tight for million of years [59].

4.4 Integrity and reliability of material

In the case of subsurface hydrogen storage, the secure injection, as well as production, must be permanently guaranteed. Therefore, the main aspect is to avoid any leakage in both, the surface facilities as well as the subsurface equipment. Hence, borehole integrity is a fundamental aspect of geological hydrogen storage [60].

Thereby, the hydrogen resistance of materials utilized in borehole completions for underground gas storage may be divided into three major groups:

1. The integrity of steel alloys,
2. cement integrity in underground gas storage wells, and
3. elastomer and seal integrity.

The steel alloy integrity is of major importance since the inner casing, tubing, packer, subsurface safety valve, and so on are in direct contact with the injected and produced media. Several studies have been undertaken to study the impact of hydrogen on steel alloys. The influences that have a direct impact on the properties of steel alloys are hydrogen induced cracking, hydrogen blistering and hydrogen embrittlement. Temperature, hydrogen concentration, pressure, and stress fields are, besides the main properties of steel, able to influence the previously mentioned phenomena [60].

Stress changes in the borehole completion are critical, especially pressure and thermal changes during the operation can result in an acceleration of hydrogen embrittlement in the tubing.
Another major point is cement integrity. The cement provides a connection between the formation and the casing. Among the main challenges are the prevention of any gas leakage via the cement bond, the proper anchorage of the casing, and the stabilization of the borehole. It is of highest importance that the gas cannot diffuse through the cement into other formations or to the surface. Another focus must be put on the investigation of chemical cement changes due to exposure to hydrogen.
Finally, the elastomer and seal integrity is a key component in terms of underground hydrogen storage. Elastomers and seals are used in packers, as well as fittings, to seal off the annulus between casing and tubing. Usually, the used elastomers and seals are proven to be hydrogen resistant. Anyway, it is important to investigate if hydrogen diffusion takes place [60].

4.5 Further risks

Another potential risk that comes along with hydrogen storage in subsurface formations are geochemical reactions with rock minerals and the resident reservoir fluid. This poses several risks, on the one hand, it may lead to energy losses, which would reduce the storage efficiency, and on the other hand, the reaction with rock minerals may lead to formation damage, which is commonly accompanied by alteration of crucial reservoir properties like porosity and permeability [60].
Hydrogen may react with carbonates, and further reactants are oxygens, sulfides, and sulfates. Usually, these reactions are considered slow, and the reservoir temperature may not be sufficient to activate these reactions, but microorganisms may serve as a kind of catalyst for such operations.
Besides that, numerous microorganisms are in the reservoir, either living there naturally or artificially introduced in the course of the drilling operation [59,60]. These microorganisms can trigger several anaerobic metabolic processes. Methanogenic, sulfate-reducing, and acid-forming prokaryotes are among the most prominent. Thereby, hydrogen serves as an electron donator. Popular reactions include the methanation reaction, where hydrogen and carbon dioxide react to form methane and water [60].

Chapter 5

Experimental section

5.1 Materials

The materials investigated were ARMCO pure iron and three types of carbon steels commonly used in the oil and gas industry. The three carbon steel grades were J55, L80, and P110, according to API 5CT requirements. Moreover, the specimens were manufactured from provided casing segments. Since pure iron is relatively free of impurities and alloying components that might act as additional hydrogen traps, it was chosen as a comparable material.

5.1.1 Chemical analysis

The following tables provide information about the chemical composition of the test materials obtained by emission spectrometry (Tab. 3-Tab. 6).

Table 3. Chemical composition of ARMCO ™ iron in wt%

	Chemical composition in wt %							
Material grade	**C**	**Si**	**Mn**	**P**	**S**	**Cr**	**Ni**	**Mo**
ARMCO™- iron	0,02	<0,01	0,05	0,006	0,002	0,03	0,03	0,01
	Co	**Al**	**Sn**	**W**	**N_2**	**Cu**		
	<0,01	0,029	0,001	<0,01	0,0044	0,01		

Table 4. Chemical composition of J55 in wt%

	Chemical composition in wt %							
Material grade	**C**	**Si**	**Mn**	**P**	**S**	**Cr**	**Ni**	**Mo**
J55	0,32	0,21	1,33	0,014	0,008	0,25	0,04	0,01
	Co	**Al**	**Sn**	**W**	**N_2**	**Cu**	**Ca**	
	0,01	0,029	0,002	<0,01	0,0063	0,01	0,0015	

Table 5. Chemical composition of P110 in wt%

	Chemical composition in wt %							
Material grade	**C**	**Si**	**Mn**	**P**	**S**	**Cr**	**Ni**	**Mo**
P110	0,33	0,20	1,39	0,013	0,014	0,42	0,03	0,01
	Co	**Al**	**Sn**	**W**	**N_2**	**Cu**	**Ca**	
	0,01	0,028	0,002	<0,01	0,0054	0,01	0,0011	

Table 6. Chemical composition of L80 in wt%

	Chemical composition in wt %							
Material grade	**C**	**Si**	**Mn**	**P**	**S**	**Cr**	**Ni**	**Mo**
L80	0,32	0,20	1,34	0,018	0,007	0,24	0,03	0,01
	Co	**Al**	**Sn**	**W**	**N_2**	**Cu**	**Ca**	
	0,01	0,030	0,003	<0,01	0,0065	0,03	0,0016	

Several elements were detected in small amounts in the composition of the pure iron, which most likely arise as impurities during the manufacturing of ARMCO iron. Among the various alloying elements detected in carbon steels, those with the highest content were carbon (C), silicon (Si), manganese (Mn), and chromium (Cr). Theoretically, the solubility for hydrogen should be higher in the carbon steels than in pure iron since these steels exhibit a higher alloy content.

5.1.2 Mechanical properties

The obtained mechanical properties of the materials include the hardness according to Vickers and the resulting tensile strength. ARMCO iron shows the lowest hardness and tensile strength, and carbon steel P110 presents the highest hardness value with the associated tensile strength (Tab. 7).

Table 7. Determined hardness and tensile strength of all materials

Material	Hardness [HV 1]	Ultimate tensile strength (UTS) [MPa]
ARMCO iron	88	282
J55	177	566
L80	328	1050
P110	340	1088

5.1.3 Microstructure

The following figures present the microstructures of longitudinal and transverse cross sections of all the materials investigated. Fig. 30 depicts the microstructure of ARMCO iron in longitudinal and transverse directions within an average grain size of ferrite of about 100 µm. The cross sections of J55 are shown in Fig. 31 and exhibit a ferritic-pearlitic microstructure with a grain size smaller than ARMCO iron of approximately 30 µm. In Fig. 32, L80 shows a microstructure of tempered martensite and portions of retained austenite with a grain size of roughly 20µm. The microstructure of P110 is demonstrated in Fig. 33 and also indicates a tempered martensite phase with an average grain size of 15µm. The microstructures of L80 and P110 have smaller grain sizes than J55 and ARMCO iron, implying a higher amount of traps within the material.

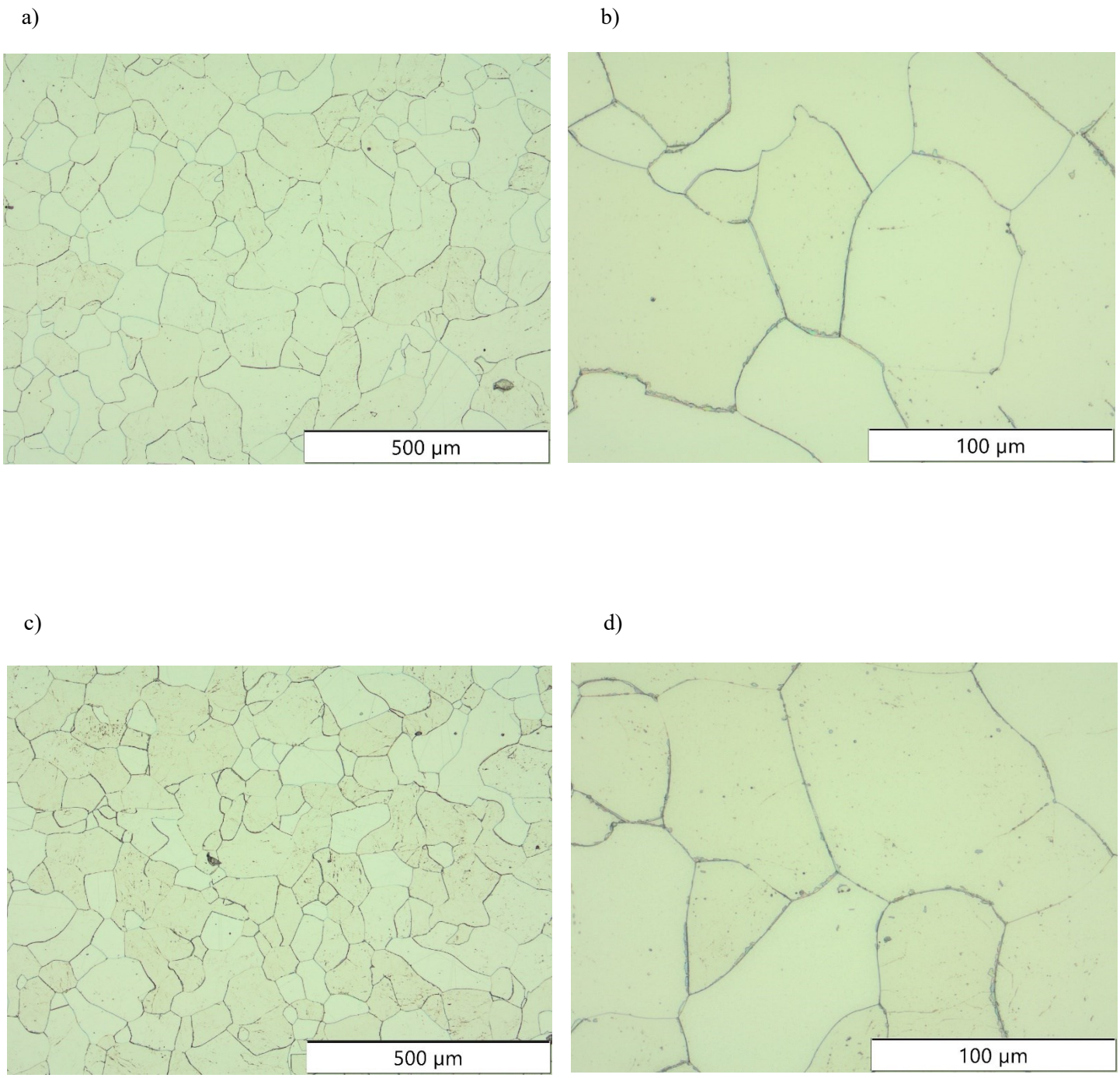

Figure 30. Microstructure of ARMCO iron: a) longitudinal cut at 100x magnification, b) longitudinal cut at 500x magnification, c) transverse cut at 100x magnification and d) transverse cut at 500x magnification

a)

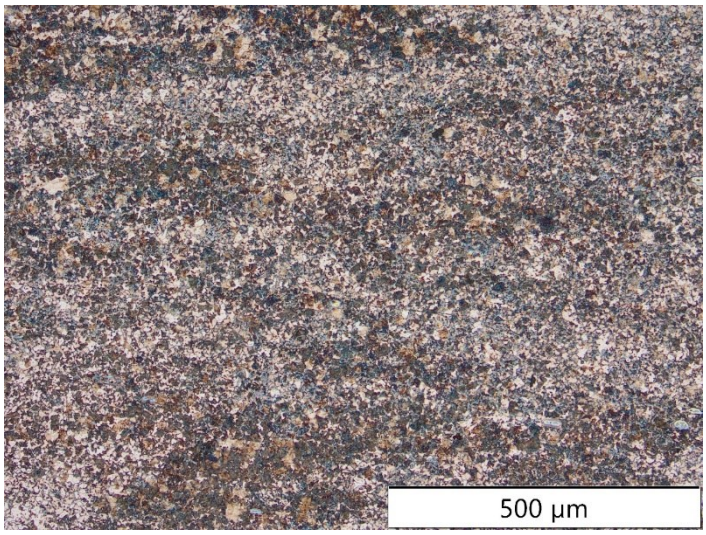

b)

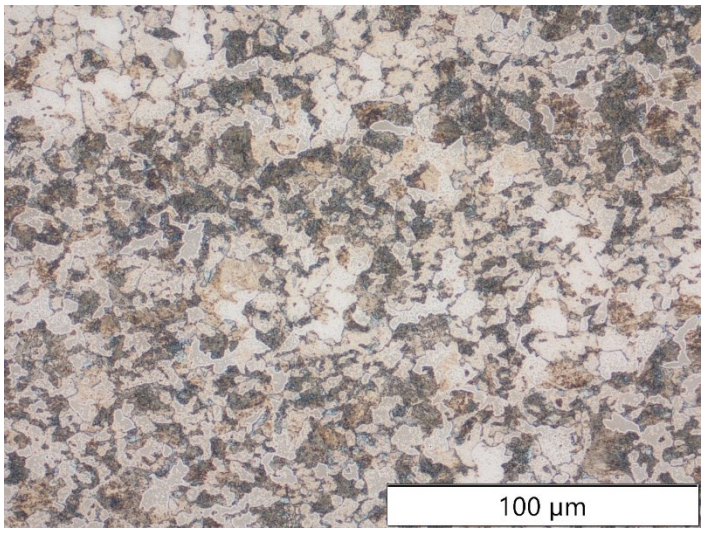

c)

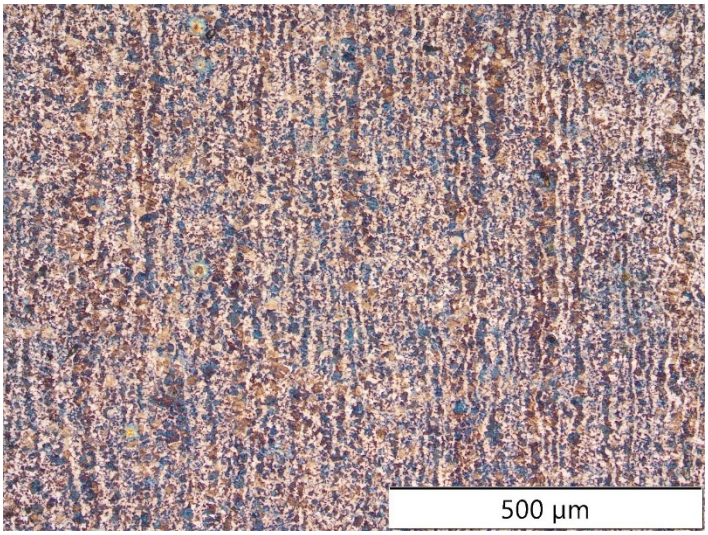

d)

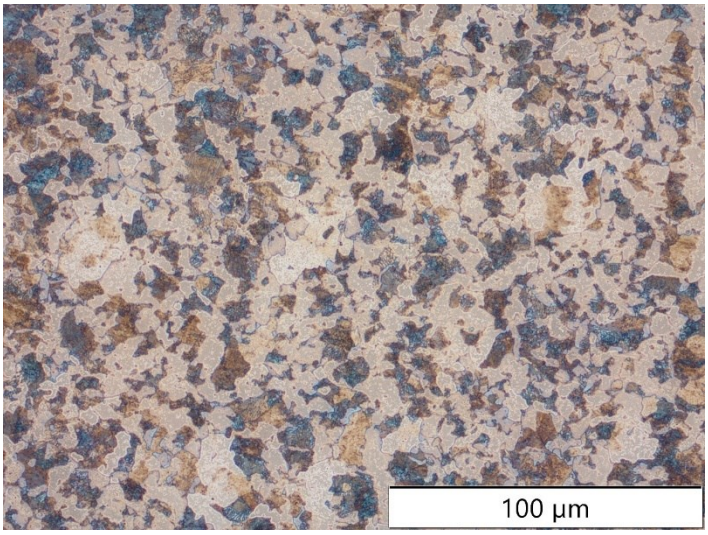

Figure 31. Microstructure of J55: a) longitudinal cut at 100x magnification, b) longitudinal cut at 500x magnification, c) transverse cut at 100x magnification and d) transverse cut at 500x magnification

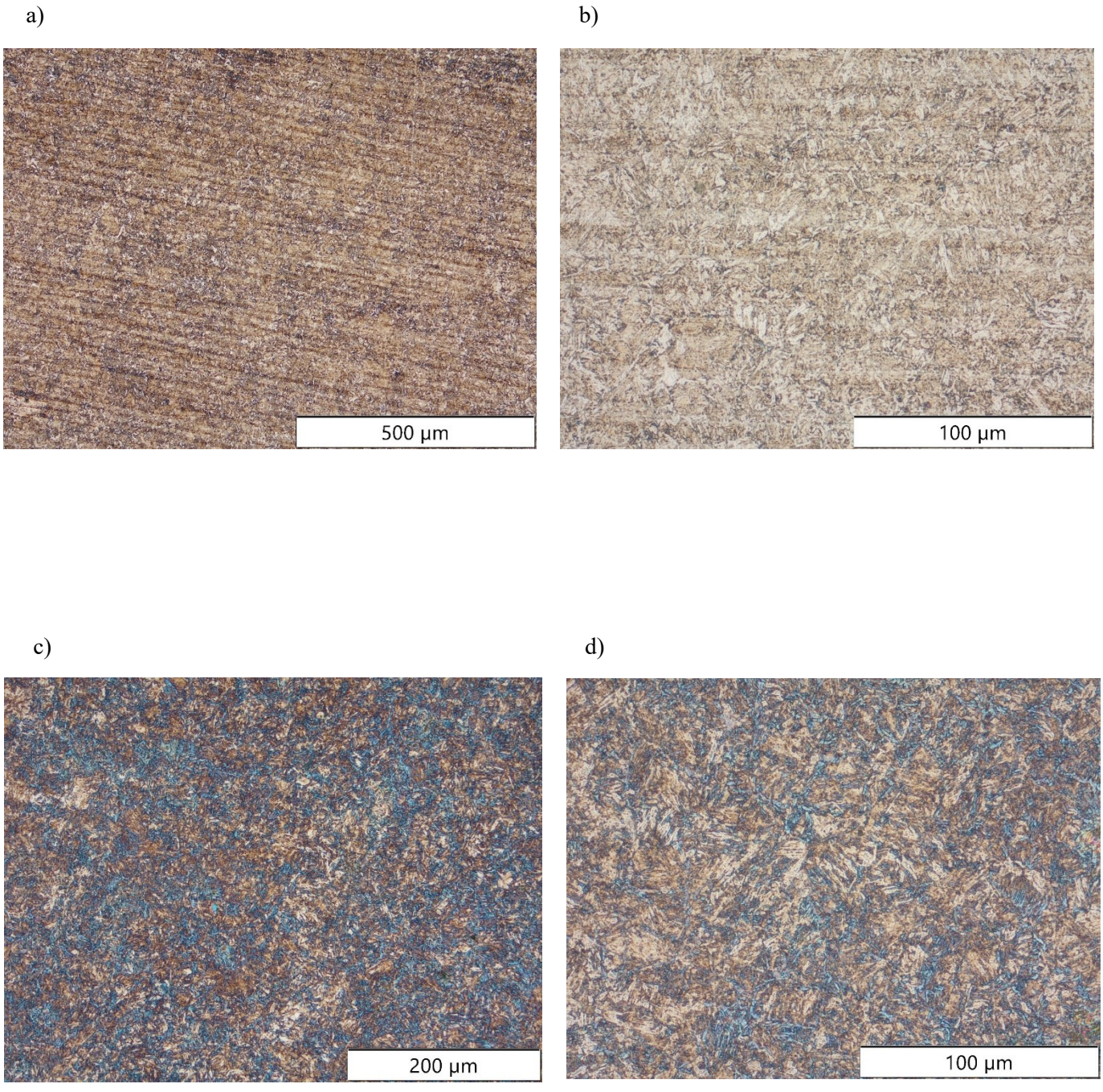

Figure 32. Microstructure of L80: a) longitudinal cut at 100x magnification, b) longitudinal cut at 500x magnification, c) transverse cut at 200x magnification and d) transverse cut at 500x magnification

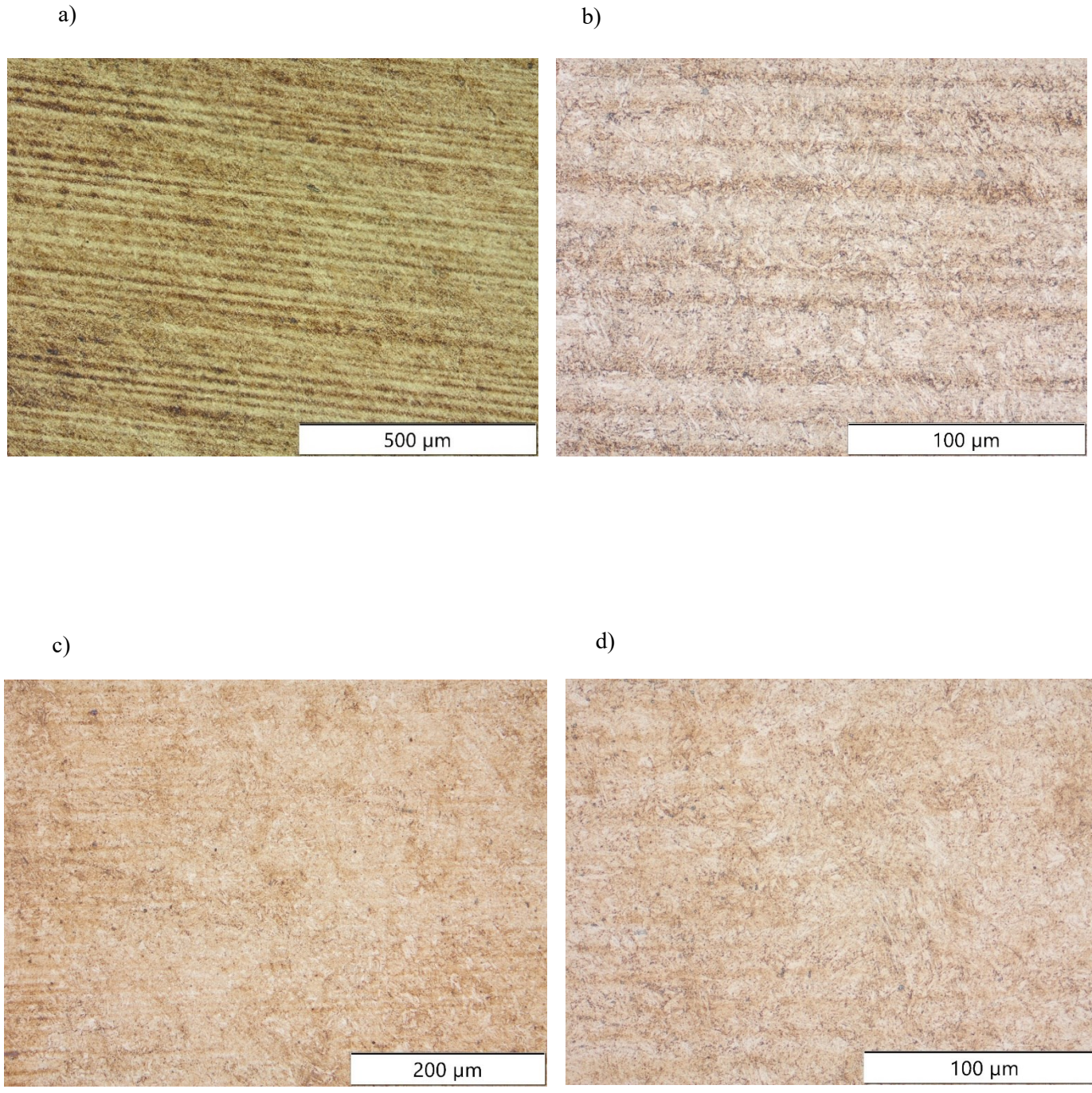

Figure 33. Microstructure of P110: a) longitudinal cut at 100x magnification, b) longitudinal cut at 500x magnification, c) transverse cut at 200x magnification and d) transverse cut at 500x magnification

5.2 Hydrogen charging

All charging experiments were conducted with a specimen dimension of 30x6x6 mm at ambient temperature conditions (Fig. 34). In order to evaluate the hydrogen saturation, two samples of any material were charged at each condition for a test duration ranging from one hour to 168 hours. Following that, the hydrogen content of all specimens was measured, and based on the experimental data, saturation curves were generated using a numerical method as described in chapter 3.2.1 to compare the diffusion coefficients for all test conditions.

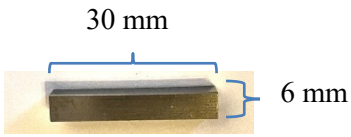

Figure 34. Specimen dimensions for hydrogen charging

5.2.1 Immersion testing

The immersion tests were performed in a neutral NaCl solution with thiourea added for 1 hour to 72 hours. The experimental setup is shown in Fig. 35.

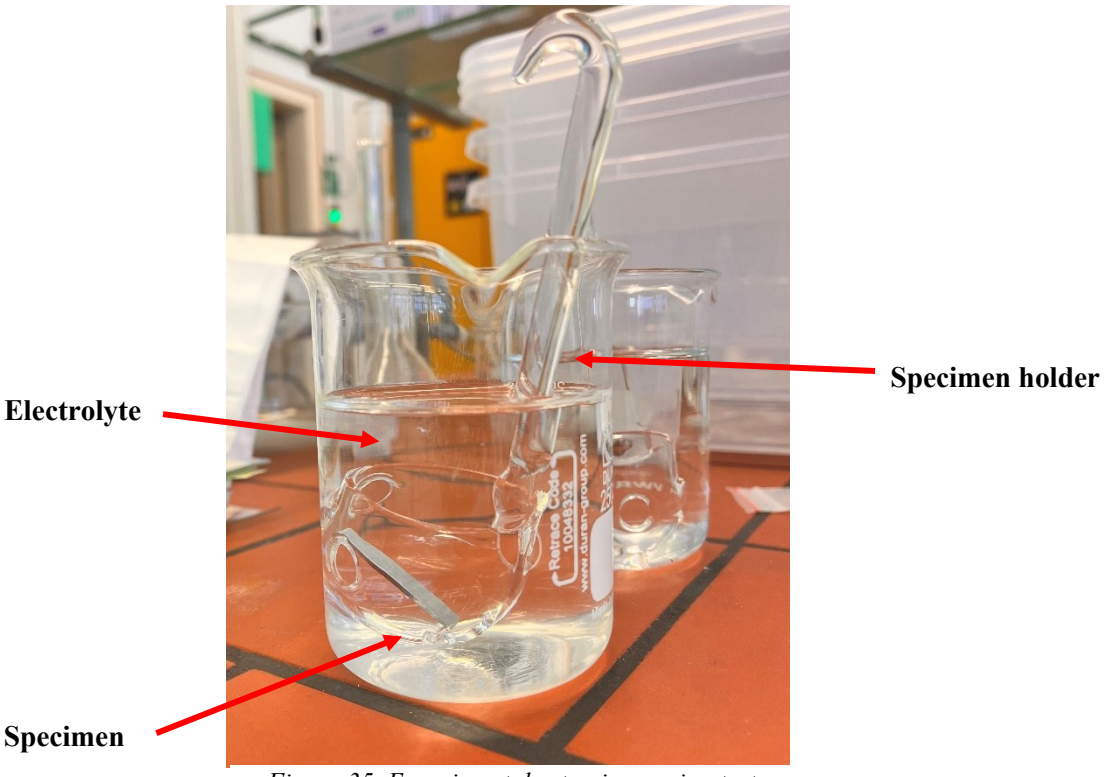

Figure 35. Experimental setup immersion test

The charging conditions are given in the table:

Table 8. Charging conditions

Electrolyte	3.5% NaCl + 1 g/L CH_4N_2S
Charging time	1h – 72h
Temperature	25°C

Prior to charging, the specimen was placed in an acetone-filled beaker and purged in an ultrasonic bath. The sample was then immersed in a 400ml electrolyte solution fixed by a sample holder. Once the predetermined charging time elapsed, the sample was removed from the solution, rinsed with acetone, and immediately cooled in liquid nitrogen to prevent hydrogen diffusion. Without prolonged exposure, the specimen was then wet grinded and instantly cooled again in liquid nitrogen until the hydrogen analysis process.

5.2.2 Cathodic charging

During cathodic charging, the samples were charged under galvanostatic charging conditions at a cathodic current density of 1 mA/cm^2 in a 3.5% NaCl solution with thiourea added, acting as a recombination inhibitor. The experimental setup is presented in Fig. 36, and the charging conditions are given in Tab. 9.

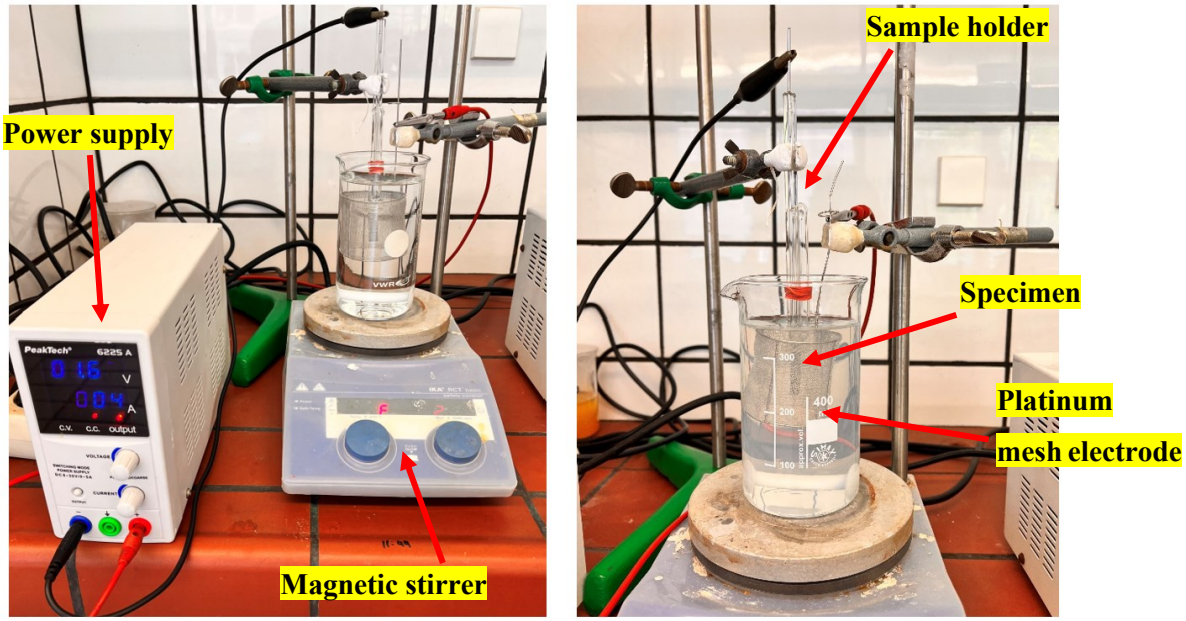

Figure 36. Experimental setup for cathodic charging

Table 9. Charging conditions

Electrolyte	3.5% NaCl + 1 g/L CH_4N_2S
Current density	1 mA/cm^2
Charging time	1h – 72h
Temperature	25°C

Prior to cathodic charging, the sample was purged in an ultrasonic bath while immersed in acetone. The specimen served as the working electrode and was immersed in a 400 ml electrolyte solution fixed by a sample holder, while a cylindrical Pt mesh electrode was used as a counter electrode that enclosed the specimen. Throughout the experiments, the electrolyte was circulated using magnetic stirrers. When the charging process was completed according to the predefined charging period, the sample was removed from the solution, rinsed with acetone, and immediately cooled in liquid nitrogen. The sample was then wet grinded and rapidly cooled again in nitrogen until hydrogen analysis was performed.

5.2.3 Autoclave tests

Autoclave tests were performed for charging times from 1 hour to 168 hours to evaluate the hydrogen uptake in all materials under gaseous hydrogen at high-pressure conditions. As for the other charging experiments, the samples were immersed in acetone and rinsed in an ultrasonic bath before hydrogen charging. Following that, four to eight specimens were placed in an autoclave at the same time. The illustration (Fig. 37) depicts a used autoclave, and Tab. 10 provides the test conditions for gaseous hydrogen charging.

Figure 37. Illustration of an autoclave used [61]

Table 10. Charging conditions

Test medium	Dry H_2 gas
Hydrogen pressure	100 bar
Charging time	1h – 168h (7 days)
Temperature	25°C

Once the specimens were positioned within the autoclave, it was evacuated several times and purged with argon to remove influences of oxygen and other atmospheric gases. After successful evacuation and purging, the autoclaves were filled with hydrogen gas under dry conditions at a pressure of 100 bar. All charging experiments were run statically, and after completion of the charging period, the test gas was released from the autoclave prior to sample removal. Following the withdrawal of the samples, they were immediately cooled in liquid nitrogen until the hydrogen analysis was conducted.

5.2.4 Hydrogen analysis

Throughout all charging experiments, the total hydrogen content of the samples was analysed after charging in a thermal conductivity cell using hot carrier gas extraction at a temperature of 950°C. In this procedure, an ELTRA H-500 hydrogen analyzer was used, as shown in Fig. 38. The previous grinding process of the specimen ensured that there were no corrosion products or other deposits on the surface that could affect the results. To initiate the analysis, the specimen was first rinsed with acetone, then weighed and placed in the cold zone of the horizontal oven. After starting the analysis, the furnace was rotated to a vertical position so that the specimen fell into the hot zone. By adding nitrogen as a carrier gas, the hydrogen is extracted from the sample and transferred to a sensitive thermal conductivity cell. The hydrogen content was then calculated by the device and expressed in ppm. The calibration gas used was helium with a thermal conductivity equal to 7.7 ppm hydrogen. Furthermore, it is recommended to use samples with a mass greater than 2 g for the analysis, as preliminary tests with lighter and smaller sample dimensions have shown inaccurate results and significant fluctuations in the measurement.

Figure 38. ELTRA H-500 analyser for residual hydrogen content measurements

5.3 Hydrogen permeation

The permeation measurements were carried out in three different ways. For both, the electrochemical permeation and permeation at open circuit potential, specimens with dimensions of 40x40x1mm were used. In the case of pressure permeation, the specimens examined were circular in shape with a diameter of 27 mm and a thickness of 1 mm (Fig. 39). Moreover, all experiments were performed at ambient temperature conditions. For the evaluation of the permeation curves and the direct calculation of the diffusion coefficient, the time-lag method described in chapter 3.3.2.1 was used. Based on the starting time of the charging cycle, the time lag was identified from the curve where the oxidation current was 63% of the steady-state current value.

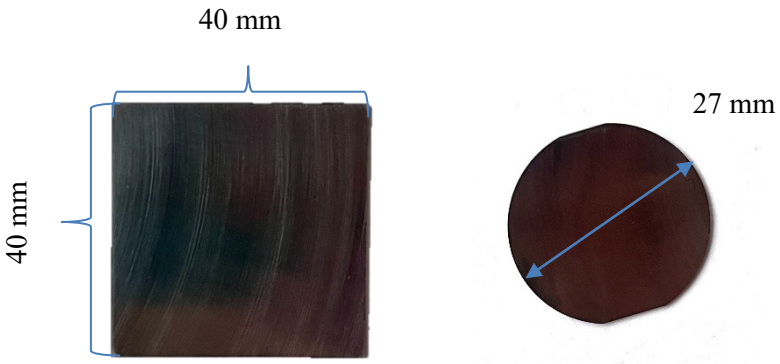

Figure 39. Specimen dimensions for permeation: Left electrochemical and right pressure permeation

5.3.1 Electrochemical permeation

Electrochemical permeation experiments were performed using specimens of all materials with dimensions of 40x40x1 mm, coated with a palladium layer. The experimental setup involves a double cell, according to Devanathan and Stachurski, and is shown schematically in Fig. 40.

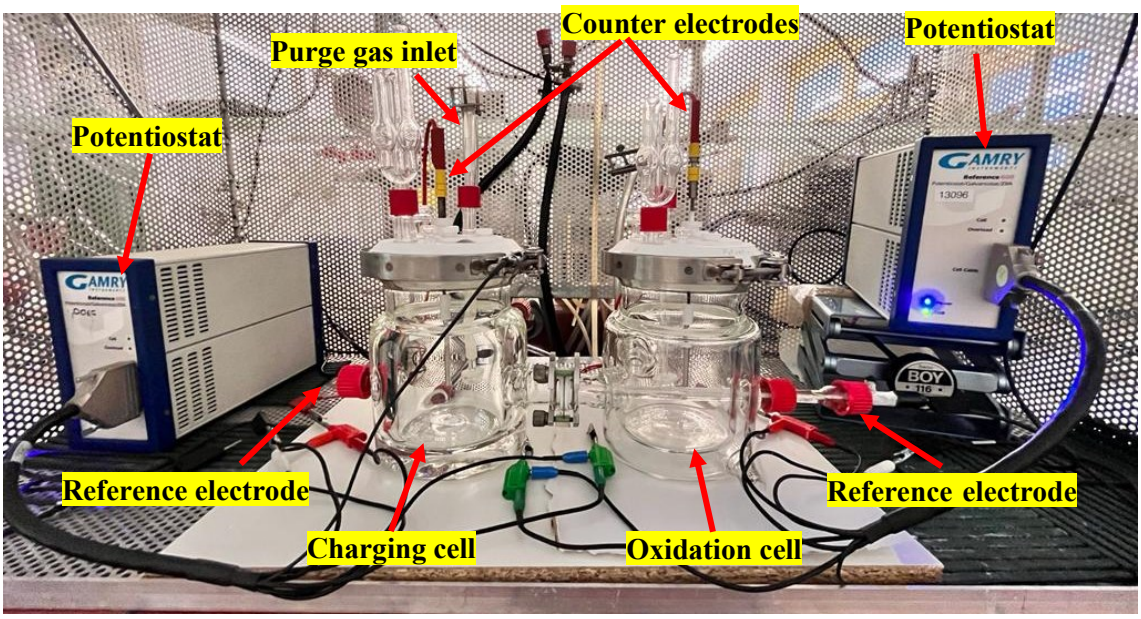

Figure 40. Experimental setup for electrochemical permeation

The experimental conditions for electrochemical permeation are listed in Tab.11:

Table 11. Electrochemical charging conditions

Electrolyte charging cell	3.5% NaCl + 1g/L CH_4N_2S
Electrolyte oxidation cell	0.1M NaOH
Temperature	25°C
Current density	1mA/cm^2
Sample thickness	1 mm
Sample coating	Pd on the oxidation side
Sample area	1 cm^2
Counter electrode	Pt
Reference electrode	Ag/AgCl
Gas purging	Ar

Prior to the permeation measurement, the specimen was rinsed in acetone in an ultrasonic bath.
The sample coated with palladium was positioned between two glass cells and fixed to a clamping device. The electrolyte used in the loading cell was a 3.5 % NaCl solution with thiourea added and a 0.1M NaOH solution in the oxidation cell. In both cells, platinum served as the counter electrode and a silver-silver chloride electrode as the reference electrode. Besides that, the specimen acted as the working electrode. The capillary of the reference electrode was conductively sealed at the front with agar-agar and filled with saturated potassium chloride solution. The temperature of the two compartments was kept constant at room temperature via a circulating thermostat for the entire duration of the experiment. Furthermore, the electrolyte solutions were gassed with argon at least 24 hours before starting the permeation measurement, and the solutions in the cells were also purged during the experiment to eliminate the influence of oxygen. A Gamry reference 600 potentiostat was used for recording the oxidation current as well as for setting a constant charging current. At the beginning of the experiment, the oxidation cell was filled with the NaOH solution, and an oxidation potential of +0.35V was set against the Ag/AgCl electrode. Once a stable potential level was established, the charging cell was filled with the 3.5% NaCl solution with thiourea added, and a cathodic charging current of $1 mA/cm^2$ was applied to initialize the permeation measurement. Throughout the measurement, the oxidation current increased and achieved a stable plateau after a specific time. When a constant current value was reached, the cathodic current supply was interrupted, followed by the removal of the electrolyte solution from the charging cell, causing the oxidation current to drop in the discharge process. The resulting decay curve achieved a constant level after a while before a second loading cycle could be performed. As in the procedure of the first measurement, the charging cell was refilled with the electrolyte, and a constant cathodic current was applied. An increase of the oxidation current was observed, which became a constant value after some time. The experiment was terminated after recording both loading curves and a decay curve, and the specimen was removed.

5.3.2 Permeation at open circuit potential

Permeation experiments at open circuit potential were performed with the same setup as for electrochemical permeation. However, in this method, only the potentiostat on the oxidation side was used, and the sample was not subjected to galvanostatic charging. In the procedure of this technique, the same electrolytes and conditions were used as in the electrochemical permeation, and the experiment was conducted according to the same steps, except that no current was applied as a driving force on the charging side. Moreover, the objective of the experiment was to measure only one charging cycle for each specimen.

5.3.3 High pressure permeation

A setup consisting of a permeation glass cell and a modified autoclave was developed to perform pressure permeation with gaseous hydrogen at 100 bar. The experimental conditions are given in Tab. 12. The experimental setup is illustrated in Fig. 41.

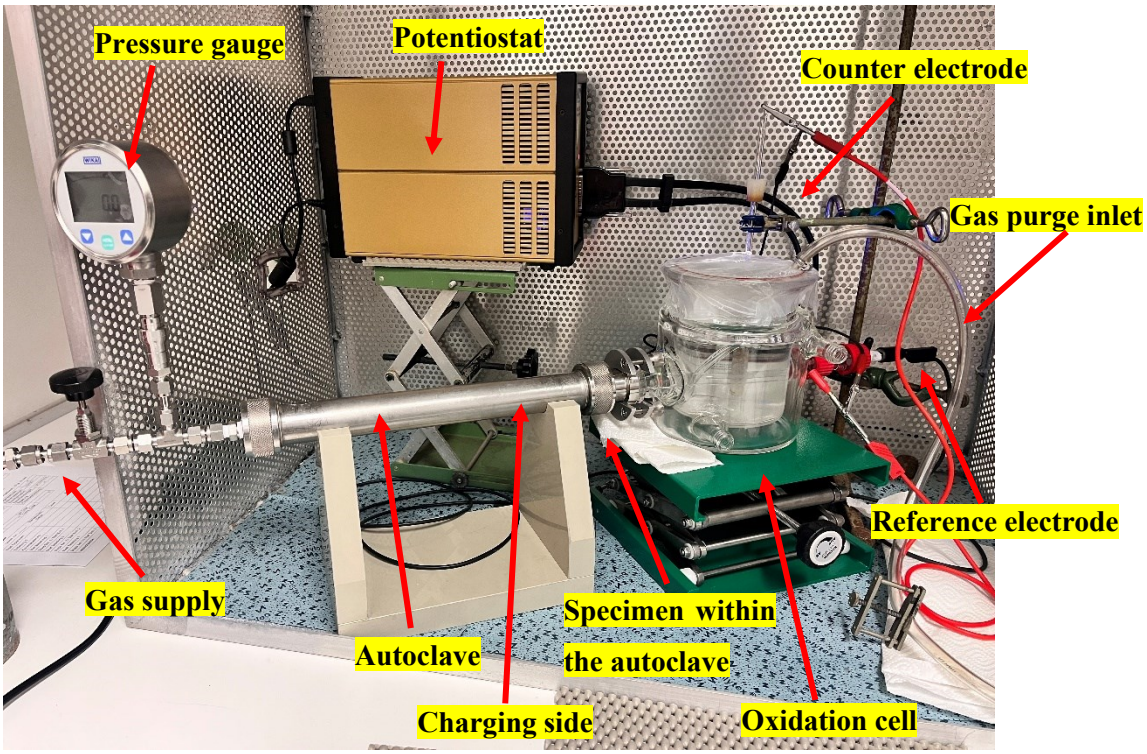

Figure 41. Experimental setup for pressure permeation

Table 12. Charging conditions for pressure permeation

Medium charging side	Dry H_2 gas
Electrolyte oxidation cell	0.1M NaOH
Temperature	25°C
Sample thickness	1 mm
Sample coating	Pd on the oxidation side
Sample area	5.7 cm^2
Counter electrode	Pt
Reference electrode	Ag/AgCl
Gas purging	Ar
Pressure	100 bar

As for the electrochemical permeation, the glass cell on the right side served as an oxidation cell with a NaOH solution as an electrolyte. Furthermore, an Ag/AgCl electrode was used as a reference electrode and platinum as the counter electrode. In this method, the autoclave represented the charging side of the permeation cell. The autoclave was modified for pressure permeation in such a way that a constant gas flow could be supplied from the left side, and the sample was placed within the autoclave and fixed with a screw lid before the transition to the glass cell to ensure tightness and avoid gas release. Additionally, the charging and oxidation sides were connected by means of a clamping device. The specimen acted as a working electrode that was contacted from the outside at the autoclave. Prior to inserting the specimen within the autoclave, it was first prepared by rinsing in acetone in an ultrasonic bath. To verify the tightness of the vessel, the autoclave within the specimen was evacuated ahead of the experiment, and its gas tightness was tested at 25 bar. This revealed only a minimal pressure loss of 0.2 bar, allowing stable conditions to be adopted for the test. After assembling the experiment, the electrolyte was filled into the oxidation compartment, and the solution was gassed with argon for the entire duration of the experiment. Initially, the discharging process of the specimen in the oxidation cell was initiated until a stable current value was established, using a Gamry reference potentiostat 600 for recording. Upon the start of the charging cycle, dry hydrogen gas was introduced into the autoclave at 100 bar, and the pressure was monitored by a manometer. In the experiment, it was expected that the oxidation current would start to increase as soon as diffusion of hydrogen atoms through the membrane occurred, followed by the establishment of a stable oxidation current once a plateau was attained, as in the case of electrochemical permeation.

Chapter 6

Results

6.1 Hydrogen uptake

In this chapter, the results of all hydrogen charging methods are presented graphically. The diagrams contain the hydrogen measured over the charging time. The theoretical saturation curves were generated numerically by curve fits based on the experimental data using the formula described in chapter 3.2.1. For this purpose, the theoretical diffusion coefficient and the surface concentration were determined from the experimentally measured hydrogen contents with the corresponding time. Subsequently, the theoretical data points with these constants were determined using Matlab so that the saturation curve could be constructed. The following table (Tab. 13) provides information on the blank hydrogen of all materials examined.

Table 13. Ground hydrogen content of all examined materials

Material	Hydrogen content [ppm]	Average [ppm]	Standard deviation [ppm]
ARMCO Fe	0.09 0.07 0.05	0.07	0.02
J55	0.05 0.07 0.08	0.07	0.015
L80	0.08 0.08 0.07	0.08	0
P110	0.09 0.11 0.07	0.09	0.02

6.1.1 Immersion testing

Fig. 42 presents the measured hydrogen content of ARMCO iron. No significant increase was detectable compared to the ground hydrogen. In addition, due to the low uptake and fluctuation of data points, curve fitting was not possible because of an insufficient value of R^2 (determination coefficient). Therefore, the constants D (diffusion coefficient) and Cs (surface concentration) could not be calculated. The coefficient of determination R^2 is a statistical measure of how close the data are to the fitted regression line. In general, the higher the R^2, the better the model fits the data. The value of R^2 was in the range above 85% for all other fitted curves.

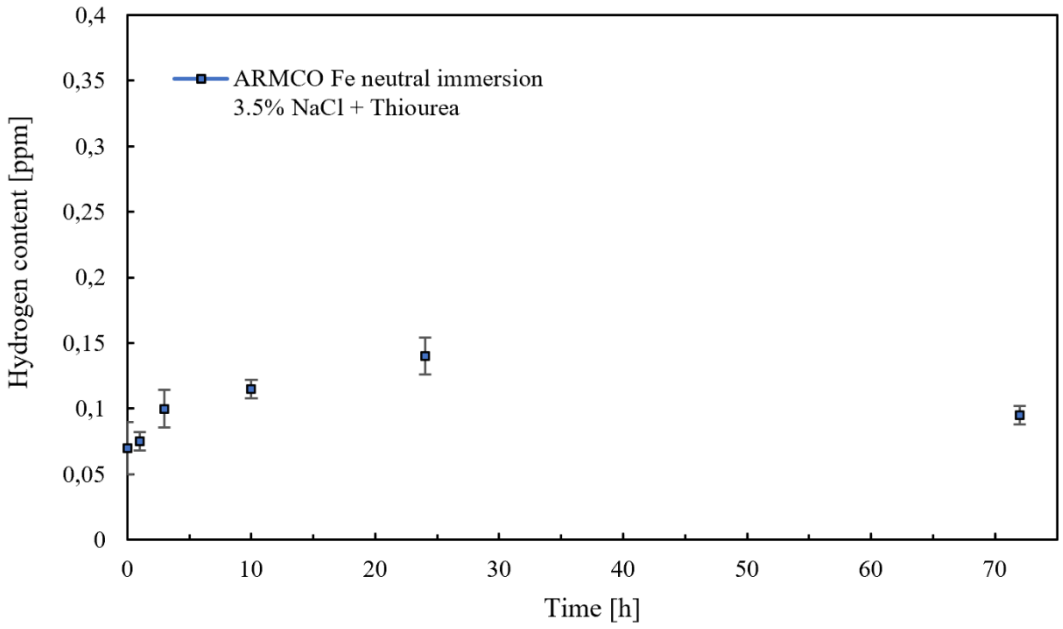

Figure 42. Measured hydrogen content of ARMCO Fe for immersion testing

The hydrogen absorption of L80 during immersion testing was slightly higher than that of ARMCO iron. During charging in a neutral solution, the addition of thiourea as a recombination inhibitor promotes corrosion and consequently increases hydrogen uptake. However, also here, only a low hydrogen absorption was observed (Fig. 43).

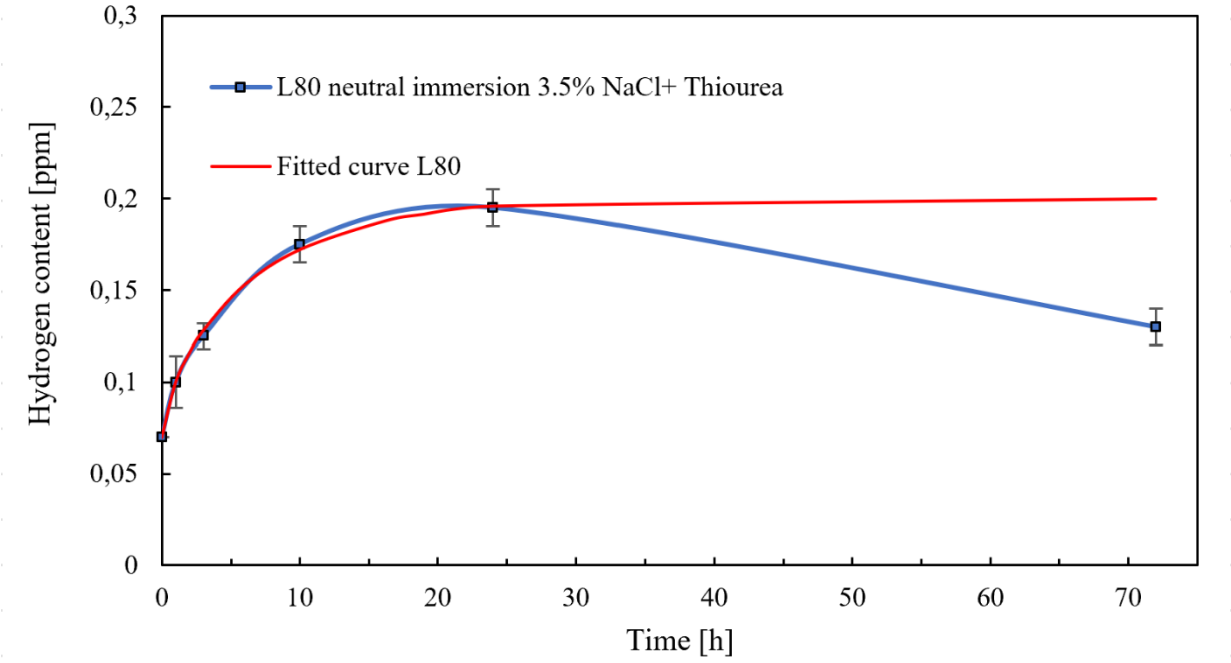

Figure 43.Measured hydrogen content compared with the fitted curve after immersion testing of L80

As can be seen in Fig. 43, the hydrogen concentration in the experimental curve achieves a maximum of around 0.20 ppm after 24 hours and drops again after 72 hours of exposure, probably due to the formation of an oxide layer on the specimen surface. The curve fitting showed the most accurate approximation with the least dispersion of data for a diffusion coefficient of $1.35*10^{-6}$ cm^2/s and a surface concentration of 0.20 ppm. The two constants were determined with the first four experimental data points and based on this, the theoretical progression of the fitted saturation curve was constructed.

Fig. 44 shows that the hydrogen uptake of P110 is similar to that of L80, with slightly higher hydrogen concentrations than ARMCO iron. The experimental saturation was observed at a hydrogen concentration of 0.2ppm followed by a drop after 72 hours due to a layer forming on the specimen surface. During curve fitting, the best diffusion coefficient was found to be $1.28*10^{-6}$ cm^2/s at a constant surface hydrogen concentration of 21 ppm, as shown in the figure. The determined hydrogen diffusion is thus slower compared to the L80 steel grade.

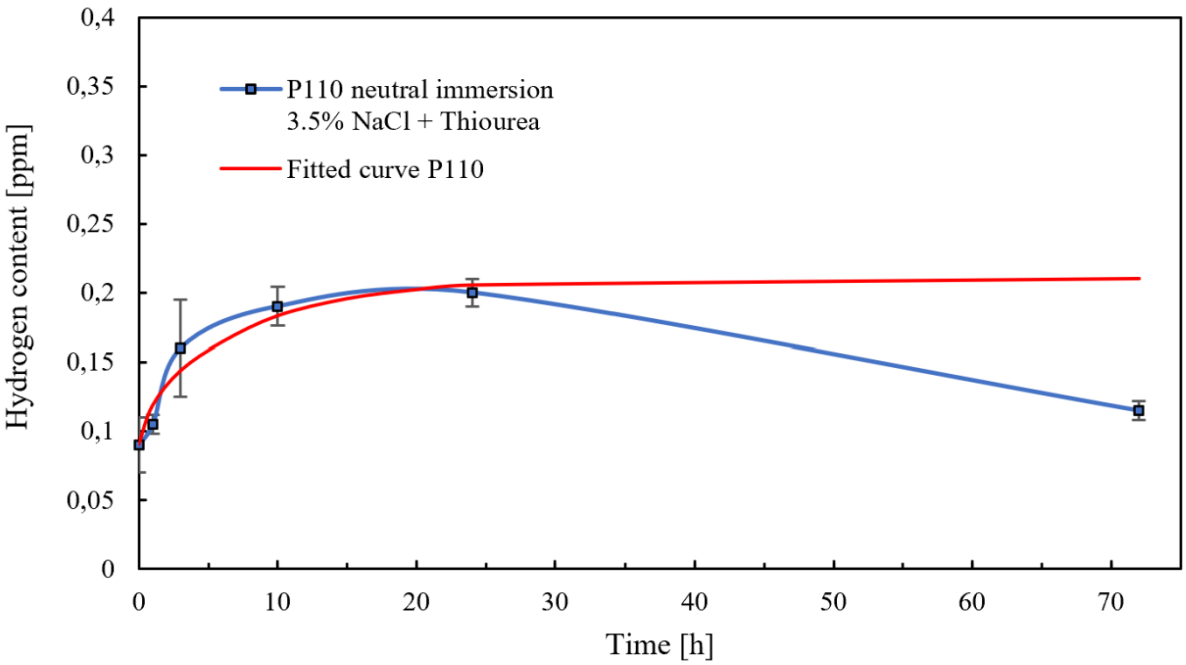

Figure 44. Measured hydrogen content compared with the fitted curve after immersion testing of P110

J55 behaves similarly to P110 and L80 in terms of hydrogen concentration with no significant hydrogen uptake. In Fig. 45, it is indicated that a saturation concentration is reached between 20 and 24 hours. The diffusion coefficient was determined to be $1.4*10^{-6}$ cm^2/s, with a corresponding surface concentration of 0.28 ppm.

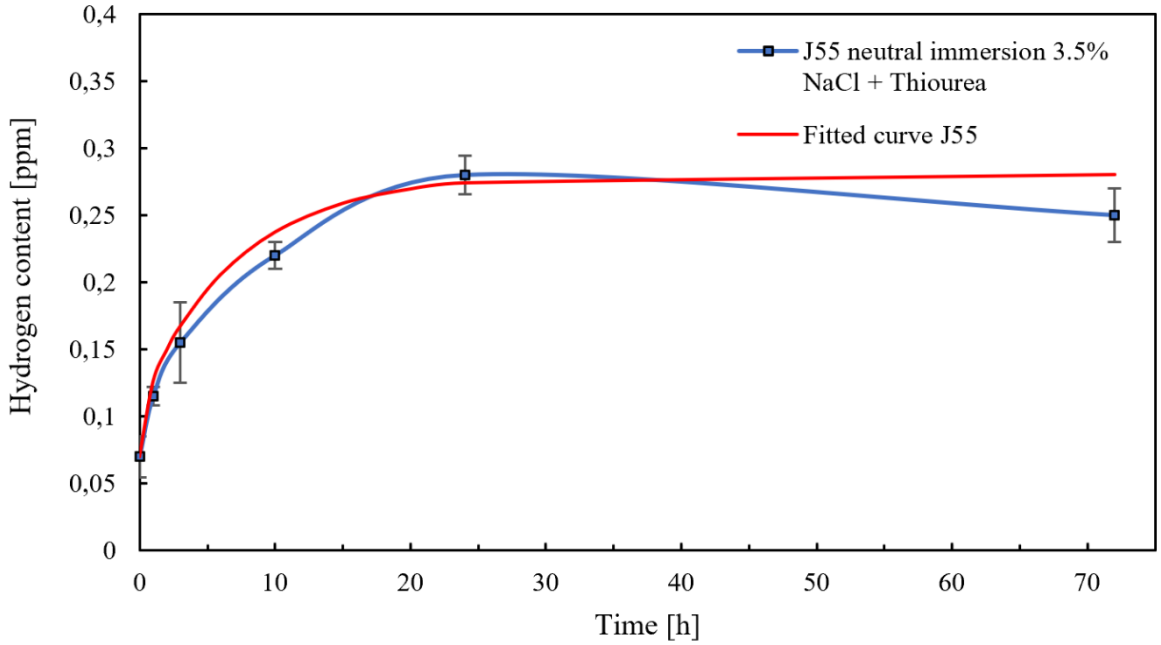

Figure 45. Measured hydrogen content compared with the fitted curve after immersion testing of J55

.

For all four materials, saturation was reached after prolonged exposure to the electrolyte. The hydrogen content decreased again with increasing test duration, probably due to the formation of a corrosion film on the specimen surface. A comparison of all theoretical saturation curves of the carbon steels obtained from the experimental data is illustrated in Fig. 46. Diffusivity is lowest for P110, and J55 exhibits the highest diffusivity of the three carbon steel grades. However, due to the low hydrogen uptake in the mild solution, all materials differ only slightly from each other

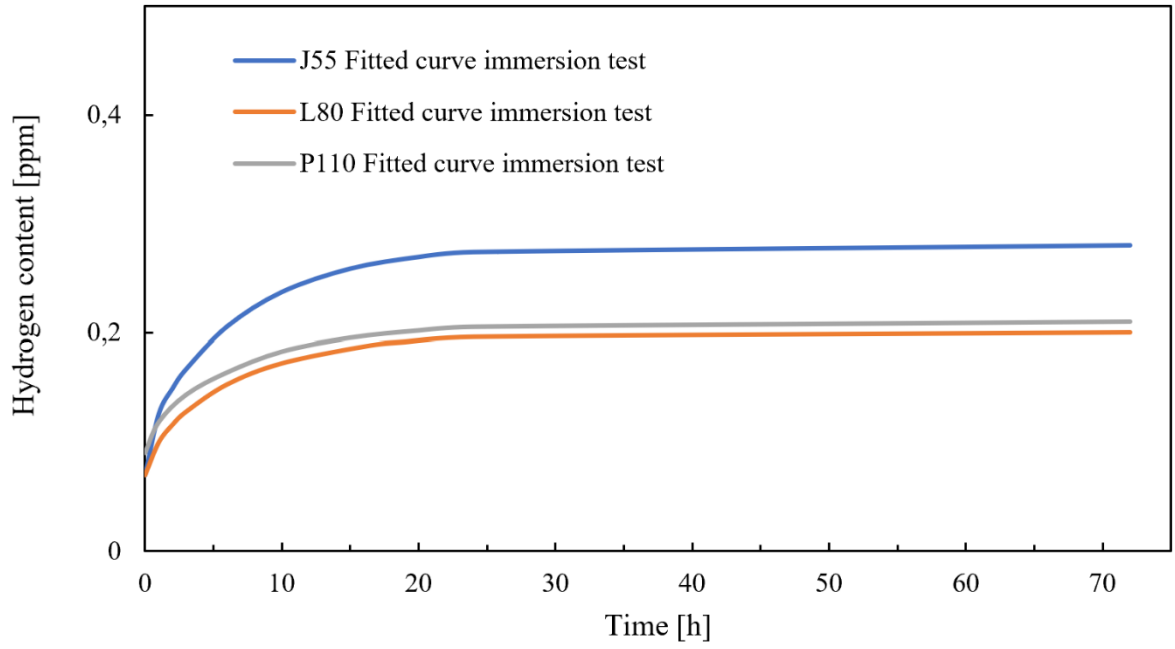

Figure 46. Comparison of the theoretical hydrogen saturation curves of the three carbon steels

6.1.2 Cathodic charging

ARMCO iron shows a higher hydrogen uptake during cathodic charging with a constant current density of 1 mA/cm^2 than for immersion testing, although the amount of absorbed hydrogen also remains relatively low. The hydrogen content in the measurement consistently increases with the charging period, and no apparent saturation was evident from the experimental data. In calculating the constants, the diffusion coefficient could not be determined unambiguously due to the low coefficient of determination (COD). Consequently, no theoretical saturation curve could be constructed. The measured hydrogen concentrations are demonstrated in Fig. 47.

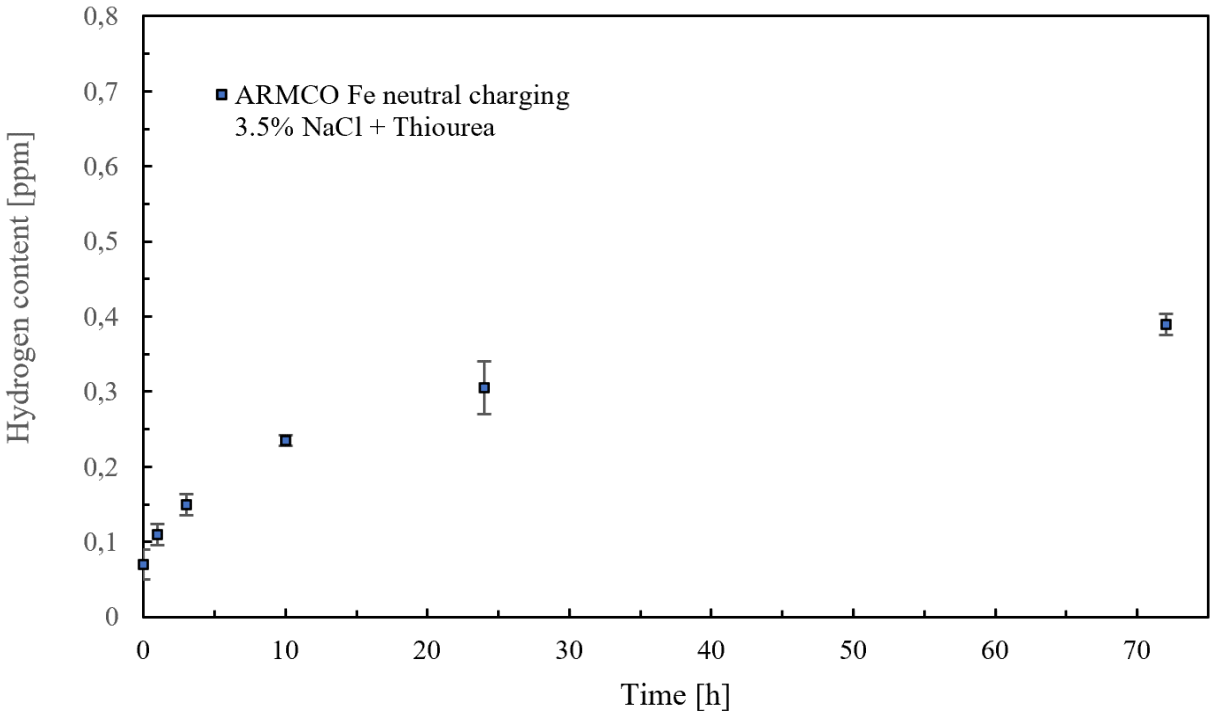

Figure 47. Measured hydrogen content after cathodic charging of ARMCO Fe

During cathodic charging, the absorbed hydrogen concentration is found to be higher for all materials than during the immersion tests. When analyzing the data after the cathodic charging of J55, a higher hydrogen content was detectable than for ARMCO iron. The experimental curve in Fig. 48 does not follow the shape of the immersion experiments, and increasing concentrations versus charging time are observed. When calculating the coefficient and the surface concentration, all experimental data points up to 10 hours were considered since the inclusion of the other data points resulted in unrealistic values, and the scatter of the approximated solution was too high to be able to state a value for the diffusion

coefficient. Therefore, the diffusion coefficient was found to be $1.49*10^{-6}$ cm^2/s with a constant surface concentration of 0.62 ppm.

According to the construction of the theoretically predicted curve, it is evident that saturation of the hydrogen content should arise earlier than 30 hours. The experimental curve deviates quite sharply from the fitted curve above a certain duration of charging and shows a tendency to a linear increase as the period is extended.

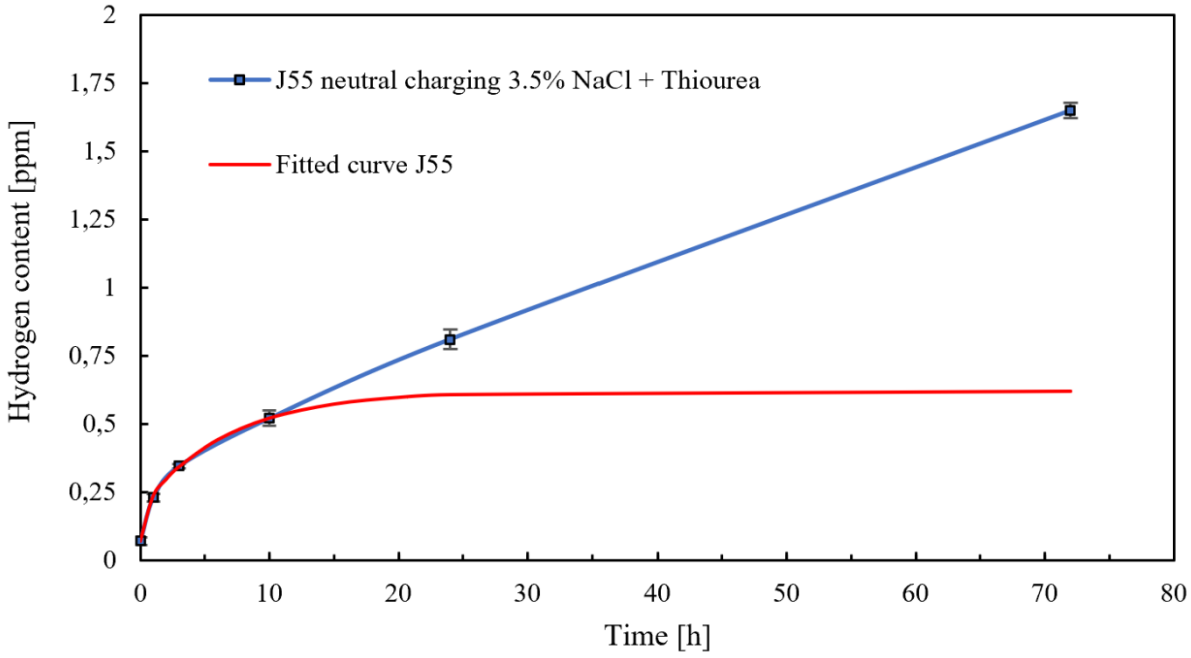

Figure 48. Measured hydrogen content after cathodic charging of J55

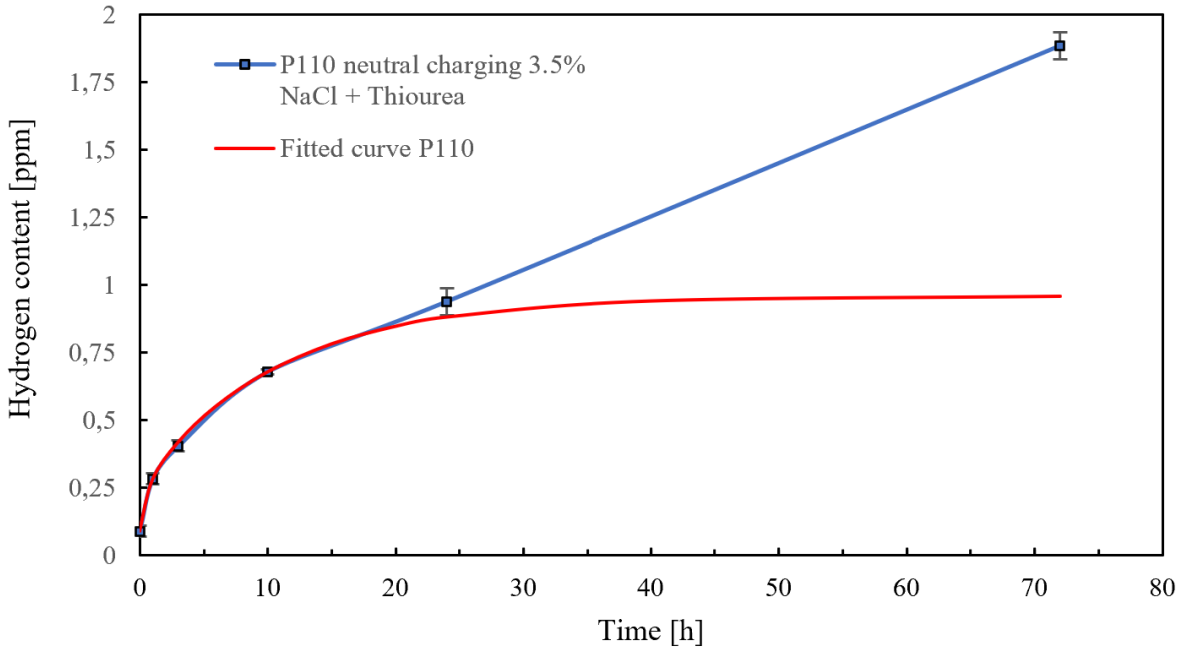

Figure 49. Measured hydrogen content after cathodic charging of P110

In principle, one reason for the sharp increase of the absorbed hydrogen content in the neutral solution could be the incidence of corrosion reactions, which enhance the absorption of hydrogen. The same phenomenon of a continuous increase in the hydrogen concentration over time is observed for all tested materials when cathodically charged in a neutral solution at 1 mA/cm^2. Also, in the case of the P110 steel, no distinct hydrogen saturation was recognizable from the measured concentrations during the test, as depicted in Fig. 49. The amount of hydrogen absorbed by the specimen is similar to that of J55 and higher than that of ARMCO iron. The calculation of the constants to create the theoretical curve is one more based on the consideration of all data points up to 10 hours. For this material, the diffusion coefficient was determined to be 9.36*10^{-7} cm^2/s with a surface concentration of 0.96 ppm.

Hydrogen absorption is similar for the investigated L80 steel as the other carbon steels and significantly higher than for ARMCO iron. The calculated diffusion coefficient, in this case, was 1.14*10^{-6} cm^2/s at a surface concentration of 0.62 ppm (Fig. 50).

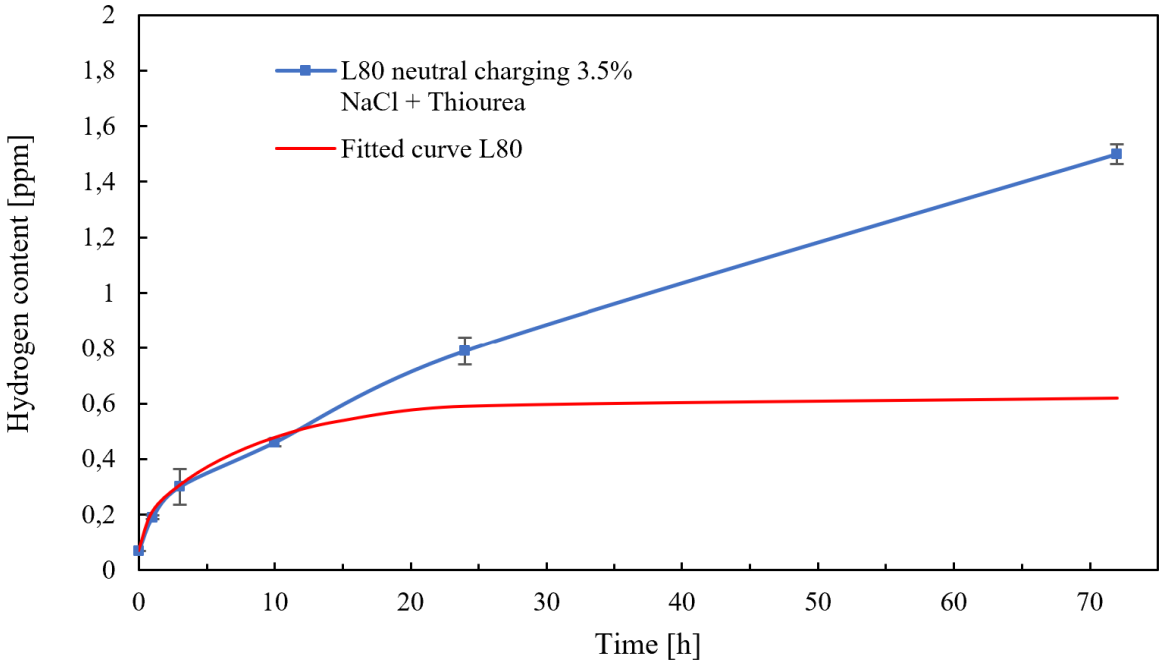

Figure 50. Measured hydrogen content after cathodic charging of L80

All four materials exhibited higher hydrogen uptake compared to the immersion testing, but no experimental saturation could be determined for the charging times performed (Fig. 52). P110 exhibits the highest hydrogen uptake of all materials. The theoretical saturation curves are shown in Fig. 51 for visual comparison. P110 demonstrates the lowest diffusion coefficient, and it can be seen that this material takes the longest time to reach a saturation state compared to L80 and J55. The sequence of increasing diffusion coefficients is the same as for immersion testing, with the lowest diffusivity for P110 and the highest for J55. Again, the differences between the materials are only minor.

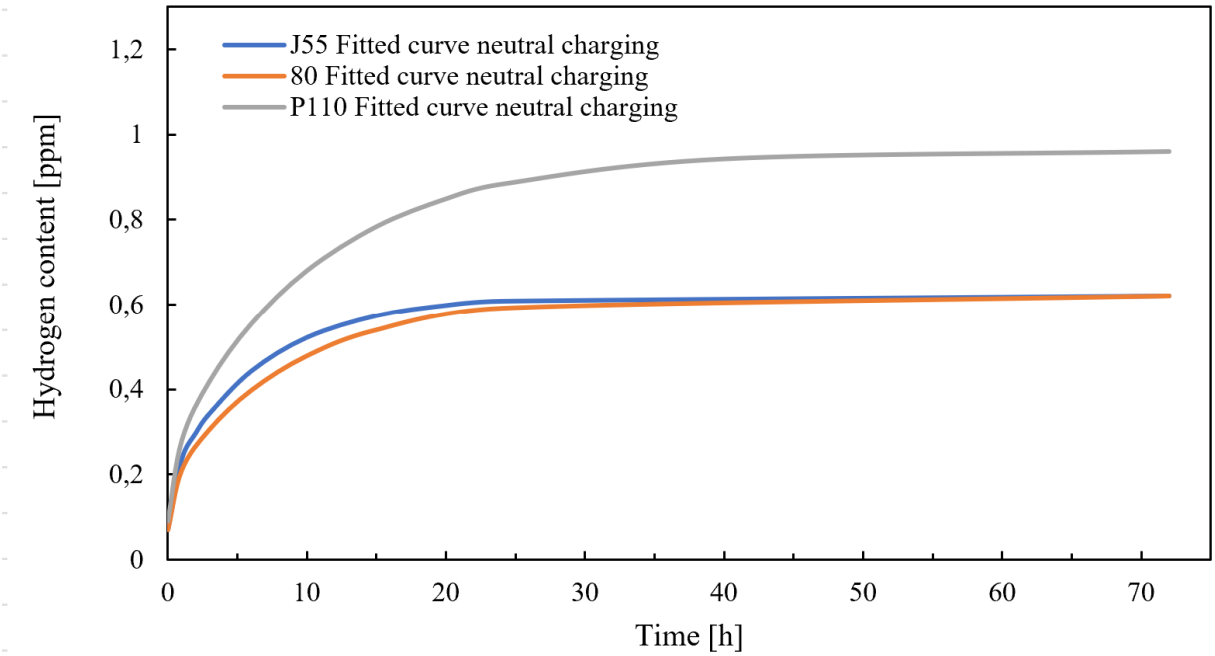

Figure 51. Comparison of the theoretical hydrogen saturation curves of the three carbon steels

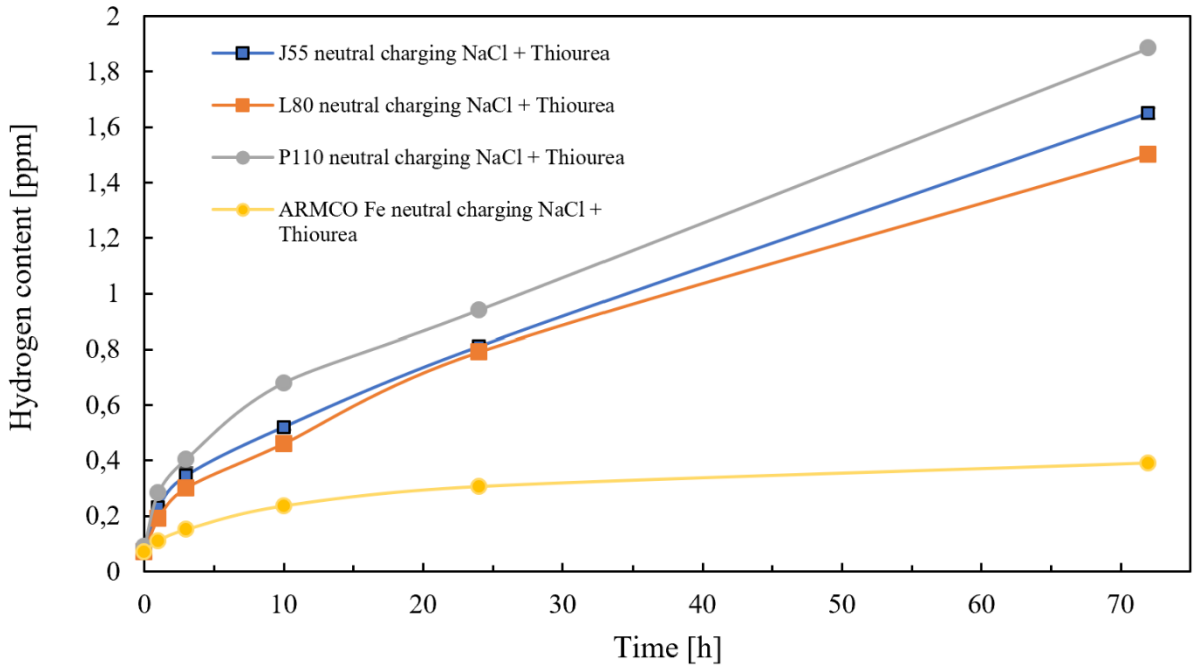

Figure 52. Measured hydrogen content after cathodic charging of all investigated materials

6.1.3 Autoclave tests

The measured content of hydrogen uptake by autoclave tests of dry gaseous hydrogen at 100 bar and room temperature are presented in Fig. 53. When comparing the data series, none of the tested materials shows significant hydrogen uptake. This is also in line with the theory that high pressures greater than 100 bar are required for hydrogen to be absorbed by the metal. The test conditions must correspond to an elevated pressure above 100 bar and increased temperatures to achieve an increased hydrogen uptake in the materials. Furthermore, the addition of an aqueous electrolyte may also lead to improved hydrogen uptake.

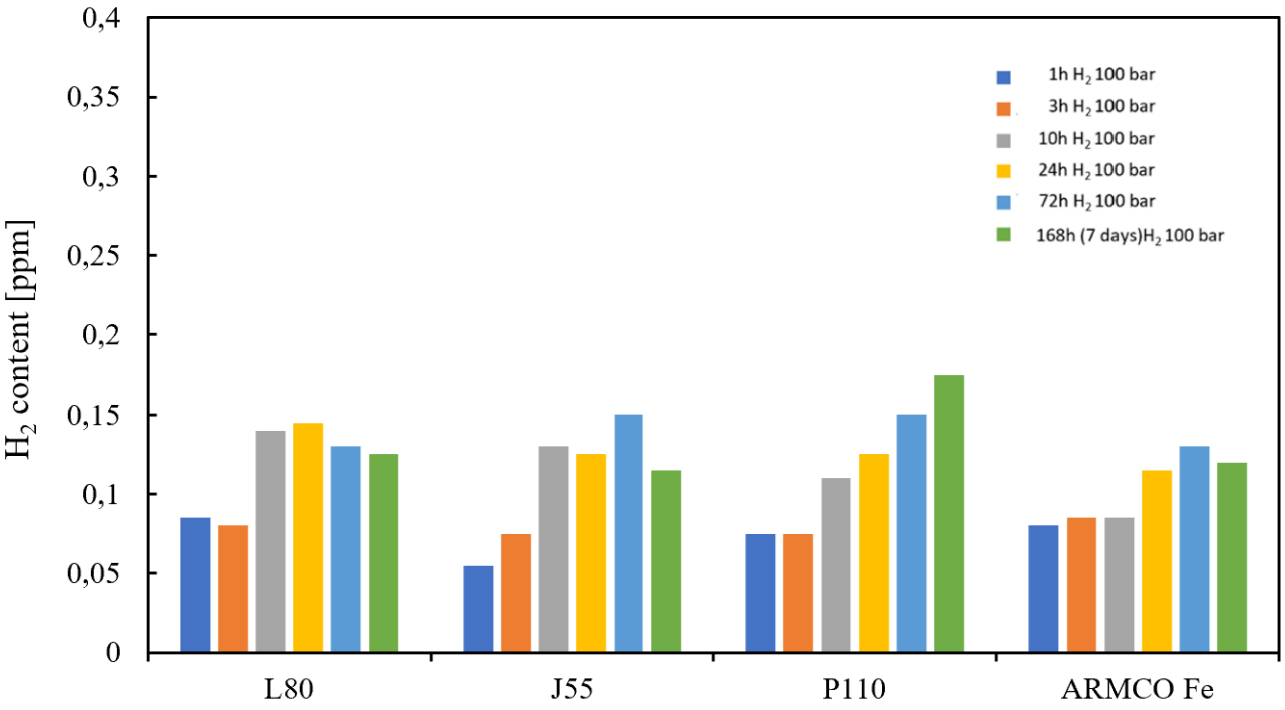

Figure 53. Measured hydrogen content of all materials after various charging times

6.2 Hydrogen permeation

The measured permeation curves were evaluated using the time lag method described in section 3.3.2. The diffusion coefficient was calculated using the following formula:

$$D = \frac{L^2}{6*t_{lag}} \quad \text{(Eq.16)}$$

In addition, a theoretical curve for the charging cycle was constructed according to Fick's law to compare the measured permeation curve:

$$\frac{J(t)}{J_\infty} = \frac{2L}{\sqrt{\pi Dt}} \exp\left(-\frac{L^2}{4Dt}\right) \quad \text{(Eq.17)}$$

If an Equilibrium is established between the charged surface of the membrane and the solution, the hydrogen concentration at the surface can be calculated by the determined diffusion coefficient and the achieved steady-state current density with the following formula:

$$C_0 = \frac{J_\infty * L * M_H}{F * D * \rho_{Fe}} \quad \text{(Eq.18)}$$

Whereby C_0 is the calculated surface hydrogen concentration in ppm, L refers to the thickness of the specimen (m), J_∞ defines the achieved steady-state current density (A/m^2), M_H is the molar mass of hydrogen (g/mol), F describes the Faraday constant (96,485 C/mol) and ρ_{Fe} describes the density of iron ($7.87*10^6$ g/m^3)

6.2.1 Electrochemical permeation

The figures in this section show the normalized charging curves of the electrochemical permeation measurements of all investigated materials. In addition, the corresponding permeation data are tabulated below the figures.

In the permeation measurement of L80, shown in Fig. 54 and Fig. 55, a steady state current value of 6.03 µA and 5.15 µA was obtained for the first and second charging cycles, respectively. The resulting diffusion coefficient was determined to be $1.39*10^{-6}$ cm^2/s for the first charging and $1.44*10^{-6}$ cm^2/s for the second charging. Furthermore, the measured permeation curves in both cycles are close approximated to the theoretical Fick's curve, with the second permeation curve deviating slightly more from the theoretical curve than the first. Comparing the two curves indicates a shorter lag time for the second cycle and higher diffusivity, as shown in Fig. 56.

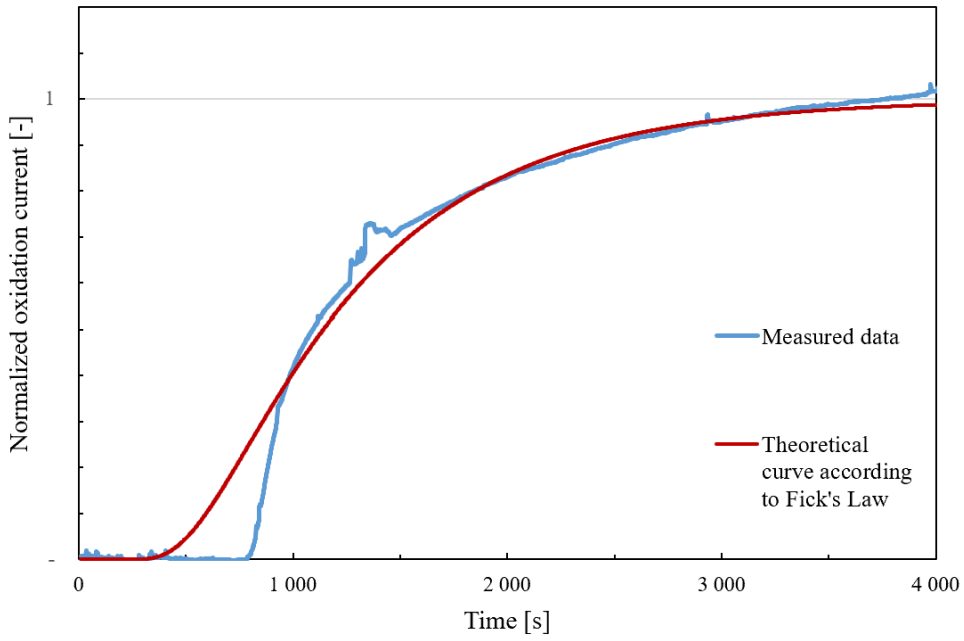

Figure 54. Normalized first permeation transient of L80 and simulation according to Fick's law

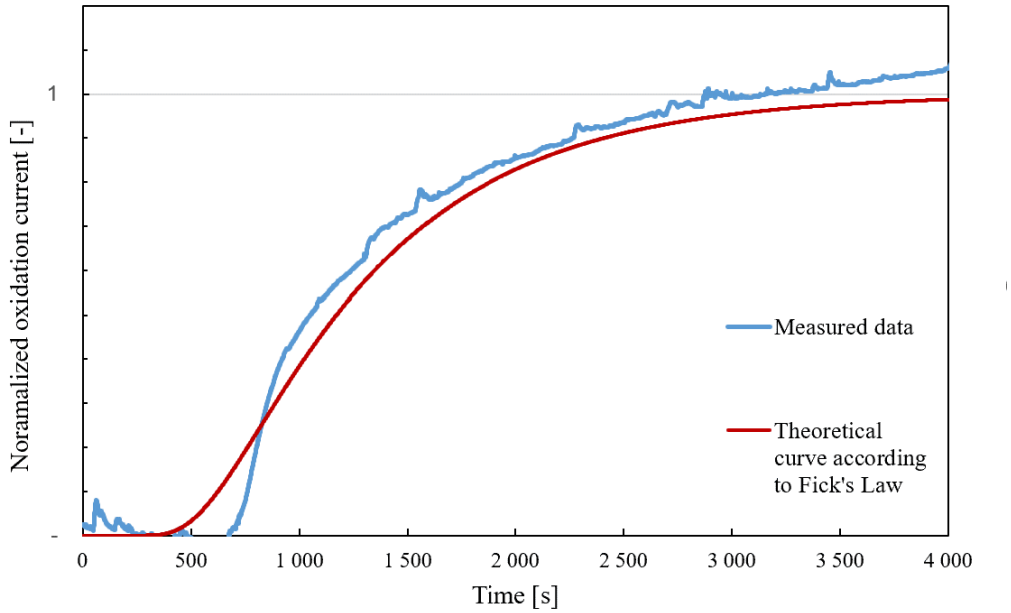

Figure 55. Normalized second permeation transient of L80 and simulation according to Fick's Law

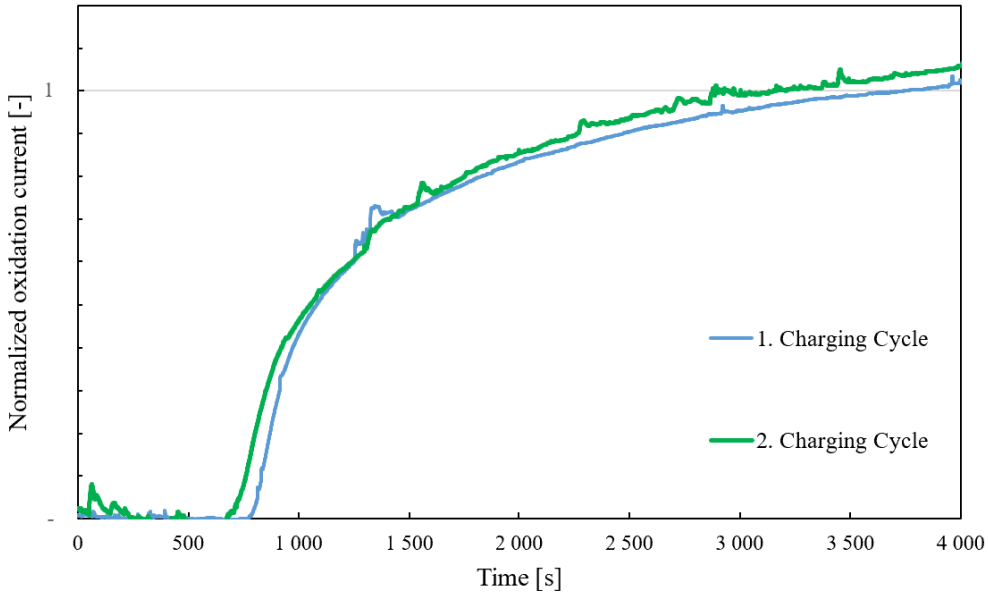

Figure 56. Comparison of both permeation transients of L80

Table 14. Measured data by permeation of L80

	I_∞ [µA]	t_{lag} [s]	D_{eff} [cm²/s]	C_0 [ppm]
1. Charging cycle	6.03	1254	$1.39*10^{-6}$	0.53
2. Charging cycle	5.15	1211	$1.44*10^{-6}$	0.44

For the permeation curves of P110 presented in Fig. 57 to Fig. 59, both transients provide a close approximation to Fick's curve, and the steady state current reached 9.05 µA for the first cycle and 10.04 µA for the second charging cycle. The calculation of the effective diffusion coefficients resulted in $9.15*10^{-7}$ cm^2/s for the first charging and raised to $1.01*10^{-6}$ cm^2/s for the second one. Moreover, a hydrogen surface concentration of 1.24 ppm was determined for both measurements. When comparing the diffusivity, it is found that the diffusion coefficient of P110 is lower than that of L80, and P110 also achieves a higher saturation concentration.

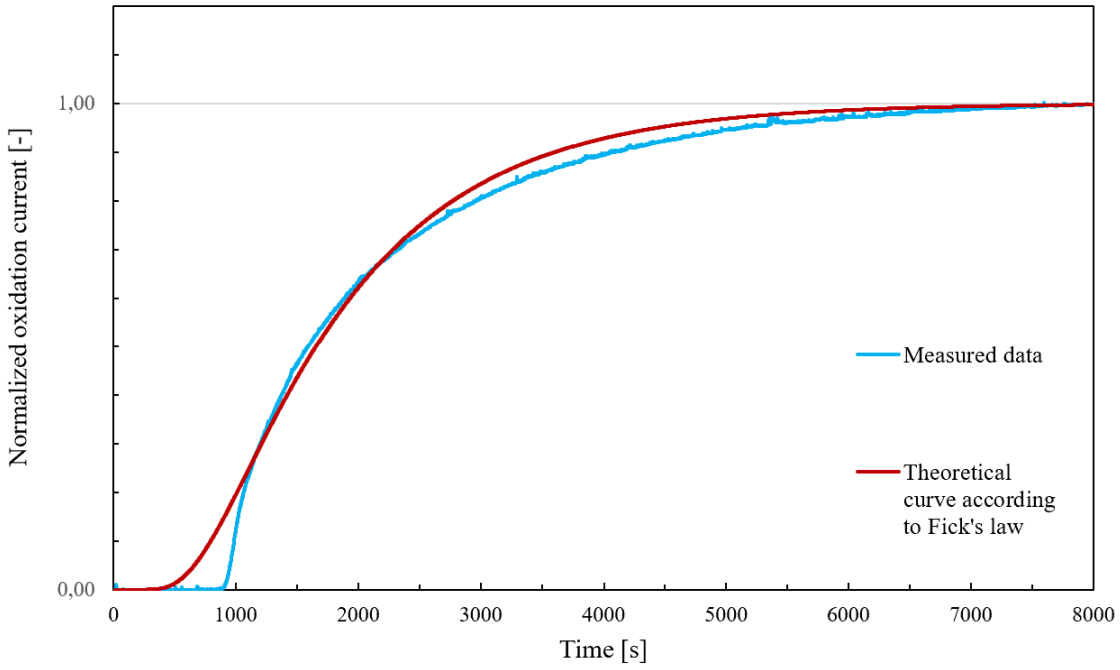

Figure 57. Normalized first permeation transient of P110 and simulation according to Fick's law

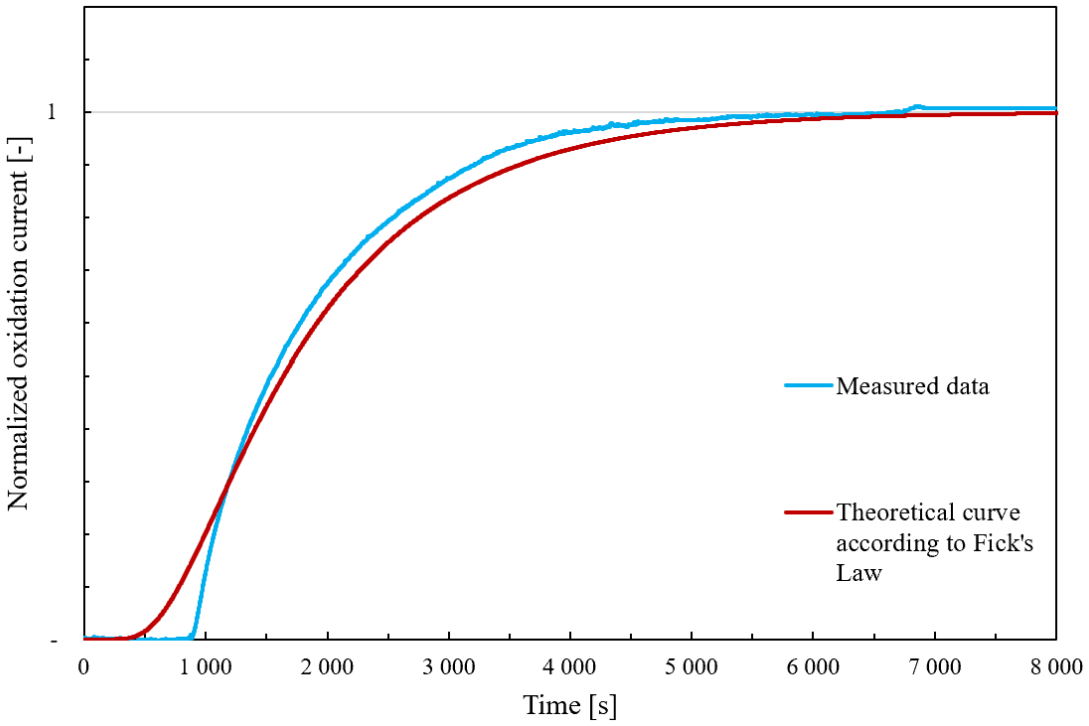

Figure 58. Normalized second permeation transient of P110 and simulation according to Fick's law

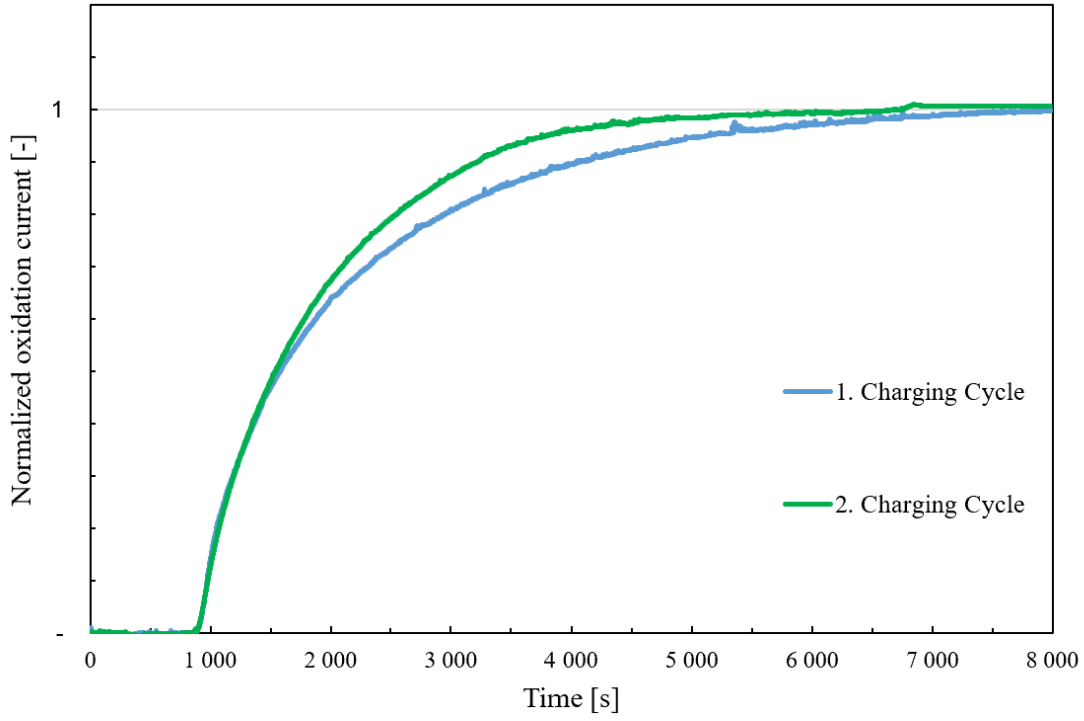

Figure 59. Comparison of both permeation transients of P110

Table 15. Measured data by permeation of P110

	I_∞ [µA]	t_{lag} [s]	D_{eff} [cm^2/s]	C_0 [ppm]
1. Charging cycle	9.05	1970	$9.15*10^{-7}$	1.24
2. Charging cycle	10.04	1784	$1.01*10^{-6}$	1.24

The transients of ARMCO iron are shown in Fig. 60 to Fig. 62. ARMCO iron shows the lowest diffusion coefficient among all materials of $1.19*10^{-5}$ cm^2/s and $1.64*10^{-5}$ cm^2/s for the first and second charging cycles, respectively. The surface concentration level in the material also indicates the lowest value of all the tested materials. Compared with the theoretical curve, it is noticeable that the transients during loading do not follow Fick's law. The calculated surface concentrations theoretically indicate that almost no hydrogen is absorbed by ARMCO iron, and is similar to the value of the blank hydrogen content. As in the previously described permeation evaluations, diffusion is faster in the second charging cycle, and therefore the effective diffusion coefficient is higher than in the first charging cycle.

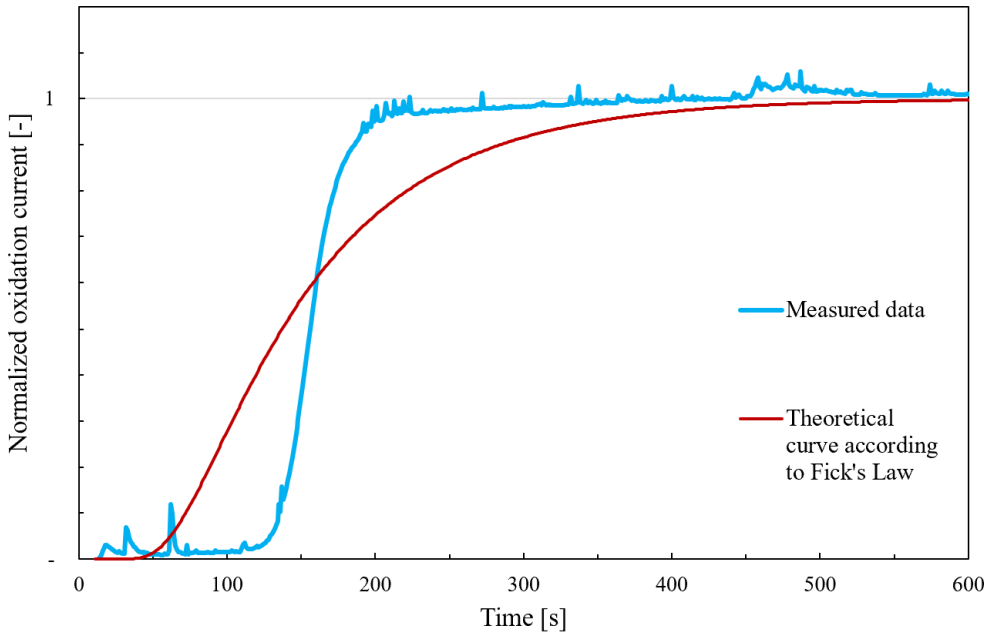

Figure 60. Normalized first permeation transient of ARMCO Fe and simulation according to Fick's law

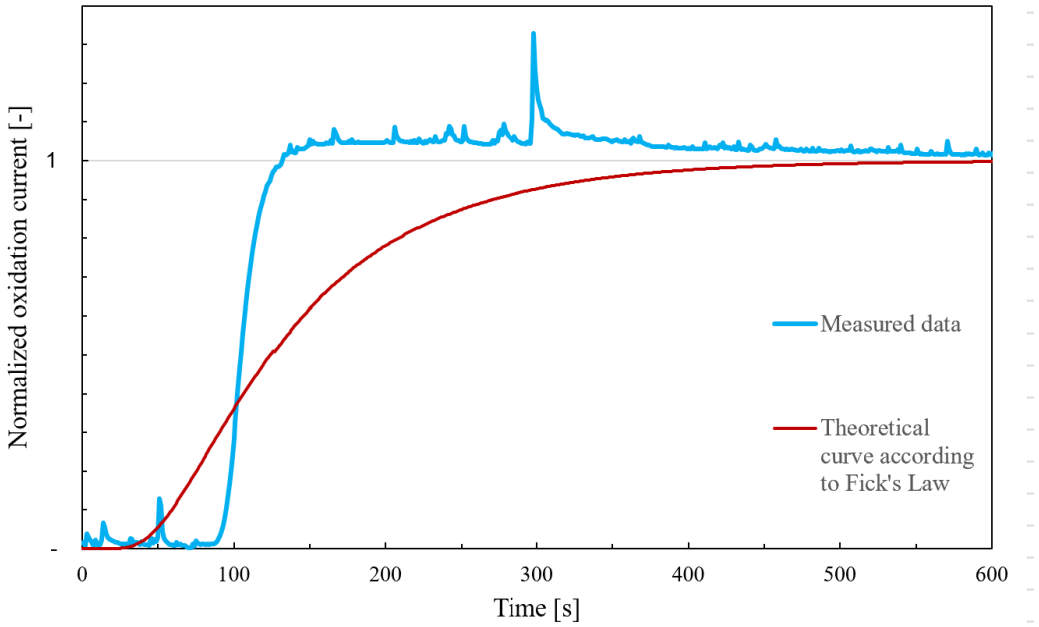

Figure 61. Normalized second permeation transient of ARMCO Fe and simulation according to Fick's law

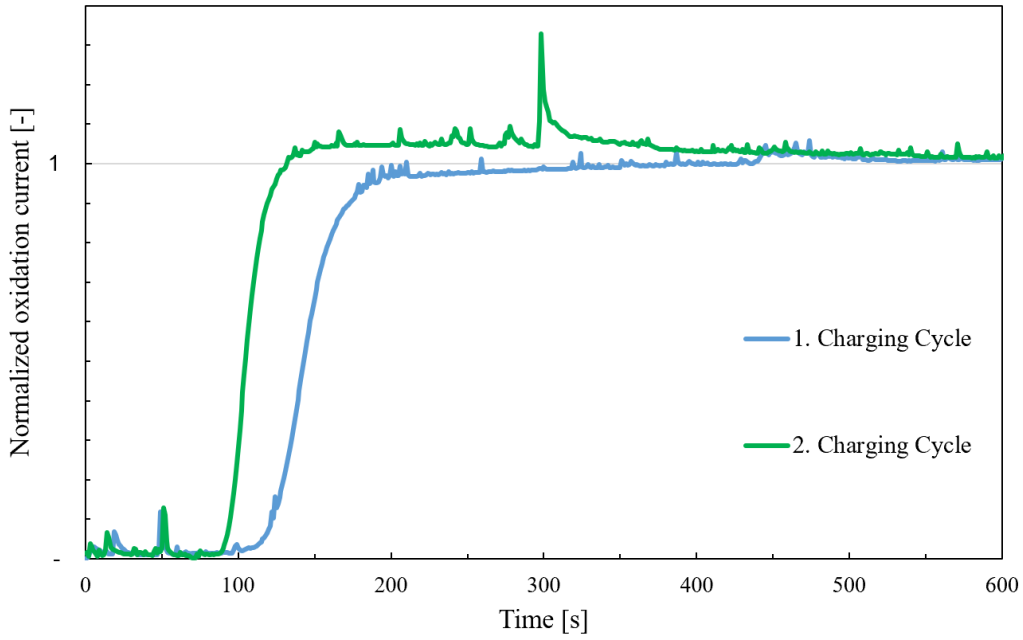

Figure 62. Comparison of both permeation transients of ARMCO Fe

Table 16. Measured data by permeation of ARMCO iron

	I_∞ [µA]	t_{lag} [s]	D_{eff} [cm²/s]	C_0 [ppm]
1. Charging cycle	4.64	149	$1.19*10^{-5}$	0.05
2. Charging cycle	5.36	108	$1.64*10^{-5}$	0.04

During the interpretation of J55, only one loading cycle could be evaluated, and the second one was not reproducible (Fig. 63). The determined diffusion coefficient corresponds to $1.91*10^{-6}$ cm²/s with a surface concentration of 0.44 ppm H.

Table 17. Measured data by permeation of J55

	I_∞ [µA]	t_{lag} [s]	D_{eff} [cm²/s]	C_0 [ppm]
1. Charging cycle	7.5	872	$1.91*10^{-6}$	0.44

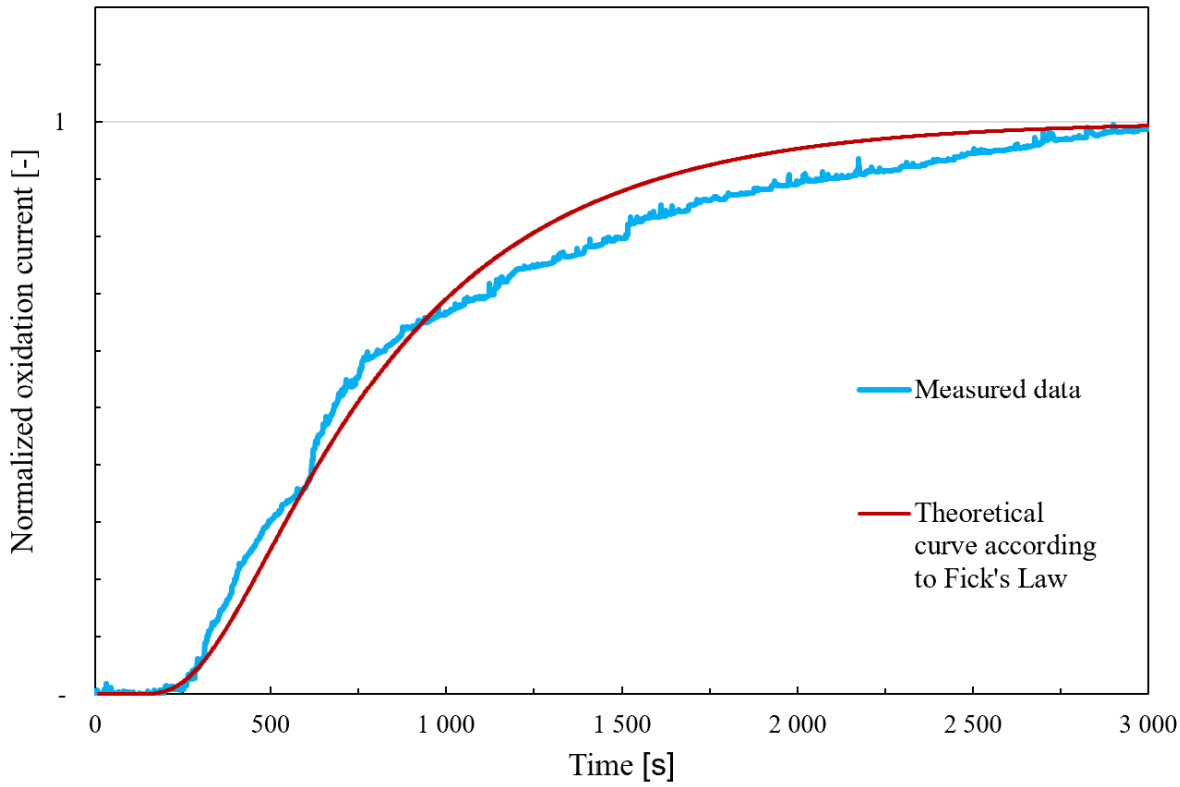

Figure 63. Normalized first permeation transient of J55 and simulation according to Fick's law

The permeation transients of all materials investigated are depicted in Fig.64. The diagram indicates that hydrogen diffuses fastest in ARMCO iron, followed by J55, L80, and P110, with the slowest diffusion. This sequence also corresponds to the observed results from cathodic charging and the immersion tests. In addition, the results are also all in the same order of magnitude as the coefficients found in the other experiments and represent similar values.

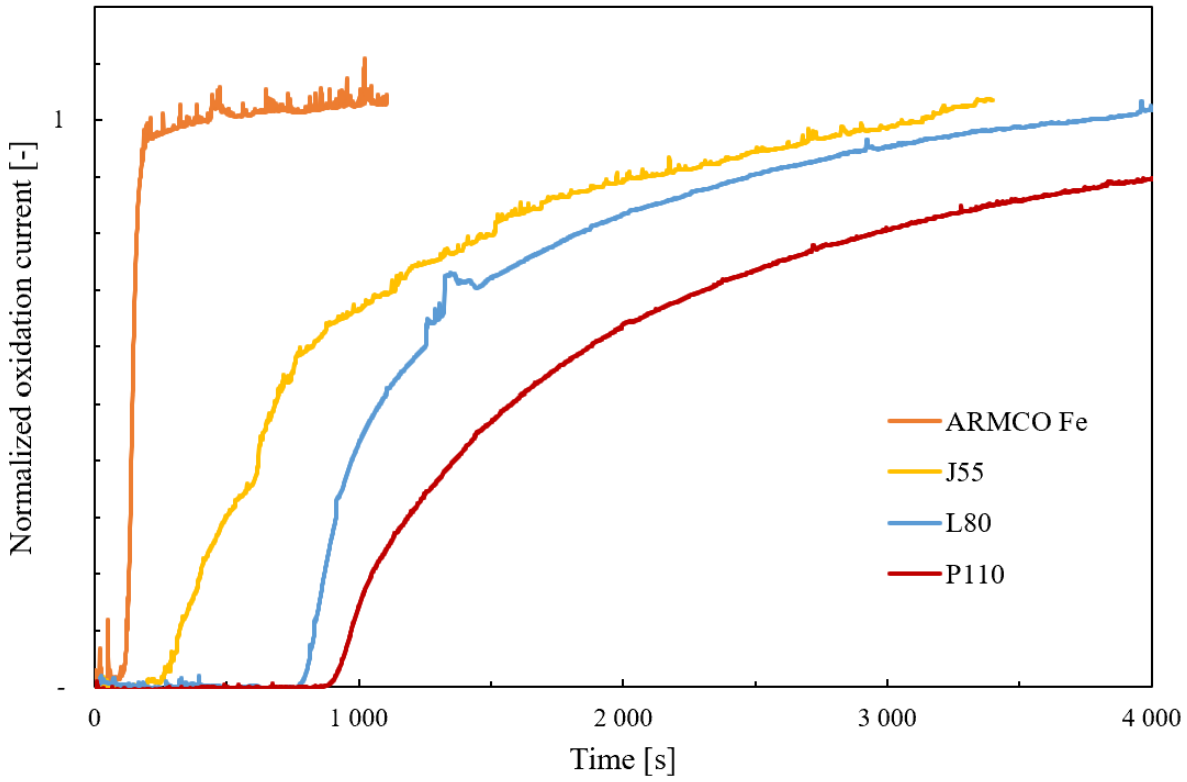

Figure 64. Comparison of the permeation transients obtained for all materials

6.2.2 Permeation at open circuit potential

Throughout the permeation tests at open circuit potential, a build-up of the oxidation current could only be measured for two materials after starting the charging process. No charging cycle was recorded for the samples of L80 and P110, even after one to two days. In the experiments with ARMCO iron and J55, an increase in oxidation current could be measured until a steady state plateau value was achieved. The resulting permeation curves are shown in Fig. 65 and Fig. 66 below. When the transients were evaluated, a longer time lag was observed than for the electrochemical permeation method. The time lag for ARMCO iron was 3384 seconds, meaning it took more than 3000 seconds longer for the initial hydrogen atoms to diffuse through the membrane than required for electrochemical permeation. Therefore, the calculated diffusion coefficient was two orders of magnitude lower and resulted in $5.14*10^{-7}$ cm^2/s. The diffusion coefficient for J55 found is $1.22*10^{-6}$ cm^2/s, which is similar to the diffusion value for electrochemical permeation as the lag time is also delayed here, but not to the same extent as in the case for ARMCO iron. The time lag for J55 corresponds to 1444 seconds, compared to 872 seconds for electrochemical permeation.

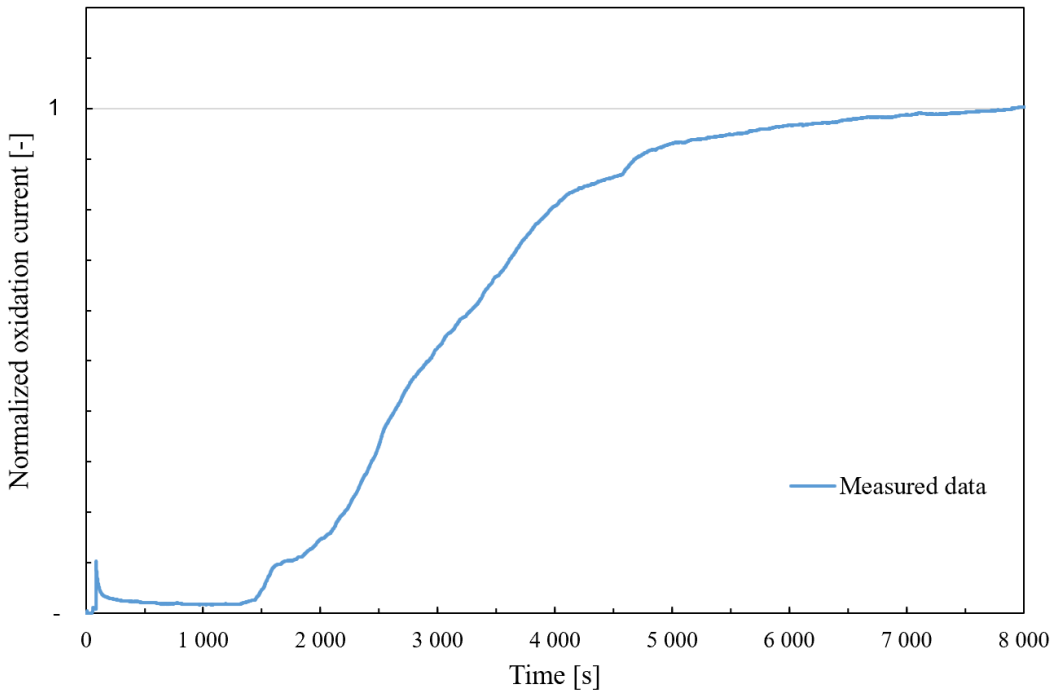

Figure 65. Normalized permeation transient of ARMCO iron

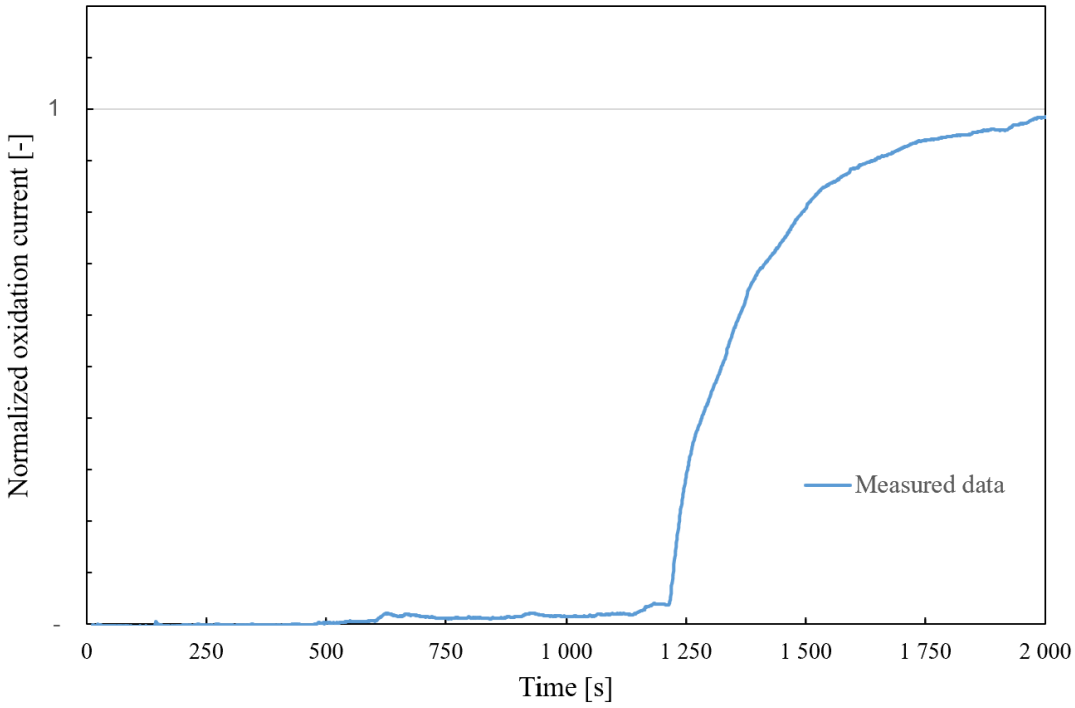

Figure 66. Normalized permeation transient of J55

6.2.3 Pressure permeation

The pressure permeation did not result in a recorded charging cycle after initiating the gas supply. Furthermore, the pressure could not be maintained during the experiment. Suggestions for improving this method will be explained in more detail in a subsequent section.

Chapter 7

Discussion

Throughout all experiments conducted, ARMCO iron exhibits the fastest diffusion of hydrogen compared to the other investigated materials. The examined carbon steel grades behave similarly to each other in terms of hydrogen absorption, with the highest amount of hydrogen absorbed found for P110 in the charging tests. Since ARMCO iron theoretically contains the least amount of traps in the microstructure, the assumption of the fastest diffusion behavior is also consistent with the literature.

Basically, room temperature conditions were selected for all experiments with an applied current density of 1 mA/cm^2, and a neutral 3.5% NaCl solution with thiourea added was used as an electrolyte. Thiourea was added to inhibit the recombination reaction and promote hydrogen uptake in the metal. The hydrogen uptake during the immersion test was rather low for all specimens. By observing the measured hydrogen concentrations, a saturation hydrogen concentration could be recognized for each material, although the hydrogen content decreased again after reaching the peak. One explanation for this could be the formation of an oxide layer on the metal surface, hindering further hydrogen uptake. During the cathodic hydrogen charging tests, it was noted that no saturation of the hydrogen concentration was achieved during charging. In the following curve fitting procedure, all data points up to 10 hours were considered for the numerical analysis for both hydrogen charging methods since these data points showed the lowest dispersion of the convergence. The saturation curves were then generated on the basis of the numerically determined diffusion coefficient and surface concentration. The constructed theoretical curves showed close approximations to the experimental data for the immersion tests except for ARMCO iron. ARMCO iron did not allow curve generation due to the low absorbed hydrogen contents and the large scatter of the data. The same phenomenon was observed for ARMCO iron in the cathodic charging tests. However, theoretical saturation curves could be generated in the cathodic charging experiments of all other materials. In the saturation curves for cathodic charging, a significant deviation from the experimental curve was observed after a specific charging duration of

about 10 hours. From this point on, the hydrogen concentration seems to increase sharply further as a function of the charging period and no longer achieves a saturation state of the hydrogen content. The steadily rising hydrogen content in the mild solution could result from corrosion reactions occurring in the material. Therefore, additional tests were carried out with ARMCO iron at increased current density of 10 mA/cm^2 to suppress these reactions and to be able to obtain saturation.

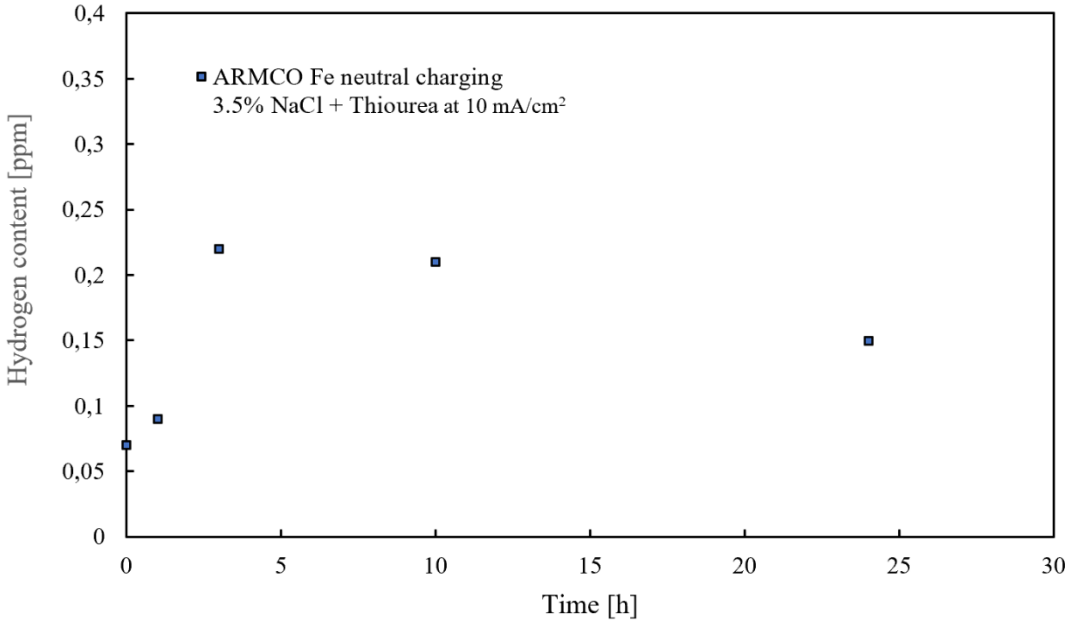

Figure 67. Cathodic hydrogen charging of ARMCO iron at 10 mA/cm^2

The results of these additional measurements are shown in Fig. 67 and show that saturation may be observed at an increased current density.

The diffusion coefficients determined in the cathodic charging experiments and immersion tests differed only slightly and are comparable to the values found in the literature.

The autoclave tests performed at 100 bar at room temperature under dry conditions with gaseous hydrogen did not indicate significant hydrogen uptake. Therefore, further tests should be performed at elevated pressures and temperatures.

The diffusion coefficient was also determined by permeation measurements under different conditions to identify differences in the resulting value of the coefficient. In the electrochemical permeation measurements, the second charging cycle indicated faster diffusion of hydrogen and, thus, a higher diffusion coefficient. The deviation of the transient from the theoretical Fick's curve varied among the materials, which may be explained by the given surface conditions of the specimen and the traps present in the microstructure. The diffusion coefficients evaluated from the permeation curves were similar to those determined in the cathodic charging and immersion tests. In addition, the permeation experiments at open circuit potential showed only one evaluable charging cycle for the examined specimens of

ARMCO Iron and J55 steel. The time lag for this method of ARMCO iron was more than 200 times longer than for the electrochemical permeation, leading to a diffusion coefficient two orders of magnitude lower. For J55, the time lag was almost twice as long as for electrochemical permeation, hence the diffusion coefficient did not change significantly.

The determined diffusion coefficients and surface concentrations in electrochemical permeation were used to plot theoretical saturation curves. The constructed curves are implemented in the cathodic hydrogen charging diagrams and presented in the following figures to show the deviation compared to the fitted curves (Fig. 68 to Fig. 70).

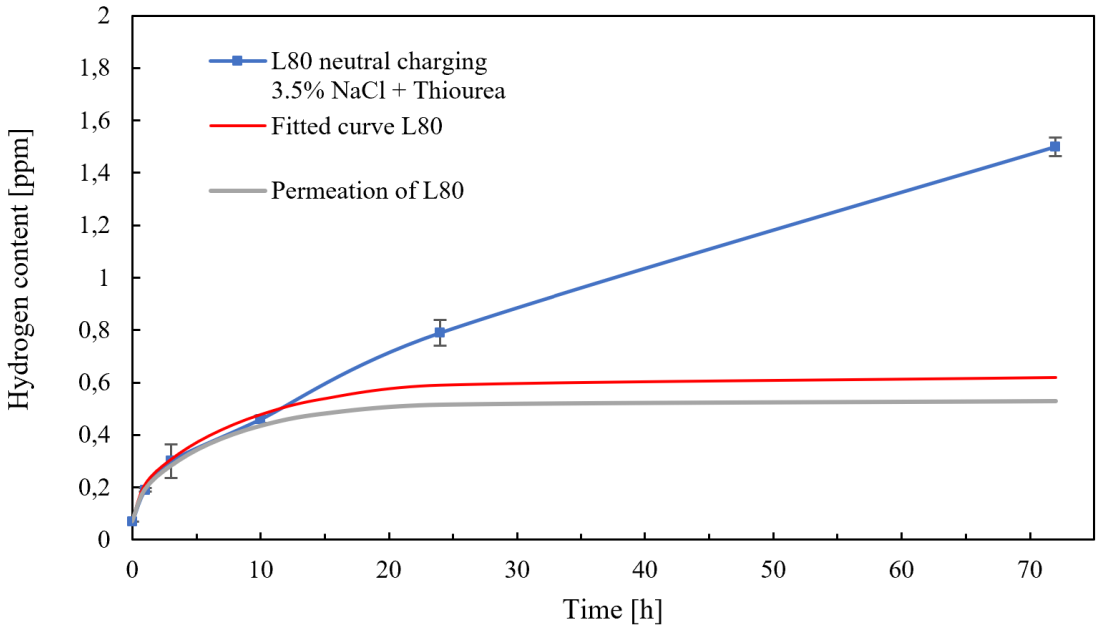

Figure 68. Comparison of hydrogen saturation curves of L80

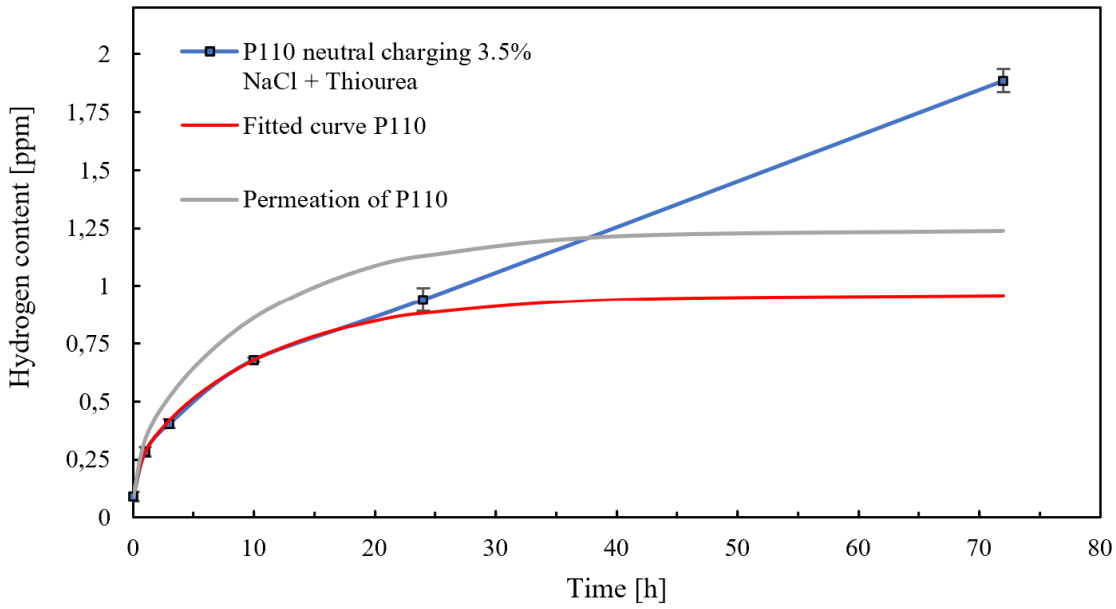

Figure 69. Comparison of hydrogen saturation curves of P110

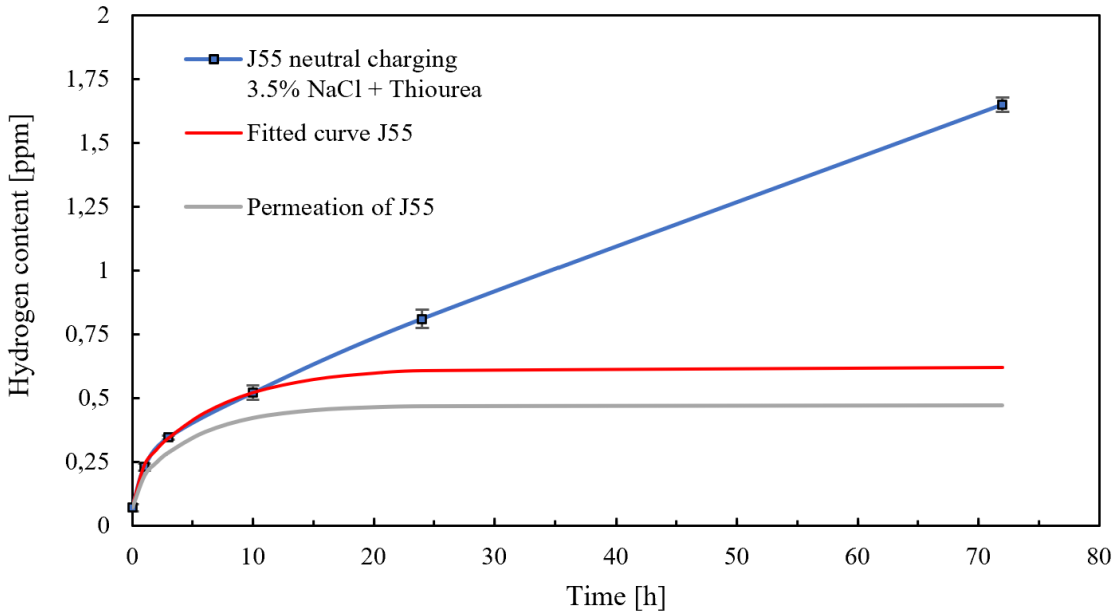

Figure 70. Comparison of hydrogen saturation curves of J55

As mentioned earlier, the pressure permeation method did not yield any results. Furthermore, pressure losses became noticeable during the experiment. Here it is advisable to reconsider the experimental setup and perhaps use a method described in the theoretical part of this thesis according to the application proposed by the Oak Ridge National Laboratory.

The same sequence of increasing diffusion coefficients was observed during all experiments performed. Hydrogen diffuses most rapidly in ARMCO iron due to the minor amount of traps in the microstructure. The order continues with J55, L80, and P110 having the lowest diffusion coefficient, as shown in Fig. 71.

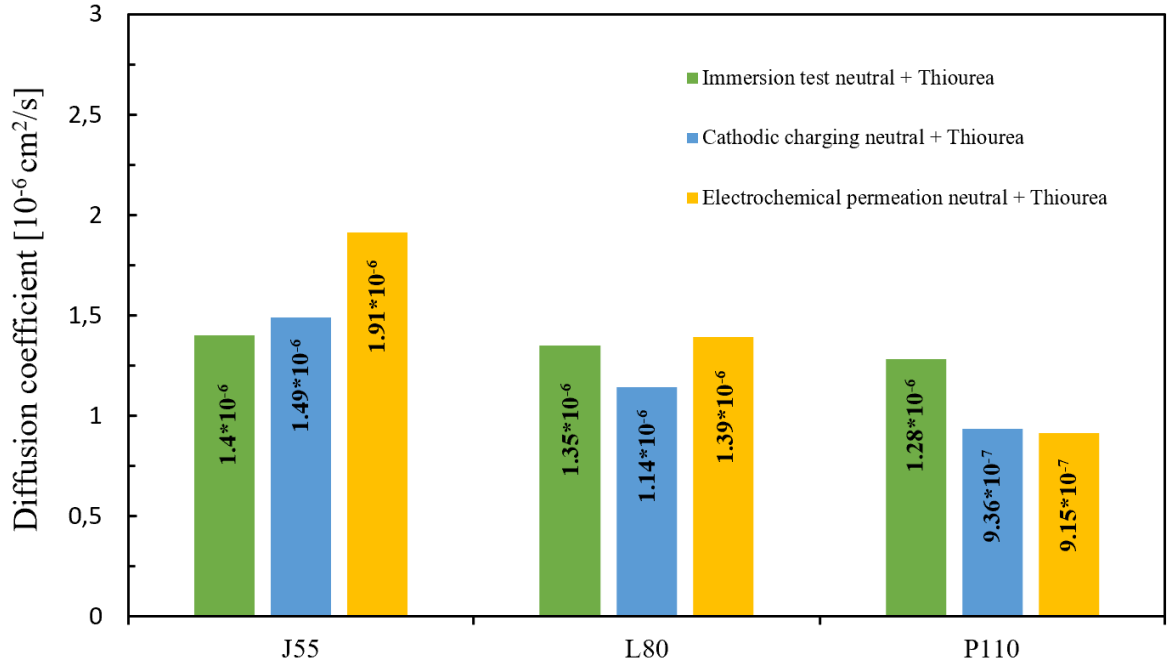

Figure 71. Diffusion coefficients obtained by various experiments

A correlation was also found that a decreasing diffusion coefficient tends to be associated with increasing strength of the material (Fig. 72). This can be explained by the fact that as the strength increases, the grain size usually decreases, and thus, the microstructure theoretically contains more traps that can capture hydrogen, resulting in a longer residence time of the atoms and therefore lowering the diffusion rate.

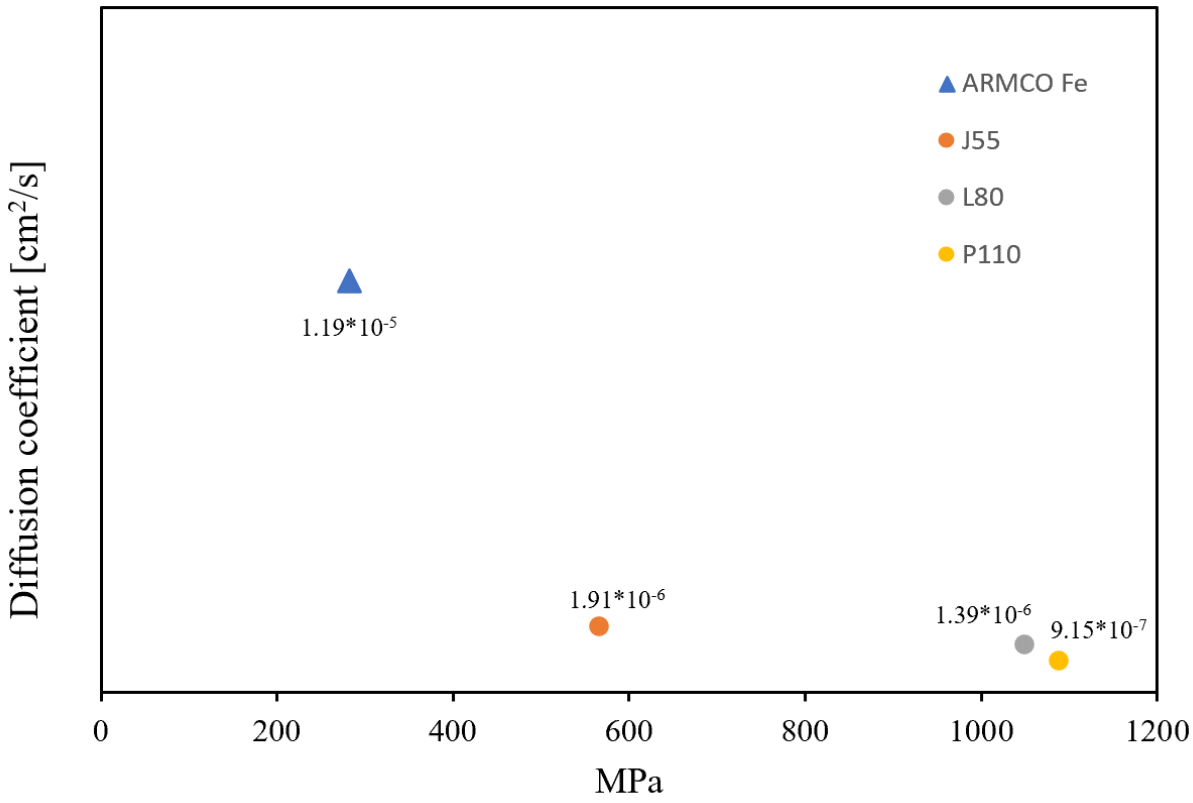

Figure 72. Diffusion coefficient vs. UTS of the investigated materials

Chapter 8

Conclusion

In order to improve the prevention of hydrogen-induced material damage and to create safe operating conditions in the oil and gas industry, as well as to ensure smooth transport and storage of hydrogen in the future, it is essential to understand the diffusion behavior of hydrogen in metals. The aim of this work was to determine diffusion coefficients by different hydrogen charging methods and permeation. Furthermore, the amount of hydrogen absorbed by different steel grades was to be analyzed. The investigated materials were three carbon steel grades J55, L80, and P110, commonly used in the petroleum business, and ARMCO iron was chosen as the reference material. The results of the experiments indicate just a minor hydrogen uptake in the neutral charging solution for all materials, with the hydrogen content being the lowest for ARMCO iron. In order to determine significant hydrogen uptake in future experiments, a more aggressive corrosive environment, such as hydrogen sulfide, should be selected for test conditions. Furthermore, it is advisable to perform tests at an increased current density of 10 mA/cm^2 to counteract layer formation on the sample surface and to measure higher hydrogen contents. The investigation of hydrogen absorption by means of autoclave tests under dry conditions presented just a rather low amount of absorbed hydrogen in the material. If these tests are to be continued, it is advisable to extend the test conditions to elevated pressures and temperatures. In addition, it is recommended to add aqueous electrolytes and gases such as H_2S or CO_2 into the autoclaves to enhance the effect of hydrogen uptake by steel. Since the pressure permeation method did not yield useful results, the experimental setup should be modified again for further tests at high pressures. In terms of permeation at open circuit potential, a permeation curve could only be obtained for two materials, J55 and ARMCO iron. In the case of ARMCO iron, the results of the evaluation indicate that the experimental method affects the resulting diffusion coefficient since it was found to be two orders of magnitude slower than the one determined during electrochemical permeation. However, this effect was not observed in the evaluation of J55 since the diffusion coefficient did not change

significantly with this technique. The values determined in the electrochemical permeation for the diffusion coefficient and the constant surface concentration allowed the individual techniques performed to be compared in terms of the diffusion coefficient. Besides that, the sequence of increasing diffusion coefficients with respect to the investigated material was the same in all experiments. This shows that hydrogen diffuses fastest in ARMCO iron, followed by J55 and L80. The slowest diffusivity was observed in P110. In general, the measured diffusivities of the carbon steel grades are comparable to literature values and are one to two orders of magnitude lower than the coefficient of ARMCO iron. Moreover, the correlation was also noticed that it seems the diffusion coefficient decreases as the strength of the steel increases.

References

[1] O. Barrera, E. Tarleton, H.W. Tang, A. Cocks, Modelling the coupling between hydrogen diffusion and the mechanical behaviour of metals, Computational Materials Science 122 (2016) 219–228

[2] A. M. El-Sherik, Trends in Oil and Gas Corrosion Research and Technologies: Production and Transmission, Woodhead Publishing Series in Energy, United Kingdom, 2017

[3] T.E. Perez, Corrosion in the Oil and Gas Industry: An Increasing Challenge for Materials, JOM 65 (2013) 1033–1042

[4] R.N. Tuttle, Corrosion in Oil and Gas Production, Journal of Petroleum Technology (1987)

[5] J. Aslam, R. Aslam, S. Zehra, M. Rizvi, 8 - Corrosion inhibitors for sweet (CO2 corrosion) and sour (H2S corrosion) oilfield environments, in: C.M. Hussain, C. Verma, J. Aslam (Eds.), Environmentally Sustainable Corrosion Inhibitors, Elsevier, 2022

[6] Nikolaus Schmidbauer, Bewertung von Korrosionsrisiken als Grundlage für die technische Überwachung einer Gasaufbereitungsanlage, Diplomarbeit, 2016

[7] L.T. Popoola, A.S. Grema, G.K. Latinwo, B. Gutti, A.S. Balogun, Corrosion problems during oil and gas production and its mitigation, International Journal of Industrial Chemistry 4 (2013) 35

[8] G. Mori, Vorlesungsskriptum Korrosionskunde, Montanuniversität Leoben,2012, Vorlesungsskriptum Korrosionskunde

[9] Y. Wang, J. Li, C. Qu, W. Li, M. Baba Pali, H. Zheng, Research Progress on Corrosion of Oil and Gas Field Gathering Pipeline in H2S-CO2-Cl−System, IOP Conference Series: Earth and Environmental Science 555 (2020) 12046

[10] E.S. Skilbred, S. Palencsár, A. Dugstad, R. Johnsen, Hydrogen uptake during active CO2-H2S corrosion of carbon steel wires in simulated annulus fluid, Corrosion Science 199 (2022) 110172

[11] Yuli Panca Asmara, The Roles of H2S Gas in Behavior of Carbon Steel Corrosion in Oil and Gas Environment: A Review: Faculty of Mechanical Engineering, University Malaysia Pahang, Jurnal Teknik Mesin (JTM) (2018)

[12] H.G. Elsbeth Wendler-Kalsch, Korrosionsschadenkunde, Springer-Verlag Berlin Heidelberg GmbH, Nachdruck 2012

[13] Qing Tang, and De-en Jiang, Mechanism of Hydrogen Evolution Reaction on 1T-MoS2 from First Principles, ACS Catalysis (2016)

[14] D. Pérez Escobar, C. Miñambres, L. Duprez, K. Verbeken, M. Verhaege, Internal and surface damage of multiphase steels and pure iron after electrochemical hydrogen charging, Corrosion Science 53 (2011) 3166–3176

[15] G. Juilfs, Dissertation, Das Diffusionsverhalten von Wasserstoff in einem niedriglegierten Stahl unter Berücksichtigung des Verformungsgrades und der Deckschichtbildung in alkalischen Medien (2000)

[16] J.O. Bockris, J. McBreen, L. Nanis, The Hydrogen Evolution Kinetics and Hydrogen Entry into a-Iron, Journal of The Electrochemical Society 112 (1965) 1025

[17] Niklas Ehrlin, Christina Bjerkén, and Martin Fisk, Cathodic hydrogen charging of Inconel 718, AIMS Materials Science (2016)

[18] E. Akiyama, S. Li, Electrochemical hydrogen permeation tests under galvanostatic hydrogen charging conditions conventionally used for hydrogen embrittlement study, Corrosion Reviews 34 (2015)

[19] R.T. Loto, C.A. Loto, A.P.I. Popoola, Corrosion inhibition of thiourea and thiadiazole derivatives A Review, J. Mater. Environ. Sci (2012)

[20] C. Yin, J. Chen, D. Ye, Z. Xu, J. Ge, H. Zhou, Hydrogen Concentration Distribution in 2.25Cr-1Mo-0.25V Steel under the Electrochemical Hydrogen Charging and Its Influence on the Mechanical Properties, Materials (Basel, Switzerland) 13 (2020)

[21] G. Mertens, L. Duprez, B. de Cooman, M. Verhaege, Hydrogen Absorption and Desorption in Steel by Electrolytic Charging, Advanced Materials Research 15 (2007) 816–821

[22] Y. Wang, J. Gong, Y. Jiang, W. Jiang, W. Jiang, Ductility loss of hydrogen-charged and releasing 304L steel, Frontiers of Mechanical Engineering 8 (2013) 298–304

[23] Y. Qiao, Q. Yan, J. Cui, H. Wang, Q. Yin, H. Yuan, W. Emori, W. Liu, J. Li, J. Zou, Effect of Hydrogen Charging on the Corrosion Behavior of E690 Steel in 3.5 wt.% NaCl Solution, Journal of Materials Engineering and Performance 31 (2022) 3826–3834

[24] D.-S. Bae, C.-E. Sung, H.-J. Bang, S.-P. Lee, J.-K. Lee, I.-S. Son, Y.-R. Cho, U. Baek, S.-H. Nahm, Effect of highly pressurized hydrogen gas charging on the hydrogen embrittlement of API X70 steel, Metals and Materials International 20 (2014) 653–658

[25] A. Turnbull, 4 - Hydrogen diffusion and trapping in metals, in: R.P. Gangloff, B.P. Somerday (Eds.), Gaseous Hydrogen Embrittlement of Materials in Energy Technologies Woodhead Publishing Series in Metals and Surface Engineering, Woodhead Publishing, 2012

[26] T. Boot, T. Riemslag, E. Reinton, P. Liu, C.L. Walters, V. Popovich, In-Situ Hollow Sample Setup Design for Mechanical Characterisation of Gaseous Hydrogen Embrittlement of Pipeline Steels and Welds, Metals 11 (2021)

[27] Thomas Zauchner, Diffusion von Wasserstoff in Reineisen: Diplomarbeit, Montanuniversität Leoben, 2015

[28] A. Trautmann, G. Mori, M. Oberndorfer, S. Bauer, C. Holzer, C. Dittmann, Hydrogen Uptake and Embrittlement of Carbon Steels in Various Environments, Materials 13 (2020) 3604

[29] A. Trautmann, G. Mori, B. Loder, Hydrogen Embrittlement of Steels in High Pressure H2 Gas and Acidified H2S-saturated Aqueous Brine Solution, BHM Berg- und Hüttenmännische Monatshefte 166 (2021) 450–457

[30] M. Truschner, A. Trautmann, G. Mori, The Basics of Hydrogen Uptake in Iron and Steel, BHM Berg- und Hüttenmännische Monatshefte 166 (2021) 443–449

[31] A. Krom, A. Bakker, Hydrogen trapping models in steel, Metallurgical and Materials Transactions B 31 (2000) 1475–1482

[32] L.S. DARKEN, R.P. SMITH, Behavior of Hydrogen in Steel During and After Immersion in Acid, Corrosion 5 (1949) 1–16

[33] Wung Yong Choo, Jai-Young Lee, Hydrogen trapping phenomena in carbon steel, Journal of Materials Science 17 (1982) 1930–1938

[34] J. Sanchez, A. Ridruejo, P.L. de Andres, Diffusion and trapping of hydrogen in carbon steel at different temperatures, Theoretical and Applied Fracture Mechanics 110 (2020)

[35] A. Thomas, J. Szpunar, Visualisation of diffusion sites and measurement of hydrogen traps in hot-rolled pipes, Materials Science and Technology 36 (2020) 1870–1882

[36] M. Nagumo, Fundamentals of Hydrogen Embrittlement, 2016

[37] E. Fallahmohammadi, G. Fumagalli, G. Re, F.M. Bolzoni, L. Lazzari, Study on hydrogen diffusion in pipeline steels, 2011

[38] J. Crank, The Mathematics of Diffusion, J. W. ARROWSMITH LTD., BRISTOL, ENGLAND, 1975

[39] L. Claeys, T. Depover, I. de Graeve, K. Verbeken, Electrochemical Hydrogen Charging of Duplex Stainless Steel, Corrosion 75 (2018) 880–887

[40] Johann Pengg, Determining the threshold hydrogen concentration of high strength ferritic-pearlitic steel wires using numerical and analytical methods: Bachelorarbeit Montanuniversität, Montanuniversität Leoben, 2021

[41] G. Padhy, Y. Komizo, Diffusible hydrogen in steel welds - A status review, Transactions of JWRI 42 (2013) 2013

[42] G. Dour, IN THE PIPELINE: AN ANALYSIS OF HYDROGEN EMBRITTLEMENT IN PIPELINE STEELS, 2022

[43] K. Kiuchi, R.B. McLellan, The solubility and diffusivity of hydrogen in well-annealed and deformed iron, Acta Metallurgica 31 (1983) 961–984

[44] F.G. Wei, K. Tsuzaki, 13 - Hydrogen trapping phenomena in martensitic steels, in: R.P. Gangloff, B.P. Somerday (Eds.), Gaseous Hydrogen Embrittlement of Materials in Energy Technologies Woodhead Publishing Series in Metals and Surface Engineering, Woodhead Publishing, 2012

[45] R. Oriani, The diffusion and trapping of hydrogen in steel, Acta Metallurgica 18 (1970) 147–157
[46] S. Evers, C. Senöz, M. Rohwerder, Hydrogen detection in metals: a review and introduction of a Kelvin probe approach, Science and Technology of Advanced Materials 14 (2013) 14201
[47] R. E. Ricker, D. J. Pitchure, and M R Stoudt, Analysis of Electrochemical Experiments for Evaluation of Susceptibility to Embrittlement by Hydrogen Gas
[48] j. Bouhattate, E. Legrand, A. Oudriss, S. Frappart, J. Creus, F. Xavier, Simulation of a hydrogen permeation test on a multilayer membrane (2022)
[49] Metrohm Autolab B.V, Corrosion Part 7 – Hydrogen permeation experiments with PGSTAT302F, Autolab Application Note COR07, available at https://www.metrohm-autolab.com/
[50] C.-H. Wu, W. Krieger, M. Rohwerder, On the robustness of the Kelvin probe based potentiometric hydrogen electrode method and its application in characterizing effective hydrogen activity in metal: 5 wt. % Ni cold-rolled ferritic steel as an example, Science and Technology of Advanced Materials 20 (2019) 1073–1089
[51] A. Thomas, J.A. Szpunar, Hydrogen diffusion and trapping in X70 pipeline steel, International Journal of Hydrogen Energy 45 (2020) 2390–2404
[52] J. Kittel, F. Ropital, J. Pellier, Corrosion 2008 (Mar 2008)
[53] A. Zafra, Z. Harris, C. Sun, E. Martínez-Pañeda, Comparison of hydrogen diffusivities measured by electrochemical permeation and temperature-programmed desorption in cold-rolled pure iron, Journal of Natural Gas Science and Engineering 98 (2022) 104365
[54] S. Frappart, X. Feaugas, J. Creus, F. Thebault, L. Delattre, H. Marchebois, Study of the hydrogen diffusion and segregation into Fe–C–Mo martensitic HSLA steel using electrochemical permeation test, Journal of Physics and Chemistry of Solids 71 (2010) 1467–1479
[55] G. Alefeld and J. Volkl, Hydrogen in metals, Springer-Verlag, Berlin, New York, 1978
[56] A.J. Haq, K. Muzaka, D.P. Dunne, A. Calka, E.V. Pereloma, Effect of microstructure and composition on hydrogen permeation in X70 pipeline steels, International Journal of Hydrogen Energy 38 (2013) 2544–2556
[57] Z. Feng, L.M. Anovitz, J.G. Blencoe,S. Babu, and P. S. Korinko, Hydrogen Permeability and Integrity of Hydrogen Delivery Pipelines, 2005
[58] Deborah Houssin,Sile Brennan, Tom Van Esbroeck, Didier Bouix, Deliverable D1.1 Report on hydrogen safety aspects of technologies, systems and infrastructures pertinent to responders: European Train the Trainer Programme for Responders, Fuel Cells and Hydrogen Joint Undertaking (FCH JU), HyResponder (2020)
[59] V. Reitenbach, L. Ganzer, D. Albrecht, B. Hagemann, Influence of added hydrogen on underground gas storage: a review of key issues, Environmental Earth Sciences 73 (2015) 6927–6937

[60] Netherlands Enterprise Agency, The effects of hydrogen injection in natural gas networks for the Dutch underground storages: Final Report, Commisioned by the ministry of Economic Affairs (2017)

[61] Max Svetina, On the risk of hydrogen embrittlement of carbon steels in underground hydrogen storage: Master's Thesis, Montanuniversität Leoben, 2022

Appendix A

Experimental results

A.1 Immersion testing

Table 18. Experimental data ARMCO Fe immersion testing 3.5% NaCl + Thiourea

Time [h]	Hydrogen content [ppm]	Average content [ppm]	Standard deviation [ppm]
1	0.08 0.07	0.075	0.007
3	0.09 0.11	0.1	0.014
10	0.11 0.12	0.115	0.007
24	0.15 0.13	0.14	0.014
72	0.09 0.1	0.095	0.007

Table 19. Experimental data J55 immersion testing 3.5% NaCl + Thiourea

Time [h]	Hydrogen content [ppm]	Average content [ppm]	Standard deviation [ppm]
1	0.11 0.12	0.115	0.007
3	0.13 0.18	0.155	0.035
10	0.19 0.21	0.2	0.014
24	0.28 0.3	0.29	0.014
72	0.23 0.27	0.25	0.028

Table 20. Experimental data L80 immersion testing 3.5% NaCl + Thiourea

Time [h]	Hydrogen content [ppm]	Average content [ppm]	Standard deviation [ppm]
1	0.11 0.09	0.1	0.01
3	0.13 0.12	0.125	0.01
10	0.19 0.17	0.18	0.01
24	0.20 0.19	0.195	0.01
72	0.13 0.15	0.14	0.01

Table 21. Experimental data P110 immersion testing 3.5% NaCl + Thiourea

Time [h]	Hydrogen content [ppm]	Average content [ppm]	Standard deviation [ppm]
1	0.11	0.105	0.007
	0.1		
3	0.13	0.155	0.035
	0.18		
10	0.2	0.19	0.014
	0.18		
24	0.21	0.2	0.014
	0.19		
72	0.12	0.115	0.007
	0.11		

A.2 Cathodic charging

Table 22. Experimental data ARMCO Fe cathodic charging 3.5% NaCl + Thiourea

Time [h]	Hydrogen content [ppm]	Average content [ppm]	Standard deviation [ppm]
1	0.12	0.11	0.014
	0.1		
3	0.14	0.15	0.014
	0.16		
10	0.24	0.235	0.007
	0.23		
24	0.33	0.305	0.035
	0.28		
72	0.38	0.39	0.014
	0.4		

Table 23. Experimental data J55 cathodic charging 3.5% NaCl + Thiourea

Time [h]	Hydrogen content [ppm]	Average content [ppm]	Standard deviation [ppm]
1	0.22	0.23	0.014
	0.24		
3	0.34	0.345	0.007
	0.35		
10	0.54	0.52	0.028
	0.50		
24	0.83	0.805	0.035
	0.78		
72	1.67	1.65	0.028
	1.63		

Table 24. Experimental data L80 cathodic charging 3.5% NaCl + Thiourea

Time [h]	Hydrogen content [ppm]	Average content [ppm]	Standard deviation [ppm]
1	0.19 0.18	0.185	0.007
3	0.34 0.25	0.295	0.064
10	0.45 0.47	0.46	0.014
24	0.82 0.75	0.785	0.05
72	1.53 1.48	1.505	0.035

Table 25. Experimental data P110 cathodic charging 3.5% NaCl + Thiourea

Time [h]	Hydrogen content [ppm]	Average content [ppm]	Standard deviation [ppm]
1	0.29 0.27	0.28	0.021
3	0.39 0.42	0.405	0.021
10	0.67 0.69	0.68	0.014
24	0.98 0.9	0.94	0.057
72	1.92 1.85	1.885	0.05

List of Figures

Figure 1. The electrochemical corrosion mechanism [6] 4

Figure 2. Mechanisms of hydrogen evolution [13] 7

Figure 3. Illustration of cathodic hydrogen evolution: A) According to the Volmer- Tafel mechanism, B) according to the Volmer-Heyrovsky mechanism [12] 7

Figure 4. Illustration of a cathodic hydrogen charging setup [17] 9

Figure 5. Comparison of diffusible hydrogen content measured in the 1-mm-thick specimen after charging and analytical results using a hydrogen diffusion model [20] 10

Figure 6. Hydrogen concentration vs. different charging densities [22] 11

Figure 7. Hydrogen content as a function of different charging current densities [21] 11

Figure 8. Hydrogen concentration for various electrolytes and different current densities of FB450 steel [14] 12

Figure 9. Hydrogen absorption in gaseous environment [25] 13

Figure 10. Hydrogen content after charging at different pressures [30] 14

Figure 11. Hydrogen concentration of P110 after pressurized charging under various conditions [28] 15

Figure 12. Hydrogen concentration of L80 after pressurized charging under various conditions [28] 15

Figure 13. Various sites for hydrogen trapping in steels [33] 16

Figure 14. Illustration of tetrahedral and octahedral interstitial sites in bcc and fcc crystal structures [25] 17

Figure 15. Solid solubility data of hydrogen in steels [36] 18

Figure 16. Hydrogen content as a function of charging time [39] 20

Figure 17. Theoretical fitted saturation curve according 20

Figure 18. Solubility of hydrogen in steel as a function of temperature and pressure [41] 21

Figure 19. Hydrogen diffusion coefficient as a temperature function in different types of metals. [42] 22

Figure 20. Diffusion coefficients in bcc iron as a function of the temperature [44] 23

Figure 21. Illustration of a setup for electrochemical permeation [49] 24

Figure 22. Permeation curve after one polarization [35] 25

Figure 23. Typical permeation curve after two charging cycles [51] 26

Figure 24. Permeation transient with different evaluation methods [53] 26

Figure 25. Arrhenius plot with diffusion coefficients of H in Pd coated ferrite [55] 28

Figure 26. High pressure testing rig up to 120,000 PSI and 1000°C [57] 29

Figure 27. Low pressure testing rig up to 1.3 bar and 500°C [57] 30

Figure 28. Principle of pressure permeation [57] 30

Figure 29. Pressure-time curve for X52 steel at H_2 charging condition of 38 bar and 170°C [57] 31

Figure 30. Microstructure of ARMCO iron: a) longitudinal cut at 100x magnification, b) longitudinal cut at 500x magnification, c) transverse cut at 100x magnification and d) transverse cut at 500x magnification 39

Figure 31. : Microstructure of J55: a) longitudinal cut at 100x magnification, b) longitudinal cut at 500x magnification, c) transverse cut at 100x magnification and d) transverse cut at 500x magnification .. 40

Figure 32. Microstructure of L80: a) longitudinal cut at 100x magnification, b) longitudinal cut at 500x magnification, c) transverse cut at 200x magnification and d) transverse cut at 500x magnification .. 41

Figure 33. Microstructure of P110: a) longitudinal cut at 100x magnification, b) longitudinal cut at 500x magnification, c) transverse cut at 200x magnification and d) transverse cut at 500x magnification .. 42

Figure 34. Specimen dimensions for hydrogen charging 43

Figure 35. Experimental setup immersion test 43

Figure 36. Experimental setup for cathodic charging 44

Figure 37. Illustration of an autoclave used [61] 45

Figure 38. ELTRA H-500 analyser for residual hydrogen content measurements 47

Figure 39. Specimen dimensions for permeation: Left electrochemical and right pressure permeation 47

Figure 40. Experimental setup for electrochemical permeation 48

Figure 41. Experimental setup for pressure permeation 50

Figure 42. Measured hydrogen content of ARMCO Fe for immersion testing 54

Figure 43.Measured hydrogen content compared with the fitted curve after immersion testing of L80 54

Figure 44. Measured hydrogen content compared with the fitted curve after immersion testing of P110 55

Figure 45. Measured hydrogen content compared with the fitted curve after immersion testing of J55 56

Figure 46. Comparison of the theoretical hydrogen saturation curves of the three carbon steels..... 56

Figure 47. Measured hydrogen content after cathodic charging of ARMCO Fe 57

Figure 48. Measured hydrogen content after cathodic charging of J55 58

Figure 49. Measured hydrogen content after cathodic charging of P110 58

Figure 50. Measured hydrogen content after cathodic charging of L80 59

Figure 51. Comparison of the theoretical hydrogen saturation curves of the three carbon steels..... 60

Figure 52. Measured hydrogen content after cathodic charging of carbon steels 60

Figure 53. Measured hydrogen content of all materials after various charging times 61

Figure 54. Normalized first permeation transient of L80 and simulation according to Fick's law 63

Figure 55. Normalized second permeation transient of L80 and simulation according to Fick's Law 64

Figure 56. Comparison of both permeation transients of L80 64

Figure 57. Normalized first permeation transient of P110 and simulation according to Fick's law..... 65

Figure 58. Normalized second permeation transient of P110 and simulation according to Fick's law 66

Figure 59. Comparison of both permeation transients of P110 66

Figure 60. Normalized first permeation transient of ARMCO Fe and simulation according to Fick's law 67

Figure 61. Normalized second permeation transient of ARMCO Fe and simulation according to Fick's law..... 68

Figure 62. Comparison of both permeation transients of ARMCO Fe 68

Figure 63. Normalized first permeation transient of J55 and simulation according to Fick's law 69

Figure 64. Comparison of the permeation transients obtained for all materials 70

Figure 65. Normalized permeation transient of ARMCO iron 71

Figure 66. Normalized permeation transient of J55..... 72

Figure 67. Cathodic hydrogen charging of Armco iron at 10 mA/cm^2..... 74

Figure 68. Comparison of hydrogen saturation curves of L80 75

Figure 69. Comparison of hydrogen saturation curves of P110 75
Figure 70. Comparison of hydrogen saturation curves of J55 76
Figure 71. Diffusion coefficients obtained by various experiments 76
Figure 72. Diffusion coefficient vs. UTS of the investigated materials 77

List of Tables

Table 1. Diffusion coefficients of pipeline steels found in the literature 29

Table 2. Hydrogen properties [58] 33

Table 3. Chemical composition of ARMCO ™ iron in wt% 36

Table 4. Chemical composition of J55 in wt% 37

Table 5. Chemical composition of P110 in wt% 37

Table 6. Chemical composition of L80 in wt% 37

Table 7. Determined hardness and tensile strength of all materials 38

Table 8. Charging conditions 44

Table 9. Charging conditions 45

Table 10. Charging conditions 46

Table 11. Electrochemical charging conditions 48

Table 12. Charging conditions for pressure permeation 50

Table 13. Ground hydrogen content of all examined materials 53

Table 14. Measured data by permeation of L80 64

Table 15. Measured data by permeation of P110 67

Table 16. Measured data by permeation of ARMCO iron 69

Table 17. Measured data by permeation of J55 69

Table 18. Experimental data ARMCO Fe immersion testing 3.5% NaCl + thiourea 85

Table 19. Experimental data J55 immersion testing 3.5% NaCl + Thiourea 86

Table 20. Experimental data L80 immersion testing 3.5% NaCl + Thiourea 86

Table 21. Experimental data P110 immersion testing 3.5% NaCl + Thiourea 87

Table 22. Experimental data ARMCO Fe cathodic charging 3.5% NaCl + Thiourea 88

Table 23. Experimental data J55 cathodic charging 3.5% NaCl + Thiourea 88

Table 24. Experimental data L80 cathodic charging 3.5% NaCl + Thiourea 89

Table 25. Experimental data P110 cathodic charging 3.5% NaCl + Thiourea 89